

**THE MODELLING OF SPECIES WITH POTENTIAL
USE AS CARRIERS OF RADIONUCLIDES FOR
BONE CANCER THERAPY**

Janine Robinson

**A dissertation submitted to the Faculty of Science,
University of the Witwatersrand, Johannesburg, in
fulfilment of the Degree of Master of Science**

Johannesburg,

2008

Declaration

I declare that this thesis is my own, unaided work. It is being submitted for the Degree of Master of Science in the University of the Witwatersrand, Johannesburg. It has not been submitted before for any degree or examination in any other University.

(Signature of Candidate)

_____ day of _____ 2008

Abstract

The ability of the Generalised AMBER Force Field (GAFF) to model the structure of bisphosphonate ligands, $C(R_1)(R_2)(PO_3^{2-})_2$, important compounds in the treatment of bone cancer, by molecular mechanics methods is evaluated. The structures of fifty bisphosphonates and nine bisphosphonate esters were predicted and compared with their crystal structures. Partial charges were assigned from a RHF/6-31G* single point calculation at the geometry of the crystal structure. Additional parameters required for GAFF were determined using the methods of the force field's developers. The structures were found to be well replicated with virtually all bond lengths reproduced to within 0.015 \AA (1.2σ). Bond angles were reproduced to within 1.9° (0.8σ). The observed gauche or anti conformation of the molecules was reproduced, although in several instances gauche conformations observed in the solid state energy-minimised into anti conformations, and vice versa. The interaction of MDP ($R_1 = R_2 = H$), HEDP ($R_1 = OH, R_2 = CH_3$), APD ($R_1 = OH, R_2 = (CH_2)_2NH_3^+$), alendronate ($R_1 = OH, R_2 = (CH_2)_3NH_3^+$) and neridronate ($R_1 = OH, R_2 = (CH_2)_5NH_3^+$) with the (001), (010) and (100) faces of hydroxyapatite was examined by energy-minimising twenty random orientations of each ligand 20 \AA from the mineral and then at about 8 \AA from the surface whereupon the ligand relaxes onto the surface. The difference in energy between the two systems is the interaction energy. In all cases interaction with hydroxyapatite caused a decrease in energy. On the (001) face, both phosphonate groups interact near a surface Ca^{2+} ion. The magnitude of the exothermic interaction energy varies with molecular volume (MDP < HEDP < APD < alendronate) except for neridronate, which interacts less effectively than alendronate because the long amino side chain folds in on itself and does not align with the surface of the mineral. The bisphosphonates adopt two conformations on the (010) face. In the first of these, found for MDP and 40% of the alendronate structures, both phosphonates interact with the surface and the side chain points away from the surface. In the second conformation, one phosphonate and the $C\alpha$ side chain interact with the surface. The interaction energy increases with the molecular volume of the ligand, again with the exception of neridronate. Two conformations also occur on the (100) face. In the first conformation, only one of the phosphonate groups points towards the surface and the $C\alpha$ side chain interacts with the surface; in the second conformation the $C\alpha$ side chain interacts strongly with the surface and both phosphonate groups point away from the surface towards the solution. The first conformation is energetically more favourable. Its magnitude is

virtually insensitive to the nature of the side chain and is similar to the magnitude of the interaction energy on the other two faces. The magnitude of the second conformation increases with the size of the C α side chain.

Acknowledgements

I would just like to thank a few people who without their assistance this project would not have been possible.

Firstly I would like to thank Professor Helder Marques for all his valuable assistance and guidance over the last few years. Professor Marques has always been available to assist and patiently explain the science of the research (often repeatedly) to me. Thank you for always being so open and willing to share your expertise with me. He has been extremely supportive and I am really grateful.

Secondly I would like to thank Dr. Alvaro De Sousa who assisted with various aspects of this project.

Thank you to Manuel Fernandes and Professor Dave Billing who were always available to assist with any queries in connection with crystallographic structures or modelling.

Finally I would like to thank Agnes for always assisting with the daily running of the admin to and from Professor Marques.

To everyone else in the Department of Chemistry who assisted with the project daily, thank you very much.

Publication

Robinson J., Cukrowski I., Marques H.M., *J. Mol. Struct.*, **825**, (2006), 134-142.

Table of Contents	Page
Abstract	iii
Acknowledgements	iv
Publication	v
Table of Contents	vi
List of Figures	ix
List of Tables	xi
Abbreviations	xii
Chapter 1: Introduction	1
1. Overview of bone cancer	1
Bone metastasis	1
A possible mechanism for lytic tumour growth	2
2. Bisphosphonates (BP) and their use in cancer treatment	3
The relative activity of bisphosphonates on bone resorption	4
3. Literature survey- previous molecular modelling of bisphosphonates	6
4. Molecular modelling	8
Quantum chemistry	8
The Born-Oppenheimer approximation (BOA)	9
Molecular orbital (MO) calculations	9
Hartree product and Slater determinant	9
Molecular orbital calculations	10
Hartree-Fock (HF) approach	10
Roothaan-Hall (RH) approach	11
Semi-empirical methods	11
Force field calculations	12

	Page
5. Optimisation of the force field	16
Derivative methods	16
Steepest descent method	16
Conjugate gradient methods	17
6. Simulated annealing.	17
7. Aim	18
Chapter 2: Experimental	19
1. Choice of force field parameterisation	19
1.1. GAFF Force Field	20
2. Crystal structures	22
2.1. Preparation of crystal structures for molecular modelling	22
2.1.1. Allocation of partial charges	28
3. Preparation of the force field	30
4. Modelling of the bisphosphonates (BPs)	33
5. Interactions with the bone surface	33
5.1. The hydroxyapatite surface, $\text{Ca}_5(\text{PO}_4)_6(\text{OH})_2$	33
5.2. Interactions of the bisphosphonates with the hydroxyapatite surface	35
Chapter 3: Results and Discussion	40
1. Modelling of the bisphosphonates	40
1.1. Semi-empirical methods versus <i>ab initio</i> calculations	41
2. The modelling of the ligands	42
3. Simulated annealing of the bisphosphonates	45

4. Modelling of the interactions of the bisphosphonates with hydroxyapatite	46
4.1. Modelling of the hydroxyapatite surface	46
4.1.1. The (001) face of hydroxyapatite	46
4.1.2. The (010) face of hydroxyapatite	47
4.1.3. The (100) face of hydroxyapatite	47
4.2. Testing of the effect of the relative permittivity	48
4.3. Interactions of the bisphosphonates with the hydroxyapatite surface	51
4.3.1. Interactions of the mono-protonated bisphosphonates with the hydroxyapatite surface	51
4.3.1.1. Interactions with the (001) face of hydroxyapatite	54
4.3.1.2. Interactions with the (010) face of hydroxyapatite	57
4.3.1.3. Interactions with the (100) face of hydroxyapatite	58
4.3.2. Interactions of the di-protonated bisphosphonates with the hydroxyapatite surface	60
4.3.2.1. Interactions with the (001) face of hydroxyapatite	61
4.3.2.2. Interactions with the (010) face of hydroxyapatite	63
4.3.2.3. Interactions with the (100) face of hydroxyapatite	64
Chapter 5: Conclusion	66
Chapter 6: Future Work	67
Chapter 7: Appendix	68
Chapter 8: References	100

List of Figures

Figure 1: The cycle of tumour growth.

Figure 2: A generalised bisphosphonate.

Figure 3: Examples of first (a), second (b) and third (c) generation bisphosphonates.

Figure 4: A comparison of Hooke's law versus a Morse potential function.

Figure 5: The torsion angle is defined by the angle formed by the three red bonds.

Figure 6: Example of a charge distribution for a bisphosphonate.

Figure 7: Illustration that the linear combination of two Gaussian orbitals is a Gaussian orbital

Figure 8: (001), (010) and (100) faces of hydroxyapatite.

Figure 9: Partial charges for the smallest unit of hydroxyapatite, $\text{Ca}_5(\text{PO}_4)_6(\text{OH})_2$.

Figure 10: Atom types for the bisphosphonate backbone.

Figure 11: Overlay of alendronate (fully deprotonated) obtained from simulated annealing and from force field calculations.

Figure 12: Representation of a surface cavity and an octahedral cavity present on (001) surface of hydroxyapatite.

Figure 13: Representation of the (010) surface of hydroxyapatite showing translation along the c axis.

Figure 14: Representation of the (100) face of hydroxyapatite showing translation along the a axis.

Figure 15: Side-on and top view of the overlaid structures of (A,B) APD and (C,D) HEDP on the (001) face of hydroxyapatite generated from a common starting structure in which the ligand was 10\AA from the surface of hydroxyapatite and allowed to relax onto the surface, whilst changing the dielectric constant between $75\epsilon_0$ and $10\epsilon_0$.

Figure 16: Graphical representation showing the dependence of the total energy of the minimised structure on the relative permittivity.

Figure 17: Representations of the interaction of the bisphosphonates with the (001) face of hydroxyapatite (represented by: A-C: HEDP, D-E: alendronate).

- Figure 18: Dependence of the interaction energy of five bisphosphonate ligands and the (001) face of hydroxyapatite on the molecular volume of the ligand.
- Figure 19: Representations of the interactions of the two conformations A and B adopted by the bisphosphonates when interacting with the (010) surface of hydroxyapatite (represented by HEDP).
- Figure 20: Representations of the interactions of the two conformations A (represented by alendronate) and B (represented by HEDP) adopted by the bisphosphonates when interacting with the (100) surface of hydroxyapatite.
- Figure 21: Species distribution for APD (A), alendronate (B) and neridronate (C).
- Figure 22: Representation of the interaction between the (001) surface of hydroxyapatite and neridronate, $[H_2L^{2-}]$.
- Figure 23: Representation of the intramolecular hydrogen bond present in the di-protonated bisphosphonates when interacting with the (001) surface of hydroxyapatite (represented by neridronate).
- Figure 24: Graphical representation showing that as the length of the $C\alpha$ chain increases so the interaction energy increases.
- Figure 25: The interactions of the two conformations A and B of di-protonated alendronate with the (010) surface of hydroxyapatite.
- Figure 26: Representation of the interaction of conformation A (represented by alendronate) and B (represented by APD) of the di-protonated bisphosphonates with the (100) surface of hydroxyapatite.

List of Tables

- Table 1: The antiresorptive potency of a series of bisphosphonates
- Table 2: Definition of atom types
- Table 3: Numbering system
- Table 4: Additional parameters added to GAFF for the modelling of bisphosphonate ligands
- Table 5: Unpublished acid dissociation constants determined by glass electrode potentiometry in our laboratory (298 K and $\mu=0.15$ M NaCl)
- Table 6: Partial charges on five bisphosphonate ligands in their monoprotinated and di-protonated forms as determined from a SCF-RHF calculation at the crystal structure geometry using a 6-31G* basis set
- Table 7: Partial charge distribution for the bisphosphonate backbone atom types
- Table 8: Comparison of bond lengths and bond angles obtained using structures with partial charge distributions obtained from PM3 and RHF methods
- Table 9: Comparison of the bond lengths and bond angles of bisphosphonate ligands observed crystallographically and those predicted using molecular mechanics and GAFF
- Table 10: Comparison of the bond lengths and bond angles of bisphosphonate ester ligands observed crystallographically and those predicted using molecular mechanics and GAFF
- Table 11: Change in strain energy, ΔE_s , for the interactions of APD and HEDP with the (001) surface of hydroxyapatite as a function of the relative permittivity.
- Table 12: Change in strain energy, ΔE_s , for the interactions of the mono-protonated bisphosphonate ligands with the three surfaces of hydroxyapatite
- Table 13: Interaction of bisphosphonates with hydroxyapatite: distances between oxygen atoms of phosphonates and the nearest calcium ions on the (001) face of hydroxyapatite
- Table 14: Interaction energies of di-protonated nitrogen containing bisphosphonates with the various faces of hydroxyapatite

Table of Abbreviations

Abbreviation	
AMBER	assisted model building and energy refinement
BOA	Born-Oppenheimer approximation
BP(s)	bisphosphonate (s)
CHARMM	Chemistry at Harvard Macromolecular Mechanics
CoMFA	comparative molecular field analysis
CSD	Cambridge structural database
FPP	farnesyl pyrophosphate
GAFF	generalised AMBER force field
GGPP	geranylgeranyl pyrophosphate
GPP	geranyl pyrophosphate
HF	Hartree-Fock
HP	Hartree product
IPP	isopentenyl pyrophosphonate
MM2, MM3	Allinger's MM2 and MM3 force field
MO	molecular orbital
NMR	nuclear magnetic resonance
OPLS	optimised potentials for liquid simulations
PRPP	phosphoribosylpyrophosphate
PRT	purine phosphoribosyltransferase
PTHrP	parathyroid hormone related protein
RH	Roothaan Hall
RHF	restricted Hartree-Fock
SD	Slater determinant
SE	Schrödinger equation
TcHPRT	trypanosoma cruzi
TGF- β	transforming growth factor β
UFF	universal molecular mechanics force field [28]
WitsGAFF	our version of GAFF

XRD	x-ray diffraction
-----	-------------------

Chapter 1: Introduction

1. Overview of bone cancer

Cancer is a group of diseases consisting of more than one hundred different types. Cancer is present when cells become abnormal. These cells subsequently grow and destroy body tissue and are even capable of spreading to other parts of the body [1].

Healthy cells that make up the body's tissues grow, divide, and replace themselves in an orderly way. This process keeps the body in good repair but cells that lose the ability to control their growth grow too rapidly and without any order. This leads to the formation of too much tissue; this extra tissue is called a tumour. Tumours can be benign or malignant. Benign tumours are non-cancerous and are seldom life-threatening whereas malignant tumours are cancerous. Malignant tumours invade and destroy nearby healthy tissues and organs [1].

Bone cancer can originate at the bone (primary bone cancer) or have spread to the bone from another organ (secondary or metastatic bone cancer). The primary sources for secondary bone cancer are tumours from breast, lung, prostate and renal cancer [2-4]. The focus of the work in this dissertation relates to secondary cancer.

Symptoms of [bone cancer](#) develop slowly with the most frequent initial symptom being terrible pain. Other common symptoms include the presence of a firm, slightly tender lump on the bone that can be felt through the skin (this is due to calcemia), bone fracturing [4] and spinal cord compression [5]. The presence of bone metastasis is determined by radiography and bone scans.

1.1. Bone metastasis

Bone consists of both organic and cellular elements containing minerals, cytokines, growth factors, bone and hematopoietic cell lines. Healthy bone is always remodelling. This is characterised by two opposite actions, the formation of new bone by osteoblasts and the resorption of the old bone by osteoclasts. If this cycle is disturbed by a tumour, lesions will form. A lytic lesion occurs when the resorption of the bone occurs more rapidly than the deposition thus leading to pits in the bone; a blastic lesion occurs when the rate of deposition is greater than that of resorption, which leads to the formation of a soft lump on the bone. As this lump is very soft, the bone is fragile and can break easily. It is also possible for an imbalance to occur in both processes thus leading to the formation of a mixed lesion [2].

1.1.1. A possible mechanism for lytic tumour growth

During resorption, the bone releases cytokines and growth factors, which interact with the tumour. The tumour releases cell signals that stimulate the osteoclasts. In the formation of osteolytic lesions these signals include the release of the parathyroid hormone related protein (PTHrP) and the transforming growth factor β (TGF- β). The tumour cells produce excess TGF- β , thus stimulating osteoclastic bone resorption that in turn leads to the release of TGF- β by the bone. These elevated levels of TGF- β stimulate the metastatic capability of the tumour and the tumour's ability to produce PTHrP. Thus a cycle is formed that leads to tumour growth and the development of large lesions [2]. Figure 1 shows a graphical representation of this process.

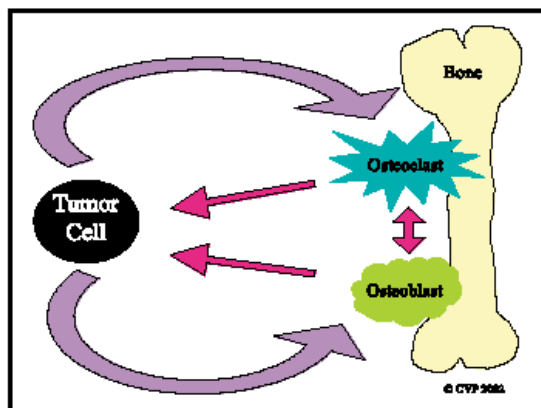


Figure 1: The cycle of tumour growth [2]

Common treatments for bone cancer include surgery, [radiation therapy](#), hormone treatment, radioisotopic treatment, and/or chemotherapy. Usually it is necessary to use a combination of

treatment methods, dependent on the patient's needs. For most bone cancer patients surgery is necessary. During surgery the tumour and the healthy bone and tissue from around the tumour are removed [2,4].

[Chemotherapy](#) uses a combination of drugs which are administered orally or intravenously to kill cancer cells. These drugs travel through the blood stream to the infected area where they kill the cells. The treatment is given in a cycle of treatment periods followed by recovery periods. Chemotherapy is almost always used to shrink a tumour before surgery. In addition, it is usually used as an additional therapy after surgery to kill cancer cells that may remain in the body and to prevent tumour regrowth. For certain bone cancers, chemotherapy is combined with radiation therapy [2,4].

Often cancer treatment involves the use of high-energy rays to damage cancer cells and to stop cell growth. This is known as radiation therapy. In some cases, radiation therapy is used instead of surgery to destroy the tumours. This form of treatment is also used to destroy cancer cells that remain in the area after surgery [2,4].

Radioisotopic treatment has become a common treatment for bone cancer. Radioisotopic treatment involves the use of several radiopharmaceuticals that are administered intravenously. These radiopharmaceuticals attack the tumour, even at very low concentration, by emitting radiation to kill the tumour. A commonly used series of radiopharmaceuticals are the bisphosphonates [2-10].

2. Bisphosphonates (BP) and their use in cancer treatment

Bisphosphonates are chemically and biologically equivalent to naturally-occurring inorganic pyrophosphate [6,11]. They are a group of compounds that contain a P-C-P backbone structure with two phosphonic acid groups attached to the same central carbon atom as illustrated in Figure 2.

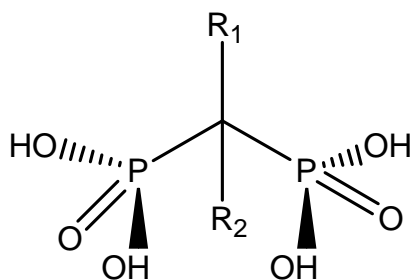


Figure 2: A generalised bisphosphonate

BPs were originally used in industry for fertilizers, oil and textiles but in the late 1960's they began being used in medicine [3]. Their uses in medicine include treatments for bone diseases such as osteoporosis, hypercalcemia, Paget disease and bone metastasis [2-12] .

The exact mechanism by which BPs inhibit bone resorption is not yet fully understood. BPs have a high affinity for bone minerals thus preventing calcification and inhibiting the dissolution of hydroxyapatite crystals (principal mineral in bone, $\text{Ca}_{10}(\text{PO}_4)_6(\text{OH})_2$) [11]. Clinical research has shown that in breast and prostate cancer bisphosphonates can prevent the attachment of tumours to the bone matrix thus preventing secondary bone cancer [13]. Clinical data also suggest that the presence of bisphosphonate treatment decreases tumour cell growth and increases the efficiency of antineoplastic therapy [14]. BPs (even at very low concentrations) inhibit the precipitation of calcium salts [2,3,8,13], and since bone metastasis often leads to raised calcium levels in the blood, this is extremely useful [2]. BPs are used to coordinate beta-emitting radionuclides, such as samarium-153 and rhenium-186, for bone cancer treatment [9-11].

2.1. The relative activity of bisphosphonates on bone resorption

The activity of the BPs varies from one compound to another; thus much research needs to be done into the specific activity of each compound. The relevant potency (the ability to inhibit resorption) is dependent on the substituents on the central carbon atom. Three classifications of BPs are currently available: first generation BPs have simple substituents on the central carbon atom, second generation BPs have an aliphatic amine containing a chain and third generation BPs contain a hetrocyclic substituent (Figure 3).

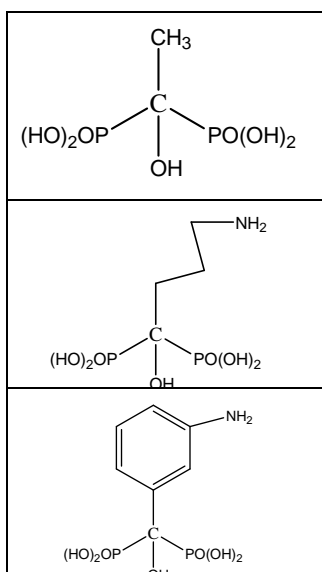


Figure 3: Examples of first (a), second (b) and third (c) generation bisphosphonates

The 3rd generation BPs are the most potent [7]. Table 1 shows the relative potencies of some common bisphosphonates using etidronate as the reference point [11].

Table 1: The antiresorptive potency of a series of bisphosphonates [11]

Bisphosphonate	R1	R2	Potency
Clodronate	Cl	Cl	~ 10×
Etidronate	OH	CH ₃	~ 1×
Pamidronate	OH	(CH ₂) ₂ NH ₂	~ 100×
Alendronate	OH	(CH ₂) ₃ NH ₂	>100 < 1000×
Neridronate	OH	(CH ₂) ₅ NH ₂	~ 100×
Olpadronate	OH	(CH ₂) ₂ N(CH ₃) ₂	> 100 < 1000×
Ibandronate	OH	(CH ₂) ₂ N(CH ₃)(CH ₂) ₄ CH ₃	> 1000 < 10000×
Risedronate	OH	CH ₂ -3-pyridine	> 1000 < 10000×
Zoledronate	OH	CH ₂ -imidazole	> 10000×

From Table 1 it is seen that the nitrogen-containing BPs (second generation) have a greater potency than the first generation BPs. This is due to the fact that the nitrogen-containing BPs, in addition to inhibiting bone resorption, also inhibit osteoclastic function [2].

The exact relationship between the nature of the carbon substituents and the potency is not yet clear. Thus it would be useful to try to construct a predictive knowledge base. One of the predictive tools that could be incorporated in such a knowledge base and that we attempted to develop in this project was molecular modelling.

3. Literature survey— previous molecular modelling of bisphosphonates

Limited molecular modelling has been performed on bisphosphonate ligands. Neves *et al.* [15] used the CVFF 950 molecular mechanics force field to study the structure of pamidronate ($R_1 = (\text{CH}_2)_2\text{NH}_2$, $R_2 = \text{OH}$, Figure 1), alendronate ($R_1 = (\text{CH}_2)_3\text{NH}_2$, $R_2 = \text{OH}$) and neridronate ($R_1 = (\text{CH}_2)_5\text{NH}_2$, $R_2 = \text{OH}$) *in vacuo*. They found that intramolecular hydrogen bonding between the terminal amino group and the hydroxyl group is the dominant interaction in pamidronate and alendronate, so that the amino group is gauche to the backbone carbon. For neridronate the intramolecular hydrogen bonding is less significant, and the trans conformation is favoured. The interactions with the (001) face of hydroxyapatite were examined, as this is believed to be the fastest growing face [16]. It was found that the most important interactions occurred between the phosphonate and the amino groups of the bisphosphonate ligands and the calcium ions of hydroxyapatite [15]. The distance between the nitrogen atom and the nearest calcium ion is lowest for alendronate (3.75 Å, compared with 5.77 Å for pamidronate and 5.07 Å for neridronate) implying that the stabilising interaction energy for alendronate is more significant than for the other ligands. This is in agreement with *in vivo* studies, which have shown that the pharmacologic activity of alendronate is an order of magnitude larger than the other two ligands [17].

In vitro studies have shown that nitrogen-containing bisphosphonates inhibit isopentenyl pyrophosphate (IPP) isomerase/farnesyl pyrophosphate (FPP) in a dose-dependent manner which mimics the *in vivo* bone antiresorptive properties [18]. Similarly these ligands also inhibit farnesyl pyrophosphate/geranylgeranyl pyrophosphate (GGPP) synthase in plants [19,20]. Martin and co-workers [21] used molecular graphics methods to examine the

interaction of nitrogen-containing bisphosphonates of known structure as well as a naturally-occurring bisphosphonate equivalent, geranyl pyrophosphate, GPP (a known isomerase/synthase inhibitor), with FPP synthase to determine how these interact at the binding site. The results showed that bisphosphonates and GPP interacted similarly with FPP synthase demonstrating that bisphosphonates should have an effect on the resorption of bone. It was found that alendronate mimicked bound GPP the closest with a r.m.s. fit of 0.3 Å, implying that alendronate is the best ligand to inhibit bone resorption [21].

It is known that high levels of pyrophosphate are present in many of the major human disease-causing parasitic protozoa [22-25] and it has been shown that bisphosphonates have inhibitory effects on various parasite enzymes [26]. Szabo and Oldfield [27] used molecular mechanics (with a universal molecular mechanics force field, UFF [28]) to carry out a qualitative analysis of a series of known bisphosphonate structures and of imidodiphosphonate. Comparative molecular field analysis (CoMFA) was used to construct a rectangular energy grid for each molecule. Each molecule was compared with the most active molecule, aminomethylene bisphosphonate, by performing a r.m.s.-fitting of the pharmacophoric atoms of each molecule. They were then allowed to explore conformational space near to V/H⁺-PPase (proton pumping vacuolar pyrophosphatase found in the mung bean). It was concluded that the major component in the interaction of a bisphosphonate with the enzyme is ionic in nature and it was suggested that bisphosphonates can be used as inhibitors for these parasitic diseases [27].

Trypanosoma cruzi (TcHPRT) is the causative agent in the deadly Chaga's disease. It is believed that purine phosphoribosyltransferase (PRT) is an inhibitor of these parasitic diseases [29,30]. Fernandez and co-workers [31] compared the interactions of both the bisphosphonates and HPRT, hydroxanthine-guanine PRT, with TcHPRT.

PRPP (phosphoribosylpyrophosphate) was used to represent the TcHPRT. A Monte Carlo procedure was used to explore the conformational space available to a series of bisphosphonates. These structures were then compared with the HPRT complex and then docked in the close proximity of the PRPP. The results show that these structures would bind well to PRPP, suggesting a use for these ligands in drug design.

4. Molecular modelling

4.1. Quantum chemistry

The behaviour of very small particles, such as electrons and nuclei of atoms and molecules, is not correctly described by classical Newtonian mechanics, because of their wave-like properties and the uncertainty principle. Thus it is necessary to use an alternative method. A series of laws have subsequently been defined for this application - these are the laws of quantum mechanics [32].

The fundamental equation of quantum mechanics is the full time-dependent Schrödinger equation (SE) (equation 1),

$$\left\{ -\frac{\hbar^2}{2m} \left(\frac{\partial^2}{\partial x^2} + \frac{\partial^2}{\partial y^2} + \frac{\partial^2}{\partial z^2} \right) + V \right\} \Psi(\mathbf{r}, t) = i\hbar \frac{\partial \Psi(\mathbf{r}, t)}{\partial t} \quad \dots(1)$$

which refers to a single particle of mass m moving through space \mathbf{r} (three dimensional position vector) and time t under the influence of an external force V ; \hbar is Planck's constant divided by 2π and i is the imaginary number $\sqrt{-1}$. $\Psi(\mathbf{r}, t)$ refers to the wavefunction that describes the motion of the particle.

When the external force is independent of time the wavefunction can be divided into the contribution due to spatial arrangement and the contribution due to time. Then by assuming that the potential is independent of time the SE can be simplified to the time-independent SE (equation 2).

$$\left\{ -\frac{\hbar^2}{2m} \left(\frac{\partial^2}{\partial x^2} + \frac{\partial^2}{\partial y^2} + \frac{\partial^2}{\partial z^2} \right) + V \right\} \Psi(\mathbf{r}) = E\Psi(\mathbf{r}) \quad \dots(2)$$

Then by introducing the Hamiltonian operator (equation 3) on the left hand side of the equation the time-independent SE can be simplified to equation 4.

$$H = -\frac{\hbar^2}{2m} \left(\frac{\partial^2}{\partial x^2} + \frac{\partial^2}{\partial y^2} + \frac{\partial^2}{\partial z^2} \right) + V \quad \dots(3)$$

$$H\Psi(\mathbf{r}) = E\Psi(\mathbf{r}) \quad \dots(4)$$

To solve the time-independent SE it is necessary to determine the values for the energy E and for the wavefunction. These equations allow one to calculate various properties of the system such as potential energy and kinetic energy of the single nucleus. The problem is that it is impossible fully to solve the time-independent SE for polyelectronic atoms or molecules as the mathematics of the system becomes too complex. Therefore it is necessary to make various assumptions [32-34].

4.1.1. The Born-Oppenheimer approximation (BOA)

The BOA states that the motion of the electrons can be decoupled from the motion of the nuclei. Since the mass of the nucleus is much larger than that of the electron, the electron will be able to adjust to any positional change of a nucleus almost instantaneously, i.e. the nucleus will appear stationary when considering the motion of the electron. Thus the wavefunction is only dependent on the position of the nuclei and the electronic energy of the system. The electronic energy comprises the kinetic and potential energies of the electrons moving in the electronic field. When applying the BOA to calculations, it is assumed that the positions of the nuclei are fixed.

This approximation is useful for small molecules where the number of electrons is small but is impractical for larger molecules as the number of electron-electron repulsions will be too large to calculate in a reasonable time i.e. the calculations become computationally prohibitive. It is more practical to use molecular orbital methods.

4.2. Molecular orbital (MO) calculations

4.2.1. Hartree product and Slater determinant

A possible functional form of the wavefunction is the Hartree Product (HP, equation 5).

$$\Psi(1, 2, \dots N) = \chi_1(1)\chi_2(2)\dots \chi_N(N) \quad \dots(5)$$

The energy of this system is equal to the sum of the one-electron spin orbitals; this implies that the probability of finding one electron at a specific point is independent of finding another electron at that point in space. This is not strictly correct as there is a correlation between the motion of the electrons. The HP also assumes that the electrons are assigned to specific orbitals. This assumption disagrees with the antisymmetry principle, which states that electrons are indistinguishable. For a polyelectronic system, a determinant that obeys the antisymmetry principle, is used to represent the functional form. This functional form is known as the Slater Determinant (SD, equation 6). The SD allows for interactions between electrons but in addition

it also obeys Pauli's Principle (two electrons cannot have the same set of quantum numbers) since if two electrons did have the same quantum numbers the determinant would break down.

$$\Psi = \frac{1}{\sqrt{N!}} \begin{vmatrix} \chi_1(1) & \chi_2(1) & \dots & \chi_N(1) \\ \chi_1(2) & \chi_2(2) & \dots & \chi_N(2) \\ \vdots & \vdots & & \vdots \\ \vdots & \vdots & & \vdots \\ \chi_1(N) & \chi_2(N) & \dots & \chi_N(N) \end{vmatrix} \quad \dots(6)$$

4.2.2. Molecular orbital calculations

For MO calculations performed on molecules each molecular orbital is expressed as a linear combination of atomic orbitals (equation 7).

$$\psi_i = \sum_{\mu=1}^K c_{\mu i} \phi_{\mu} \quad \dots(7)$$

where ψ_i is the molecular orbital, ϕ_{μ} is an atomic orbital and $c_{\mu i}$ is a coefficient. The first step in a molecular orbital calculation is to determine the energy of the system. This is calculated by using equation 8.

$$E = \frac{\int \Psi(\mathbf{r}) H \Psi^*(\mathbf{r}) d\tau}{\int \Psi(\mathbf{r}) \Psi^*(\mathbf{r}) d\tau} \quad \dots(8)$$

For a large system these integrals are very difficult and time-consuming to determine thus it is necessary to make some approximations. The two common *ab initio* (or from first principles) approaches used are the Hartree-Fock approach and the Roothaan-Hall approach.

4.2.2.1. Hartree-Fock (HF) approach

For a large system, there are various functional forms of the wavefunction. Thus it is necessary to determine which is the best form for the application. This is determined by using the variation theorem which states that the energy calculated from an approximation to the wavefunction will always be greater than the actual energy of the system. The HF equations are obtained by constraining the energy expression to a minimum ($\partial E = 0$) such that the orbitals are orthonormal to each other. By using various mathematical methods the HF equations are simplified to equation 9 [33].

$$f_i \chi_i = \varepsilon_i \chi_i \quad \dots (9)$$

$$\text{where : } f_i(1) = H^{core}(1) + \sum_{j=1}^N \{J_j(1) - K_j(1)\}$$

$$H^{core}(1) = -\frac{1}{2} \left(\frac{\partial^2}{\partial x^2} + \frac{\partial^2}{\partial y^2} + \frac{\partial^2}{\partial z^2} \right) - \sum_{A=1}^M \frac{Z_A}{r_{1A}}$$

$$J_j(1) = \int d\tau_2 \chi_j(2) \frac{1}{r_{12}} \chi_j(2)$$

$$K_j(1) \chi_i(1) = \left[\int d\tau_2 \chi_j(2) \frac{1}{r_{12}} \chi_i(2) \right] \chi_j(1)$$

f_i is known as the Fock operator, J_i is the coulombic operator and K_i is the exchange operator. An assumption used when doing a calculation is that each electron is moving in a fixed field consisting of nuclei and other electrons, in other words the solution for one electron will affect the solution for another electron. The strategy used to solve these calculations is the Self-Consistent Field approach. A set of trial solutions for the molecular orbitals are used to calculate the coulombic operator and exchange operator; these in turn are used to calculate the HF equations. From these results the new set of molecular orbitals are calculated. This method is iterated until the results for the electrons are statistically equivalent.

Often direct solutions for molecules are impractical and thus each spin orbital can be written as a linear combination of single electron orbitals. These one electron orbitals are known as a basis set and often correspond to the atomic orbitals. The size of the input basis set will be dependent on the computational efficiency and needed accuracy for a specific calculation. The basis sets are usually used with the Slater Determinant functional form of the wavefunction.

4.2.2.2. Roothaan-Hall (RH) approach

The RH equations are based on the HF equations but to promote calculation efficiency the equations are adapted into a matrix form, which computationally is easier to work with. These equations are used as the basis for many semi-empirical methods [35,36].

4.3. Semi-empirical methods

Ab initio calculations are extremely time-consuming and expensive on computer resources whereas the semi-empirical methods are much simpler to solve. They incorporate experimentally determined parameters rather than determining them during the calculation. For many calculations these simplifications are sufficient. As stated above these approximation methods are based on the RH equations. Many approximation methods are currently in use [32-34].

4.4. Force field calculations

While quantum mechanics is extremely useful, it is often impractical for many chemistry problems as the number of electrons in the system is too large. Therefore another method is needed. Molecular mechanics (or force field methods) ignores the electronic motions of the system and calculates the energy of the system as a function of the positions of the nuclei only.

A minimalistic force field is a mathematical model that consists of four terms that represent the intra- and intermolecular interactions of the system. These terms are the potential energies to stretch a bond, to bend an angle, to distort a torsion and non-bonded interactions, including van der Waals and electrostatic interactions. The bond stretching and angle bending terms are referred to as the hard 'degrees of freedom' as large amounts of energy are needed to distort the bonds and angles from equilibrium while the torsions and non-bonded interactions are softer in nature.

The bond stretching term is best represented by a Morse potential (equation 10, Figure 4) but due to the lack of computational efficiency, it is more economical to use a Hooke's law formula (equation 11, Figure 4). The Hooke's law formula is as accurate as the Morse potential provided that the deviation from the equilibrium length is not large.

$$V(l) = D_e \left\{ 1 - \exp[-a(l - l_o)] \right\}^2 \quad \dots (10)$$

$$V(l) = \frac{k}{2} (l - l_o)^2 \quad \dots (11)$$

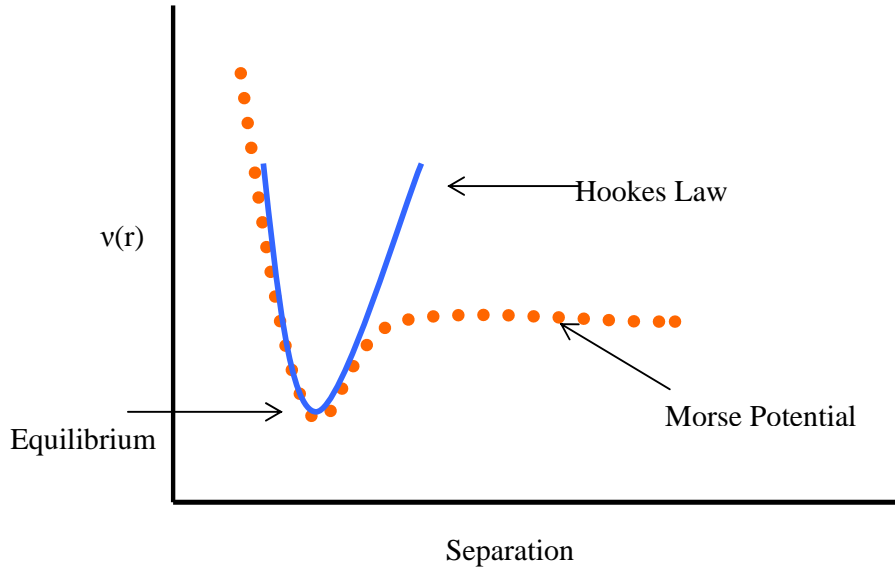


Figure 4: A comparison of Hooke's law versus a Morse potential function

Hooke's law says that the energy to stretch a bond is proportional to the square of the displacement from the equilibrium length l_0 . The equilibrium length is a reference length (or strain-free length), which is the length that the bond will adopt when all other terms in the force field are set equal to zero, and k is a force constant. These parameters are input parameters. This term is the largest contributing term to the potential energy of the system.

The angle bending term also uses the form of a Hooke's law equation (equation 12), where θ_0 is the reference angle and k is a force constant that can be determined by a variety of methods. Less energy is needed to distort an angle away from equilibrium than to stretch a bond. Thus the force constants are much smaller in magnitude.

$$V(\theta) = \frac{k}{2} (\theta - \theta_0)^2 \quad \dots (12)$$

A proper torsion is a rotation about a bond; thus it is the angle made between two bonds (Figure 5).

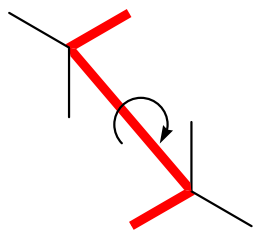


Figure 5: The torsion angle is defined by the angle formed by the three red bonds.

In flexible molecules the major changes in conformational arrangements are due to rotations about the bonds. Thus it is necessary that a force field can model these rotations effectively. The torsional term is usually represented by a cosine series expansion (equation 13) with torsional angle ω . The barrier height (V_n) gives a qualitative indication of the barrier to rotation present in a bond compared with another bond. Some force fields such as AMBER [37-40] use a single term cosine function for most of the torsions while others such as MM2 [41] use a larger expansion. The multiplicity (the number of minimum points in the function when the bond is rotated through 360°) of the torsion is represented by n and γ is the phase factor, which determines where the torsion passes through the minimum value.

$$V(\omega) = \sum_{n=0}^N \frac{V_n}{2} [1 + \cos(n\omega - \gamma)] \quad \dots(13)$$

Improper torsions or out of plane terms are also present in most force fields. An improper torsion is the energy needed to keep a sp^2 hybridised atom's molecular geometry planar. Either a cosine term (equation 14a) or a harmonic potential formula (equation 14b) can be used to force the improper torsion to be 0° or 180° .

$$V(\omega) = k(1 - \cos 2\omega) \quad \dots(14a)$$

$$V(\omega) = \frac{k}{2} \theta^2 \quad \text{or} \quad V(\omega) = \frac{k}{2} h^2 \quad \dots(14b)$$

Equation 14a is the most common approach as this term can be incorporated into the torsion terms. This equation takes into account the three atoms bonded to the sp^2 hybridised atom. Terms that are described by equation 14b are called out-of-plane terms. The out-of-plane energy is determined by a Hooke's law equation using either the out-of-plane angle or uncorrected height. The out-of-plane angle is the angle that the equilibrium bond would make with the horizontal plane if there was no out-of-plane torsion present and the uncorrected height is the

height that the third atom would be above the horizontal surface if the bond was uncorrected. These details are then used to determine the energy needed to counteract this equilibrium thus holding the torsion in the plane.

The non-bonded interactions term can be divided into electrostatic interactions and van der Waals interactions. The electronic structure of a molecule is often represented as an arrangement of point charges throughout the molecule. The electrostatic interactions are calculated as the interaction between each of these point charges. This is modelled by using a Coulomb's law formula (equation 15).

$$V = \sum_{i=1}^{N_i} \sum_{j=1}^{N_j} \frac{q_i q_j}{4\pi\epsilon_0 r_{ij}} \quad \dots(15)$$

q_i and q_j are the two charges, r_{ij} is the distance between the two charges and ϵ_0 is the permittivity of a vacuum.

The van der Waals interactions are divided into attractive interactions and repulsive interactions. The dispersive interactions are predominantly caused by London forces. London forces are caused by an instantaneous dipole, which arises due to a fluctuation in the electron cloud. This dipole can thus induce another dipole. The dispersive interaction is usually of the order of r^{-6} where r is the separation distance [32].

The repulsive interactions are often called exchange forces. These interactions are stronger the smaller the separation is. Often they are mathematically expressed as an exponential function or by a r^{-12} term [32].

The best-known function to model the van der Waals interaction is the Lennard-Jones 12-6 function (eq. 16).

$$V(r) = 4\epsilon \left[\left(\frac{\sigma}{r} \right)^{12} - \left(\frac{\sigma}{r} \right)^6 \right] \quad \dots(16)$$

where σ is the collision diameter (the separation distance at which the energy is at a minimum) and ϵ is the well depth (the energy value at the minimum).

5. Optimisation of the force field

The potential energy of the system is a complex, multidimensional function that is dependent on the atomic coordinates. As these coordinates change so the energy of the system will change thus leading to the formation of an energy hypersurface. It is necessary to determine the minimum or minima of this surface, as these will correspond to the coordinates of the favoured structures. The minima are found by applying optimisation procedures to the energy surface.

The minimum of a function $\varphi(\mathbf{x})$ is defined as the point(s) where the gradient is zero ($\frac{\partial\varphi(\mathbf{x})}{\partial x_i} = 0$) and the curvature is positive ($\frac{\partial^2\varphi(\mathbf{x})}{\partial x_i^2} > 0$). Optimisation methods are divided into non-derivative and derivative methods. As non-derivative methods are not useful in molecular mechanics only derivative methods will be discussed.

5.1. Derivative methods

Derivative methods are based on the Taylor expansion (equation 17) where $O(3)$ represents the terms of order three and higher and the prime implies differentiation with respect to position. The order of a method is the highest order of differentiation and the methods that will be discussed are all first order.

$$V(\mathbf{x}) = V(x_k) + (x - x_0)V'(x_k) + \frac{(x - x_0)^2 V''(x_k)}{2!} + O(3) \quad \dots (17)$$

The two most common derivative methods are steepest descent method and the conjugate gradient method.

5.1.1. Steepest descent method

The direction of a movement is defined by $\mathbf{d}_k = \frac{-\mathbf{g}_k}{|\mathbf{g}_k|}$ where \mathbf{g}_k is a vector that contains the partial derivatives of the function evaluated at a point x_k . The minimum can then be found using exact or approximate methods.

An inexact line search is carried out by bracketing the minimum of the function into a region in space. After each iteration the region in space is made smaller and smaller until the minimum is

found. This can be efficient if the original region is correctly captured but can be cumbersome, even leading to the function diverging, if the initial region was incorrectly chosen.

The initial step of an exact line search is to compute a step size α (equation 18). Then by using Lagrange multipliers a solution is readily found. The largest interatomic forces determine the direction of the gradient therefore relieving the highest energy features of the initial configuration.

$$\mathbf{x}_{k+1} = \mathbf{x}_k + \alpha \mathbf{d}_k \quad \dots(18)$$

A problem associated with line search methods is that the method is forced to make a perpendicular turn at each point, which could lead to the function diverging away from the true minimum.

5.1.2. Conjugate gradient methods

This method does not have the same perpendicular problem as the steepest descent method thus error build-up is less. In this method the gradient at each point is perpendicular but the directions are conjugated (equation 19). Other methods such as Polak-Ribiere and Fletcher-Reeves are known to solve for γ_k

$$\mathbf{v}_k = -\mathbf{g}_k + \gamma_k \mathbf{v}_{k-1} \quad \dots(19)$$

$$\text{where } \gamma_k = \frac{\mathbf{g}_k \cdot \mathbf{g}_k}{\mathbf{g}_{k-1} \cdot \mathbf{g}_{k-1}}$$

The problem with optimisation methods is that they only find the local minimum, so it does not guarantee that for a specific molecule the global energy minimum conformation is found. A technique of simulated annealing is used to help find the global minimum [33].

6. Simulated annealing

Since many molecules have many degrees of freedom many possible structures are possible dependent on the initial structure given to the force field. In a simulated annealing calculation energy is added to the system in the form of extreme heat. This is a temperature at which all

barriers of rotation can be overcome. The system is then slowly cooled before minimisation. This allows the user to determine the most stable conformation of a specific molecule, which may or may not be the global minimum [33].

7. Aim

The aim of this project was to develop a predictive tool for the modelling of bisphosphonates and their interaction with hydroxyapatite, the principal mineral in bone to determine which bisphosphonates interact favourably with the hydroxyapatite so as to allow *in vivo* research into those interactions. This would be one component of a knowledge base for the design of novel compounds to be screened as potential agents for the treatment of bone cancer.

This was to be achieved by completing a series of 'sub-aims'. These 'sub-aims' included developing and testing a force field for the modelling of the bisphosphonates. Once this was achieved it was necessary to extend and test this force field for the modelling of the hydroxyapatite surface. Finally this force field was to be used to model the interactions of a series of these bisphosphonates with the various faces of hydroxyapatite. These aims were to be achieved by using a series of tools including molecular orbital theory, molecular mechanics, molecular dynamics and simulated annealing.

Chapter 2: Experimental

1. Choice of force field parameterisation

Bisphosphonates (BPs) are highly charged molecules thus it was necessary to take electrostatic contributions into account when using molecular modelling. This criterion and the size of the BPs were used to determine which force field parameterisation to use.

All molecular modelling calculations were performed using Hyperchem version 7.03 [42]. The force fields available in this suite of programmes are MM+ (a force field equivalent to Allinger's MM2 [41] or MM3 [43]), AMBER [37,40], BIO+ (a force field equivalent to CHARMM [44]) and OPLS [45,46].

MM2 and MM3 are force fields designed predominantly for small hydrocarbons. The charge distribution for a molecule is determined by summing the contribution from the van der Waals interactions and the electrostatic interactions. The electrostatic interactions are calculated by assigning a polarisation to each bond. This energy is calculated by using the bond dipole moments. This method is sufficient for relatively non-polar molecules as the dipole moment for a specific bond type will be approximately the same for any molecule but for a polar molecule the dipole moment will vary drastically depending on the molecular structure [41,43]. As the BPs are highly polar this force field is inappropriate for this project. CHARMM (Chemistry at Harvard Macromolecular Mechanics) is a programme that uses empirical functions to model macromolecular systems, by separating the macromolecules into atomic units. This force field models electrostatics well but since the bisphosphonates are small molecules it is not appropriate. OPLS (Optimised Potentials for Liquid Simulations) was developed to simulate proteins in their native environment, thus modelling is done to mimic an aqueous environment. While this force field models electrostatic interactions well it is still inappropriate as the BP molecules do not fall into the set of molecules for which the force field was developed [45,46].

The AMBER [37,40] (Assisted Model Building and Energy Refinement) force field was designed to model the simulations of nucleic acids and proteins. The parameterisation of this force field takes both van der Waals and electrostatic interactions into account [37-40]. Various

versions of AMBER [37,40] are available for protein studies but a new force field called GAFF [47] (Generalised AMBER Force Field) has been developed for small molecules using the AMBER parametrisation [37,40]. This force field parameterisation was the one used in this project.

1.1. GAFF force field

The GAFF force field contains parameters that adequately model most organic compounds that contain only carbon, hydrogen, oxygen, nitrogen, sulfur, phosphorus and halogens. The total strain energy, E_s , is the summation of terms associated with bond stretching, angle bending, torsional strain, electrostatic interactions, and van der Waals interactions.

Bond stretching is handled in GAFF using a simple harmonic function (equation 20) for which the equilibrium bond length, r_0 , was obtained from either the equilibrium bond lengths in the original AMBER [37,40] force field, from *ab initio* calculations using a MP2/6-31G* basis set, or from crystal structures.

$$E_{str} = k_{str} (r - r_0)^2 \quad \dots (20)$$

The bond stretching force constants were obtained by using equation 21,

$$k_{str} = K_{ij} \left(\frac{1}{r_{ij}}\right)^m \quad \dots (21)$$

where $K_{ij} = \frac{K_{ii} |r_{ij}^{ref} - r_{jj}^{ref}| + K_{jj} |r_{ij}^{ref} - r_{ii}^{ref}|}{|r_{ij}^{ref} - r_{jj}^{ref}| + |r_{ij}^{ref} - r_{ii}^{ref}|}$; r_{ij} is the bond length obtained from crystallographic data and m is a power order. The values of K_{ij} and m were parameterised by means of least squares fitting to C—C, C—N and C—O bond length experimental data, and the original AMBER bond length parameters [40] were used. For other bond parameters, model molecules were constructed on which high level *ab initio* vibrational frequency analysis was performed. The force constants were optimised using Parmscan [48]. Parmscan is an automatic force field parameter optimisation programme.

The angle bending term in the GAFF force field is also handled by a simple harmonic function (equation 22) for which the equilibrium bond angle is obtained in the same manner as the equilibrium bond length.

$$E_{\theta} = k_{\theta} (\theta - \theta_0)^2 \quad \dots (22)$$

The angle bending force constant is calculated using equation 23.

$$k_{\theta} = 143.9 Z_i C_j Z_k (r_{ij} + r_{jk}) \theta_{ijk}^{-1} \exp(-2D) \quad \dots (23)$$

where $D = \frac{(r_{ij} - r_{jk})^2}{(r_{ij} + r_{jk})^2}$; Z_i and Z_k are empirical values for the first and third atom in the bond and

C_j is an empirical value for the central atom in the bond. These were derived by using two hundred and fifty two bond angle parameters from the AMBER force field [37,40].

GAFF treats the energy obtained from the torsional bending as a cosine function (equation 24, where V_i is a force constant, n is the multiplicity and ϕ is the torsional angle), whereas most parameterisations contain one general term V_1 . These values were obtained by initially scanning a series of torsional angles at the MP4/6-31G(d,p)/MP2/6-31G* level. These were modified by use of Parmscan [48] to derive the torsional angle potential to reproduce the *ab initio* rotational profile.

$$E_{\text{torsion}} = \frac{k_i}{2} [1 + \cos(n\phi - \gamma)] \quad \dots (24)$$

The energy for an electrostatic interaction is obtained from Coulomb's law (equation 25) where q_i and q_j are the charges of the atoms and r_{ij} the separation distance.

$$E_{\text{charge}} = \frac{1}{4\pi\epsilon_0} \frac{q_i q_j}{r_{ij}} \quad \dots (25)$$

The energy for a non-bonded interaction is calculated in GAFF [47] by a 6-12 Lennard-Jones potential (equation 26)

$$E_{\text{non-bonded}} = \frac{A_{ij}}{r_{ij}^{12}} - \frac{B_{ij}}{r_{ij}^6} \quad \dots (26)$$

where

$$A_{ij} = \left(\frac{r_i^*}{2} + \frac{r_j^*}{2} \right)^{12} \sqrt{\epsilon_i \epsilon_j} \quad \text{and} \quad B_{ij} = 2 \left(\frac{r_i^*}{2} + \frac{r_j^*}{2} \right)^6 \sqrt{\epsilon_i \epsilon_j}$$

In this function, $\frac{r_i}{2}$ is half the minimum energy separation for two atoms of type i, and ε_i is the well depth for two atoms of type i [40,47].

2. Crystal structures

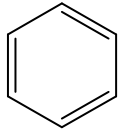
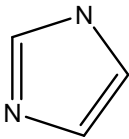
Initially it was necessary to test the GAFF force field to determine if this force field modelled bisphosphonates accurately. The structures were obtained from the Cambridge Structural Database (CSD) [49], which is a database of crystallographic structures for small organic molecules. A search was carried out on the CSD version 5.26 (November 2004) for all molecules that contained a PO₃-C-PO₃ backbone but exclusions for molecules containing a O-P group or a third P group off the central carbon and coordinated metal species were excluded (Results in Appendix). The search was restricted to crystal structures that met the following criteria: 3D coordinates are reported; not disordered; no errors; no powder structures; not polymeric; R-factor < 0.0075. The reason for these criteria was so that the crystal structures examined are reliable. The R-factor is a calculation of how well the charge density of a XRD pattern is matched to that of the structure obtained. Therefore the lower the R-factor the better the fit. The CSD results contain various structural information such as structural formula, compound name, density, crystallisation temperature and crystallographic data. Each structure is given a randomly generated CSD reference code. The results obtained contained sixty one structures (Table A1 of the Appendix) but one structure was excluded from the modelling (Table A2 of the Appendix).

2.1. Preparation of crystal structures for molecular modelling

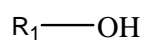
These structures were obtained as textfiles, which were converted to .ent files (see Appendix), which are readable by Hyperchem [42]. These .ent files were then opened in Hyperchem [42], where solvent molecules and counter ions were erased. These modified files were saved as .hin files (see Appendix), which are Hyperchem [42] specific files that contain both information for the spatial coordinates and the connectivity of the molecule.

Once the files were converted to Hyperchem [42] compatible files all atoms were assigned atom types. An atom type contains information about the nucleus including atomic number, geometry of the atom, spin multiplicity and atomic charge [33]. The atom types used in this project were obtained from the GAFF parameter files [47] (Table 2).

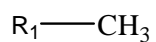
Table 2: Definition of atom types

Atom	Structural Representation	Atom Type
Carbon	$\begin{array}{c} R_1 \\ \\ R_4 - C - R_2 \\ \\ R_3 \end{array}$	C3
		CA
		CC
Phosphorus	$\begin{array}{c} O \\ \\ P \\ / \quad \backslash \\ \quad \quad \end{array} \quad \text{or} \quad \begin{array}{c} \\ P \\ / \quad \backslash \\ \quad \quad \end{array}$	P5
Oxygen	$\begin{array}{c} \quad \quad \quad O \\ \quad \quad \quad \\ \quad \quad C \\ / \quad \backslash \end{array} \quad \text{or} \quad \begin{array}{c} O \\ \\ P \\ / \quad \backslash \\ \quad \quad \end{array}$	O
	$R_1 - OH$	OH
	$\begin{array}{c} \\ P \\ / \quad \backslash \\ \quad \quad O - R_1 \end{array}$	OS

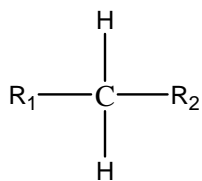
Hydrogen



HO



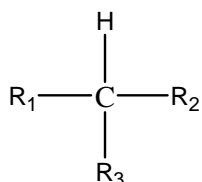
HC but if R_1 is an electron withdrawing group then H1



H2

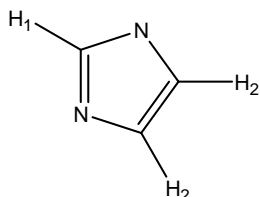
R_1 and R_2

electron withdrawing groups



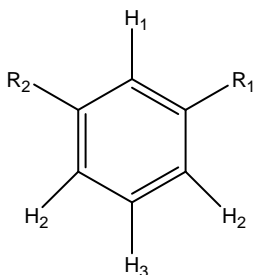
H3

R_1 , R_2 and R_3 electron withdrawing



H4 is a hydrogen next to two electron withdrawing groups.

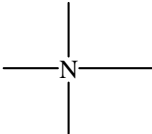
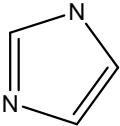
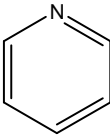
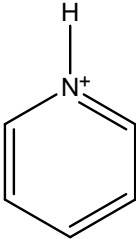
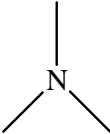
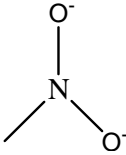
H5 is a hydrogen next to one electron withdrawing group.



HA is an aromatic hydrogen

Any hydrogen on a nitrogen

HN

Nitrogen		N4
		NC
		NB
		NA
		N
		NO
Chlorine	Any chlorine	Cl

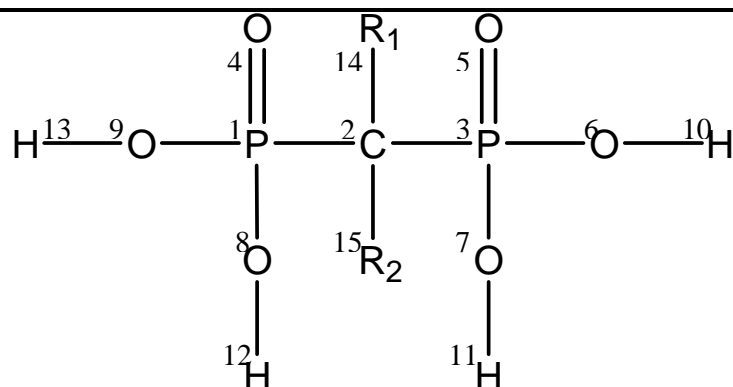
In addition, it was necessary to number the atoms in the structures in a consistent manner as the code (example in Appendix) we wrote to obtain statistical information about the structures references specific atom numbers. Since the structures obtained from the CSD contains both acids and ester derivatives of varying degrees of protonation, the structures were divided into eight categories dependent on functionality and degree of protonation. The number system adopted is given in Table 3.

Table 3: Numbering system

Group	Numbering
Acids	
No protons present	
1 proton present	
2 protons present	
3 protons present	

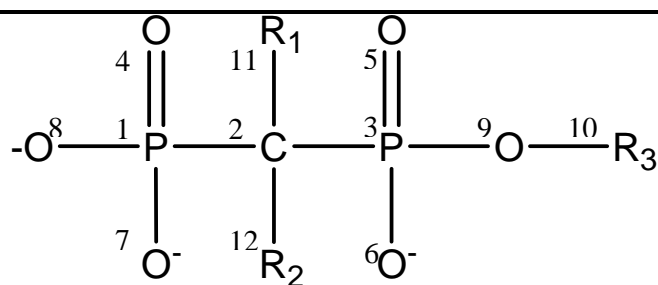
Group**Numbering**

4 protons present

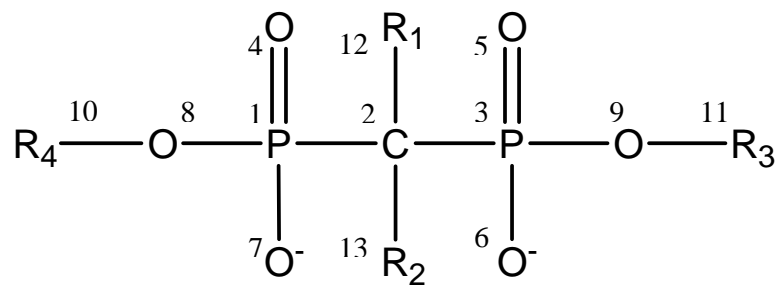


Ester Derivatives

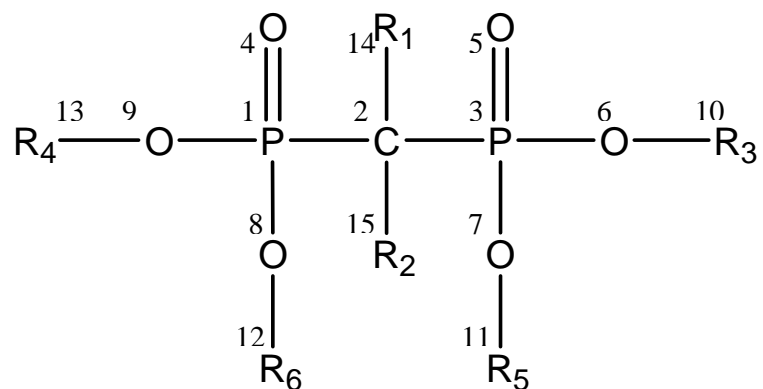
1 R- group present



2 R-groups present



4 R-groups present



2.1.1. Allocation of partial charges

The AMBER force field [37,40] parameterisation has an electrostatic interaction term thus partial charges for the atoms were determined. Restricted Hartree-Fock (RHF) *ab initio* calculations using Hyperchem [42], with a 6-31G* basis set and convergence limit 1×10^{-5} kcal mol⁻¹ with accelerated convergence, were performed to determine these partial charges (Figure 6).

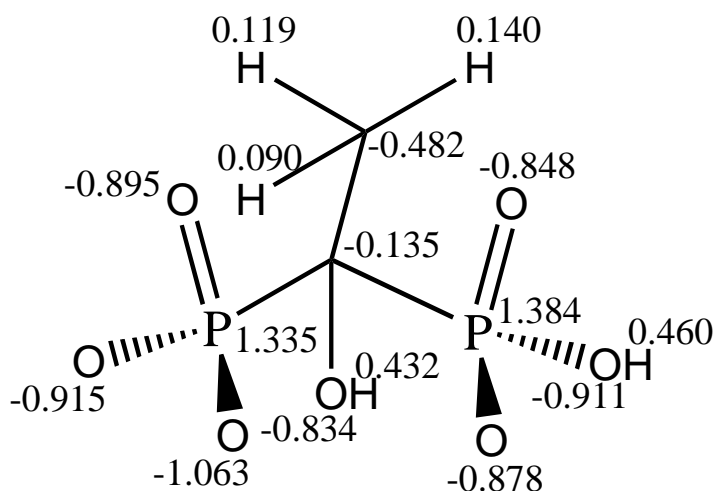


Figure 6: Example of a charge distribution for a bisphosphonate

The most common basis sets are the Slater functions and the Gaussian basis sets. The Slater orbitals consist of integrals that are computationally demanding, it is more efficient to use the Gaussian basis sets. These basis sets have the form:

$$x^a y^b z^c \exp(-\alpha r^2)$$

where (x,y,z) are the spatial coordinates raised to integral powers a,b and c and α is the radial extent of the Gaussian function. The radial spread is inversely proportional to α . A major advantage of Gaussian basis sets is that the product of two Gaussians is also a Gaussian, which is located along the centre of the two original Gaussians. A single Gaussian function is insufficient to model a system, as a Gaussian function does not have a cusp at the origin and it decays towards zero quicker than the Slater orbital. This problem is easily overcome by using a linear combination of Gaussian functions (Figure 7) but these calculations are cumbersome.

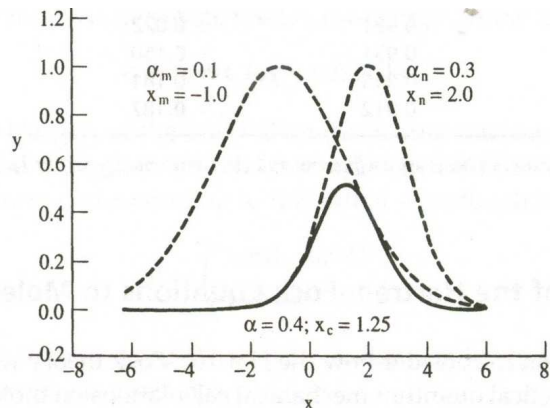


Figure 7: Illustration that the linear combination of two Gaussian orbitals is a Gaussian orbital [33].

The size of the basis set that is used is dependent on computer efficiency and accuracy needed. The smallest basis sets available are the minimal basis sets that contain just the number of functions that are required to fill all the orbitals in the shell. The minimal basis sets are known to have deficiencies for compounds containing atoms that are near the end of a period such as oxygen or the halogens [33]; thus a minimal basis set was insufficient for this project as the BPs are rich in oxygen. These problems can be addressed if more than one function is used to represent each orbital. Basis sets with these functions are called double zeta basis sets but again these calculations are computationally cumbersome. An alternative is to use the split valence approach. These basis sets separate the valence electrons from the inner core electrons. The rationale to this approach is that the inner electrons have a minimal effect on the chemical properties of a compound, as these properties are largely a consequence of the valence electron configuration the inner core electrons can be represented by one function each while the valence electrons require more than one function. These functions can also take into account polarisation and this is denoted by a single asterisk for polarisation of all the non-hydrogen atoms and a double asterisk for the polarisation of all the atoms. The basis set used in this project was the split valence with polarisation of the heavy atoms, 6-31G* [33].

In addition partial charges were also determined by semi-empirical methods, as certain BPs were too large for *ab initio* methods. Semi-empirical methods are divided into two main categories, either single Hückel method or Pariser-Parr-Pople method. The Hückel method is a one-electron theory whereas Pariser-Parr-Pople is a two-electron theory. An assumption that all semi-

empirical methods make is in the treatment of π electrons in non-planar molecules, where the valence electrons are considered together rather than separately. Various semi-empirical methods are available in the Hyperchem suite [42] but it was decided to use the PM3 method [50]. PM3 [50] is a two-electron theory that has parameters for twenty four elements including all the elements present in the bisphosphonates. In addition PM3 [50] models the geometry and dipole moments of a wide range of molecules reasonably accurately [32].

3. Preparation of the force field

A problem associated with the AMBER [37,40] force field in Hyperchem [42] is that it is impossible to determine if all needed parameters are present in the force field parameter files. The coding instructs the software to use “dummy” parameters for unknown parameters thus leading to errors in the modelling of structures. This problem was overcome by setting up a test set of parameter files and monitoring for missing parameters using the MM+ force field [41,42,51] which reports missing parameters. The test parameters were obtained by running a log file on each structure while running a minimisation code on the structure using the MM+ Force Field [41,42,51]. The log file (example in the Appendix) lists all the missing parameters from the test files.

These parameters were added to the test parameter files (in MM+ format [41,42,51]) and to WitsGAFF (our version of GAFF parameter files, from the GAFF parameter files [47]). Once all the structures were tested it was found that additional parameters needed to be added to the parameter files (Table 3). Additional bond stretching parameters were obtained from the AMBER99 [39] parameters. These parameters were optimised for our system by performing force field calculations (1000 iterations of steepest descent algorithm) on known crystal structures. The minimised bond lengths were compared with the original crystal structures bond lengths. According to the difference seen between the two structures the parameters were modified. This method was repeated until the reproducibility of the bond lengths was good. The angle parameters were obtained either from the AMBER99 [39] parameter files or by using the method determined by the developers of GAFF [47]. The additional torsions, improper torsions and non-bonded interactions were obtained either from AMBER99 [39] or by using the parameters for a similar atom type in GAFF [47]. The complete parameter files are saved on the disk attached to the Appendix.

Table 4: Additional parameters added to GAFF for the modelling of bisphosphonate ligands^a

Additional angle bending parameters			
Parameter	θ_0 /degrees	k_0 /kcal mol ⁻¹ deg ⁻²	Comments
H2-C3-P5	53.8	109.64	AMBER99 [39]
OH-C3-P5	84.2	105.3	θ_0 from crystal structures k_0 calculated from equation 23
H5-CA-NA	51.9	114.95	AMBER99 [39]
C3-CA-NA	66.4	109.16	θ_0 from crystal structures k_0 calculated from equation 23
H3-C3-P5	53.8	109.64	AMBER99 [39]
H3-C3-N	50.0	108.93	AMBER99 [39]
H1-C3-N4	49.0	107.90	AMBER99 [39]
H3-C3-N4	49.0	107.90	AMBER99 [39]
NA-CA-NH	71.4	120.98	AMBER99 [39]
NH-C3-P5	82.4	107.70	θ_0 from crystal structures k_0 calculated from equation 23
Cl-C3-P5	80.2	110.00	θ_0 from crystal structures k_0 calculated from equation 23
N-C3-P5	81.3	110.50	θ_0 from crystal structures k_0 calculated from equation 23
N4-C3-P5	80.8	114.00	θ_0 from crystal structures k_0 calculated from equation 23
CA-C3-P5	78.9	109.70	θ_0 from crystal structures k_0 calculated from equation 23
OH-P5-OH	43.7	106.40	θ_0 from crystal structures k_0 calculated from equation 23

Parameter	θ_0 /degrees	k_0 /kcal.mol ⁻¹ deg ⁻²	Comments
CA-OS-P5	87.9	97.00	θ_0 from crystal structures k_0 calculated from equation 23
P5-C3-Br	82.4	108.50	θ_0 from crystal structures k_0 calculated from equation 23
C-CA-NA	67.5	118.00	θ_0 from crystal structures k_0 calculated from equation 23
O-CA-NA	74.9	119.70	θ_0 from crystal structures k_0 calculated from equation 23
C3-OS-NA	64.5	110.40	θ_0 from crystal structures k_0 calculated from equation 23

Additional improper torsion parameters

Parameter	$V_i/2$ /kcal mol ⁻¹	γ /deg	n	Comments
__CA_**	1.10	180	2	Preliminary value, similar to improper torsion parameters in GAFF[47]
__NA_**	1.10	180	2	Preliminary value, similar to improper torsion parameters in GAFF[47]

Additional non-bonded parameters

parameter	R^* /Å	ϵ /kcal mol ⁻¹	Comments
C0	1.7131	0.459789	AMBER99[39]

Additional torsion parameters

Parameter	Periodicity	$V_i/2$ / kcal mol ⁻¹	γ /deg	N
C2-N3	4	1.20	180.00	2.00

^aThe symbol ** is a wildcard symbol and refers to any atom

4. Modelling of the bisphosphonates (BPs)

Energy minimisation was performed using one thousand iterations of a steepest descent algorithm followed by one thousand iterations of a Polak-Ribiere conjugate gradient algorithm, or until reaching the converge criteria of $0.01 \text{ kcal } \text{\AA}^{-1} \text{ mol}^{-1}$ on crystallographic structures.

The minimised structures were compared with the crystal structures. Fits were deemed acceptable if bond lengths were reproduced to within 0.01 \AA , bond angles to within 2° , and torsions to within 4° [52]. A problem was faced in determining the accuracy of the torsional parameters as there was free rotation about all the central bonds in the BPs. Subsequently various conformational isomers were obtained for each structure. The minimised torsional angles were checked by plotting the torsional distribution of each angle (see Figures A1 –A4 of the Appendix). It was seen that the torsional angles all occurred at angles of approximately $60n^\circ$ where $n = 0,1,2,3$. This was as predicted as at these angles the through-space interactions of the substituents are minimised.

In addition it was necessary to determine if these minima were the global or only the local minimum. This was explored by performing a simulated annealing on alendronate ($R_1 = \text{OH}$, $R_2 = \text{C}_3\text{H}_6\text{NH}_3$). The investigation was performed independently on five different alendronate structures. The difference in these structures was in the number of protons present on the phosphonate groups ranging from no protons (fully deprotonated) to four protons present (fully-protonated). The system was heated from 0 K to 500 K over a period of 5 ps. It was held at 500 K for 50 ps and subsequently allowed to cool (over a period of 10 ps) to 0 K. This allowed the structure to overcome any barriers to rotation and to anneal into what is hopefully the global energy minimum structure. These structures were compared with the minimum structures obtained from the force field calculation.

5. Interactions with the bone surface

5.1. The hydroxyapatite surface, $\text{Ca}_5(\text{PO}_4)_6(\text{OH})_2$

The crystal structure reported by Kay and co-workers [53] was used for the modelling of hydroxyapatite. The cell information was obtained from the Inorganic Crystallographic Structural Database [54] and then solved by direct methods using SHELXS-97 [55] and WINGX [56]. Non-hydrogen atoms were first refined isotropically followed by anisotropic refinement by

full matrix least-squares calculation based on F^2 using SHELXS-97 [55]. Hydrogen atoms were positioned geometrically and allowed to ride on their respective parent atoms. The crystal structure was grown in Mercury 1.4 [57] to obtain $1 \times 3 \times 3$, $3 \times 1 \times 3$ and $3 \times 3 \times 1$ crystals to represent the (100), (010) and (001) faces of hydroxyapatite (Figure 8). These were then converted into a Hyperchem-compatible format, and atom types were assigned. The atom type C0 was added to the force field parameter files to represent calcium; the calcium parameters were obtained from the parameter files of AMBER99 [39]. A single point restricted Hartree-Fock (RHF) *ab initio* calculation using Hyperchem [42] with a 6-31G* basis set was performed on the unit cell of hydroxyapatite (Figure 9) and the average partial charge for each atom type was allocated to the entire matrix.

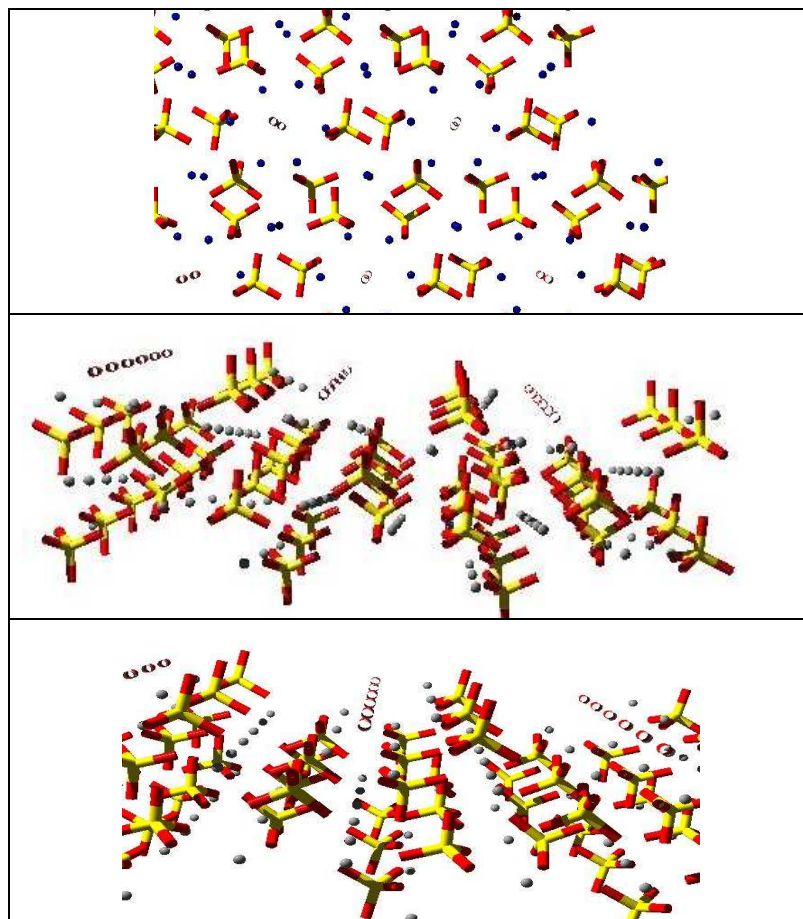


Figure 8: (001), (010) and (100) faces of hydroxyapatite

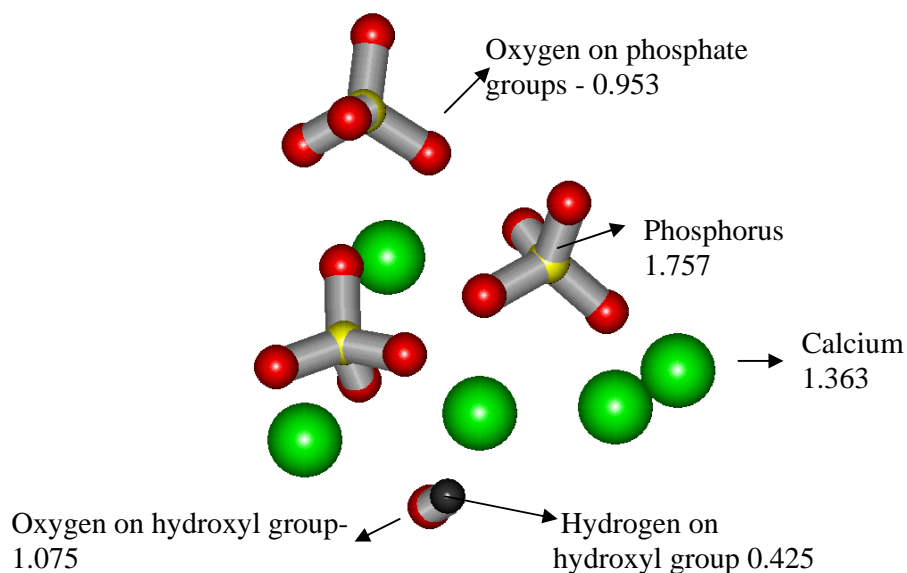


Figure 9: Partial charges for smallest unit of hydroxyapatite, $\text{Ca}_5(\text{PO}_4)_6(\text{OH})_2$

5.2. Interactions of the bisphosphonates with the hydroxyapatite surface

An investigation of the interactions was performed for five BPs namely, MDP ($R_1 = R_2 = \text{H}$, Figure 1), HEDP ($R_1 = \text{OH}$, $R_2 = \text{CH}_3$), APD ($R_1 = \text{OH}$, $R_2 = (\text{CH}_2)_2\text{NH}_3^+$), alendronate ($R_1 = \text{OH}$, $R_2 = (\text{CH}_2)_3\text{NH}_3^+$) and neridronate ($R_1 = \text{OH}$, $R_2 = (\text{CH}_2)_5\text{NH}_3^+$) with the hydroxyapatite surface. The appropriate protonation of each ligand at serum pH levels (7.2) was used, utilising the known $\text{p}K_a$ values [58] or values that have been determined in our laboratory (Table 5). The charge distributions for the chosen ligands are given in Table 6.

Table 5: Unpublished acid dissociation constants determined by glass electrode potentiometry in our laboratory (298 K and $\mu=0.15$ M NaCl)

	$\text{p}K_1$	$\text{p}K_2$	$\text{p}K_3$	$\text{p}K_4$
APD	1.85(1)	5.760(3)	9.62(1)	12.050(3)
alendronate	2.07(1)	6.10(1)	10.498(5)	11.41(1)
neridronate	2.36(1)	6.43(1)	10.86(1)	11.21(1)

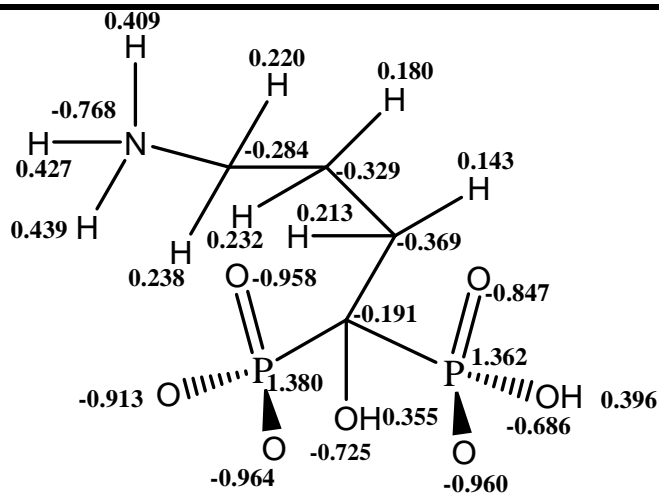
Table 6: Partial charges on five bisphosphonate ligands in their mono-protonated and di-protonated forms as determined from a SCF-RHF calculation at the crystal structure geometry using a 6-31G* basis set

Structure	Charge Distribution/ electron units
Mono-protonated species	
MDP	
HEDP	
APD	

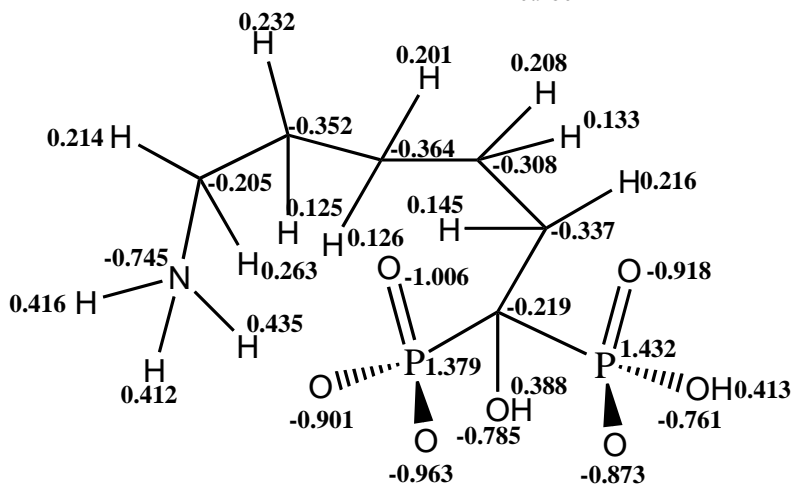
Structure

Charge Distribution/ electron units

Alendronate

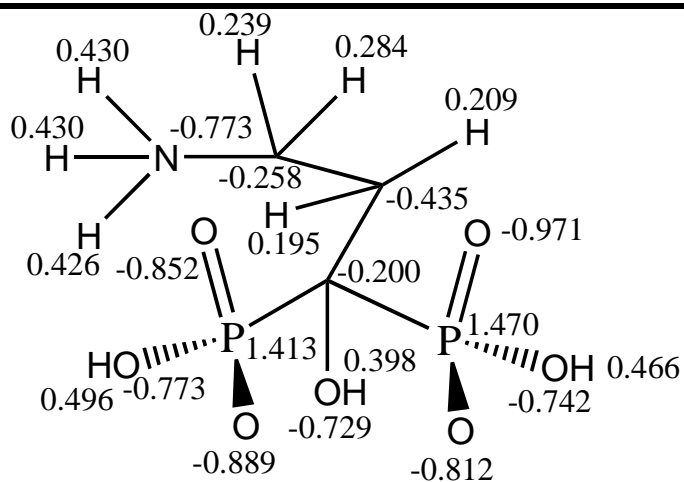


Neridronate



Di-protonated Species

APD



Structure	Charge Distribution/ electron units
Alendronate	
Neridronate	

The interaction energies were calculated by initially minimising the energy of a bisphosphonate far (ca. 20 Å) from the hydroxyapatite surface (Polak-Ribiere conjugate gradient, convergence criterion of 0.01 kcal Å⁻¹ mol⁻¹) whilst all atoms of hydroxyapatite were fixed in the position found in the crystal structure. The ligand was then brought closer to the surface (ca. 8 Å); energy minimisation (using the same method and convergence criterion) caused the ligand to relax onto the hydroxyapatite surface. The difference in strain energies between the two systems is the interaction energy. This was repeated twenty times, each with a different, random orientation of the ligand relative the hydroxyapatite surface. The reported interaction energy is the mean of the twenty individual minimisations. As we wished to mimic an aqueous environment a relative permittivity of 78ε₀ was used. A series of tests for various relative permittivity was performed on HEDP and APD to determine the effect of the relative permittivity on the energy minimisation.

The reason that these structures were chosen is that HEDP is a first generation bisphosphonate and APD is a second generation bisphosphonate, which has the amine chain present. Using these two structures it was possible to determine the contribution of the relative permittivity to the bisphosphonate backbone and to the amine chain separately.

Chapter 3: Results and Discussion

1. Modelling of bisphosphonates

The atom types for the bisphosphonate backbone are given in Figure 10.

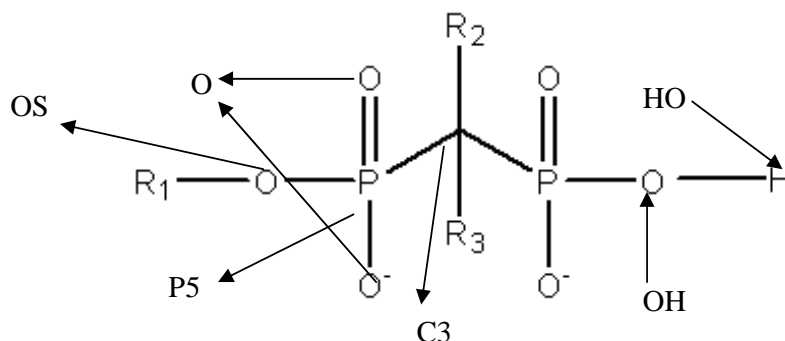


Figure 10: Atom types for the bisphosphonate backbone

The partial charges for each of the structures were determined and the mean charges for the atom types are in Table 7. As the standard deviation for most of the atom types (other than C3 and OS) is small (less than 0.1) it is sufficient to use these averages for future calculations. The large standard deviation in the C3 charge is due to the large variation present in the nature of the R₂ and R₃ substituents of the central carbon. Some of the bisphosphonate structures have strong electron-withdrawing substituents whereas others have electron-donating substituents- therefore the charge on C3 will fluctuate accordingly. The large standard deviation for OS is due to the size of the sample set, which contains only thirty two entries. The charge distributions for the P5, C3, O, OH and HO atom types are in the Appendix Figures A5-A9.

Table 7: Partial charge distribution for bisphosphonate backbone atom types

Atom Type	Sample Size	Average Charge /electron units
P5	102	1.47 ± 0.08
C3	61	-0.35 ± 0.21
O	167	-0.82 ± 0.08

OH	138	-0.75 ± 0.09
OS	32	-0.82 ± 0.17
HO	138	0.44 ± 0.09

1.1. Semi-empirical methods versus *ab initio* calculations

Originally only *ab initio* calculations (RHF method) were used to calculate the charge distributions for the bisphosphonates. Unfortunately four of the ester derivative bisphosphonates (IGUMAY [59], JOTVET [60], MUSLUH [61], PAWTUC [62]) were too large to be studied and it was therefore necessary to use semi-empirical methods. A test was performed on the other five ester derivatives (CAKKEF [63], IGUMEC [59], ZARJAD [64], ZARJEH [64], ZARJIL [64]) to determine if the semi-empirically calculated charges were sufficient. The charge distributions for these structures were determined using both a RHF *ab initio* method and by a PM3 semi-empirical method. The structures were minimised by the force field and the results for the bond lengths and bond angles compared. All the bond lengths obtained using the semi-empirical method to calculate the charges, other than the C3-C3 (central carbon on backbone- R₁ = sp³ carbon) bond, were within 0.0003 Å of the *ab initio* calculated bond lengths. As these differences are less than the standard deviation for the *ab initio* calculated bond lengths the two methods can be seen as statistically equivalent. The difference between the minimised lengths for the C3-C3 bond using the two methods was 0.0013 Å. All the semi-empirical modelled bond angles were within 0.3° of the *ab initio* bond angles. This difference was acceptable as they are all within one standard deviation of the *ab initio* structures (Table 7). It was decided to use the PM3 semi-empirical method to calculate the charge distributions for the large BP esters.

Table 8: Comparison of bond lengths and bond angles obtained using structures with partial charge distributions obtained from PM3 and RHF methods

Parameter	PM3	RHF	Difference
Bond Lengths/ Å			
P5-C3	1.823 ±0.003	1.823 ±0.003	0.000
P5-O	1.495 ±0.022	1.495 ±0.022	0.000
P5-OS	1.611 ±0.003	1.611 ±0.003	0.000
OS-C3	1.558 ±0.200	1.558 ±0.200	0.000
OS-CA	1.624 ±0.590	1.624 ±0.589	0.000
C3-Cl	1.789 ±0.001	1.789 ±0.000	0.000

C3-H2	1.100 ^a	1.100 ^a	0.000
C3-OH	1.432 ±0.001	1.432 ±0.001	0.000
C3-C3	1.545 ±0.005	1.544 ±0.004	0.001
Parameter	PM3	RHF	Difference
Bond Angles/ degrees			
P5-C3-P5	115.1±0.7	115.0±0.7	0.1
O-P5-O	111.2±0.4	111.5±0.7	0.3
O-P5-OS	115.1±1.4	115.0±1.5	0.1
OS-P5-OS	104.8±3.6	104.8±3.5	0.0
O-P5-C3	112.1±65.4 ^b	112.1±65.4	0.0
OS-P5-C3	104.0±5.4	103.9±5.2	0.1
P5-OS-C3	119.4±2.1	119.4±2.0	0.0
P5-OS-CA	89.1±36.6	89.1±36.6	0.0
P5-C3-Cl	108.4±0.1	108.4±0.1	0.0
P5-C3-H2	83.3±16.2	83.3±16.2	0.0
P5-C3-OH	104.5±0.7	104.6±0.7	0.1
P5-C3-C3	112.1±0.6	112.0±0.9	0.1

^a Single observation available

^b The large standard average is due to the arms of the substituents aligning differently in space

2. The modelling of the ligands

GAFF reproduced the structures of the bisphosphonate ligands reasonably well (Table 9 and Table 10). Bond lengths were reproduced on average to within 0.015 Å of the crystallographic mean value, or within 1.2 mean standard deviations of the experimental observations, whilst bond angles were on average reproduced to within 1.9° (0.8σ). Significant differences in bond lengths occur with P–O⁻ bonds which, in the solid state structures (average 1.512 ± 0.014 Å) are somewhat longer than in the molecular mechanics model (1.481 ± 0.001 Å) and P–OH bonds (1.570 ± 0.030 Å observed; 1.628 ± 0.001 Å calculated) are somewhat shorter. There is a distinct possibility that ambiguity in the state of protonation of a phosphonate oxygen in the solid state structures has led to experimental error when the structures are solved. Bonds between the sp³ C

of the bisphosphonate and an aromatic carbon (1.516 ± 0.034 Å observed; 1.539 ± 0.001 Å calculated) are also somewhat longer in the modelled structures than observed in the solid state.

Because of free rotation about the P–C bonds, it is difficult to compare directly the torsional angles. The torsional distributions for the backbone torsions (this excludes torsion involving H atoms as H atoms are generally not observable in structures obtained by x-ray diffraction methods) are seen in the Appendix Figure A1-A4. In virtually all structures, groups adopt either a gauche or anti conformation (which is reproduced in the modelling) but in several cases gauche conformations observed in the solid state energy-minimised into anti conformations, and vice versa.

Table 9: Comparison of the bond lengths and bond angles of bisphosphonate ligands observed crystallographically and those predicted using molecular mechanics and GAFF

Parameter	Solid state	Standard Deviation	Modelled	obs-calc	n σ^a
	Average (obs)		Average (calc)		
Bond lengths /Å					
P5-C3	1.841	0.010	1.830	0.011	1.10
P5-O	1.512	0.014	1.481	0.031	2.21
P5-OH	1.570	0.030	1.628	0.058	1.93
C3-C1	1.791	0.008	1.791	0.000	0.00
C3-OH	1.446	0.005	1.437	0.009	1.80
C3-C3	1.535	0.008	1.551	0.016	2.00
C3-NH	1.468	0.010	1.467	0.001	0.10
C3-N4	1.516	0.001	1.515	0.001	1.00
C3-N ^b	1.478		1.483	0.005	
C3-CA	1.516	0.034	1.539	0.023	0.68
Bond Angles /degrees					
P5-C3-P5	113.7	2.5	115	1.3	0.52
O-P5-O	114.5	1.9	111.2	3.3	1.74
O-P5-OH	110.6	2.7	112.1	1.5	0.56

OH-P5-OH	106.4	0.7	105.5	0.9	1.29
O-P5-C3	108.5	1.6	110.2	1.7	1.06
Parameter	Solid state		Modelled		
	Average (obs)	Standard Deviation	Average (calc)	obs-calc	$n\sigma^a$
OH-P5-C3	105	1.1	103.8	1.2	1.09
P5-C3-Cl	108.4	1.2	108.5	0.1	0.08
P5-C3-OH	105.3	3.1	104.8	0.5	0.16
P5-C3-C3	104.6	8.1	105.9	1.3	0.16
P5-C3-NH	107.7	1.1	107.6	0.1	0.09
P5-C3-N4	110.6	0.1	110.8	0.2	2.00
P5-C3-N	110.5	1.2	109.5	1.0	0.83
P5-C3-CA	109.7	1.2	109	0.7	0.58

^aThe difference between the mean observed and mean calculated parameter expressed as the number (n) of standard deviations (σ) of the experimental observations.

^bSingle observation available

Table 10: Comparison of the bond lengths and bond angles of bisphosphonate ester ligands observed crystallographically and those predicted using molecular mechanics and GAFF

Parameter	Solid state	Standard	Modelled	obs-calc	$n\sigma^a$
	Average (obs)	Deviation	Average (calc)		
Bond lengths /Å					
P5-C3	1.852	0.019	1.823	0.029	1.53
P5-O	1.486	0.021	1.495	0.009	0.43
P5-OS	1.584	0.009	1.611	0.027	3.00
OS-C3	1.526	0.243	1.558	0.032	0.13
C3-Cl	1.794	0.003	1.789	0.005	1.67
C3-OH	1.428	0.005	1.432	0.004	0.80

C3-C3	1.544	0.010	1.544	0.000	0.00
Parameter	Solid state	Standard	Modelled	 obs-calc 	$n\sigma^a$
	Average	Deviation	Average		
	(obs)		(calc)		
Bond Angles /degrees					
P5-C3-P5	114.5	0.7	115.0	0.5	0.71
O-P5-O	117.1	3.5	111.5	5.6	1.60
O-P5-OS	110.9	4.2	115.0	4.1	0.98
OS-P5-OS	103.3	1.0	104.8	1.5	1.50
O-P5-C3	110.2	64.1	112.1	1.9	0.03
OS-P5-C3	107.5	4.7	103.9	3.6	0.77
P5-OS-C3	124.3	2.1	119.4	4.9	2.33
P5-OS-CA	97.0	38.1	89.1	7.9	0.21
P5-C3-Cl	108.5	0.2	108.4	0.1	0.50
P5-C3-OH	104.6	1.7	104.6	0.0	0.00
P5-C3-C3	110.1	2.5	112.0	1.9	0.76

^a The difference between the mean observed and mean calculated parameter expressed as the number (n) of standard deviations (σ) of the experimental observations.

3. Simulated annealing of the bisphosphonates

Minimal differences were observed for the minimised structures obtained from only force field calculations and for the structures obtained from simulated annealing. The bond lengths obtained for the various structures (other than the P-O bonds) were approximately equivalent with a maximum relative standard deviation 0.1%. The slightly larger variation in bond length for the P-O bond was due to the ambiguity present in the protonation of the bond (i.e. single or double bond present). Similarly the error in the bond angles was low other than the oxygen-containing angles. These large errors are due to the change in intermolecular interactions due to the presence of the additional charged protons (Table A3 in the Appendix).

In summary, the global minimised structures compared well with the force field calculated structures with all the bonds and angles being reproduced well (Figure 11). The variations were

only present in the torsions but this is due to the free rotation present in the bonds. Therefore an assumption was made that the structures obtained from the force field calculations are actually the lowest energy structures.

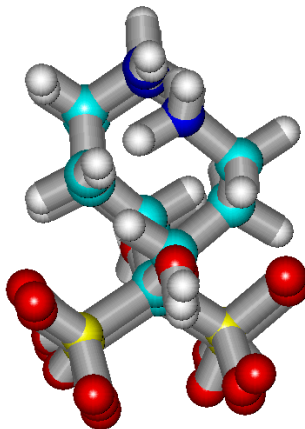


Figure 11: Overlay of alendronate (fully de-protonated) obtained from simulated annealing and from force field calculations

4. Modelling the interactions of the bisphosphonates with hydroxyapatite

4.1. Modelling of the hydroxyapatite surface

4.1.1. The (001) face of hydroxyapatite

The hydroxyapatite structure used has empirical formula $\text{Ca}_{10}(\text{PO}_4)_6(\text{OH})_2$. The (001) face contains surface Ca^{2+} ions in a trigonal arrangement with Ca^{2+} - Ca^{2+} distances of either 9.4 or 10.0 Å. Immediately below this surface layer are octahedral sites defined by six Ca^{2+} ions, with OH^- ions occupying opposite faces of the octahedron. A phosphate is located approximately along the perpendicular bisector of each Ca^{2+} - Ca^{2+} vector, 3.08 and 3.28 Å, respectively, from the two Ca^{2+} ions. The base of each surface trigonal cavity is lined either by Ca^{2+} ions and an OH^- ion of an octahedral site, or by phosphate ions (Figure 12).

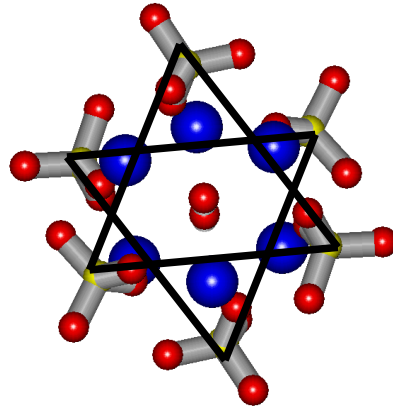


Figure 12: Representation of surface cavity and octahedral cavity present on (001) surface of hydroxyapatite

4.1.2. The (010) face of hydroxyapatite

The basic building block of the (010) surface consists of one phosphate group, one calcium ion and two hydroxyl groups. This building block is translated along the c-axis, forming a row of alternating phosphate and calcium ions, which is parallel to a row of hydroxyl groups. These rows are then translated along the a-axis to form the surface (Figure 13).

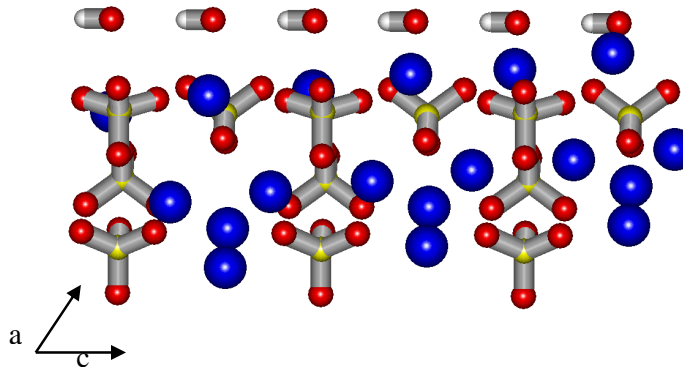


Figure 13: Representation of the (010) surface of hydroxyapatite showing translation along the c axis

4.1.3. The (100) face of hydroxyapatite

The (100) face contains the same building block as the (010) face. This is translated along the b-axis to form a row of alternating phosphate and calcium ions parallel to a row of hydroxyl groups; these rows are in turn translated along the a-axis to form the plane (Figure 14).

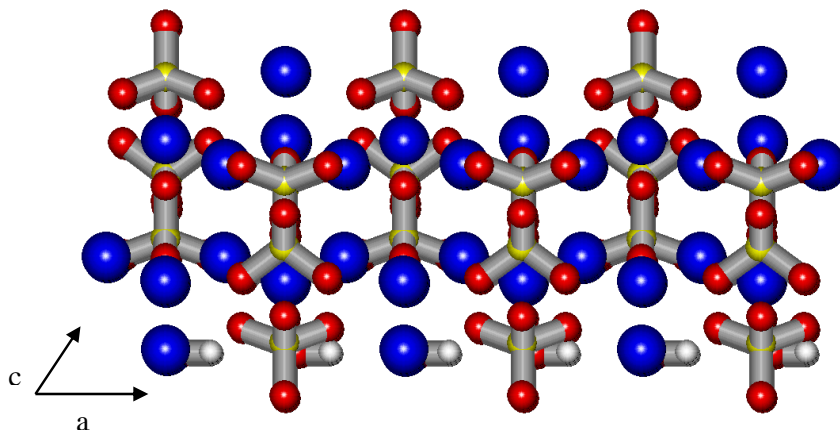


Figure 14: Representation of the (100) face of hydroxyapatite showing translation along the a axis

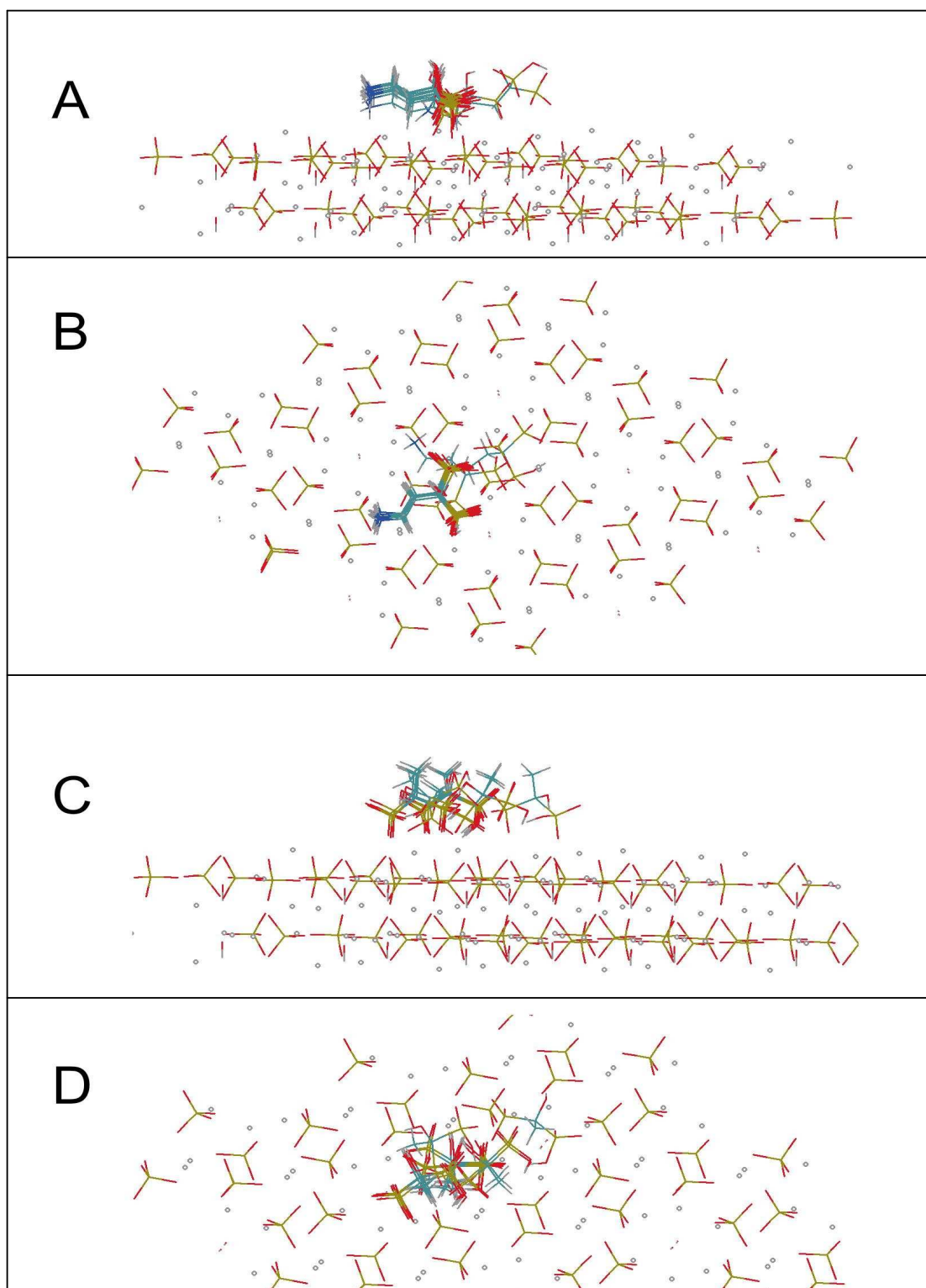
4.2. Testing the effect of the relative permittivity

The problem with using molecular modelling to investigate the interactions of BPs with bone is that molecular modelling calculations are performed in a vacuum. As this does not mimic the “real world” environment it was necessary to compensate for this variation. The only way to mimic this environment was to include a relative permittivity into our calculations to dampen the electrostatic interactions. The use of $78\epsilon_0$ [32,34] has been recommended for the relative permittivity for an aqueous environment and as blood serum is made up of seventy percent water this constant seemed the most applicable. The applicability of this constant was investigated by varying ϵ between $10\epsilon_0$ and $75\epsilon_0$ when modelling the interaction of APD and HEDP with hydroxyapatite (Table 11). The results showed that as soon as any dampening effect was added to the relative permittivity, the minimised overall energy of the system dropped 10 fold in magnitude (Figure 16). In addition the total and electrostatic energies obtained for any relative permittivity larger than $10\epsilon_0$ are statistically equivalent (by $< 1 \text{ kcal mol}^{-1}$) but more importantly the structures obtained are the same for all relative permittivities (Figure 15). As all the dampening effect for all constants larger than $10\epsilon_0$ were equivalent the relative permittivity of water was used.

Table 10: Change in strain energy, ΔE_s , for the interactions of APD and HEDP with the (001) surface of hydroxyapatite as a function of the relative permittivity

Ligand	ϵ / ϵ_0	Components of the strain energy					ΔE_s /kcal mol ⁻¹
		Bond stretching	Angle bending	Torsion	Non-bonded	Electrostatics	
APD	10	-0.02	0.07	0.05	-16.25	-13.70	-29.85
	15	0.42	1.14	0.46	-18.79	-3.06	-19.82
	20	0.05	0.25	0.00	-17.53	1.24	-15.99
	25	0.04	0.16	0.00	-17.56	1.10	-16.26
	30	0.14	0.10	0.01	-17.57	0.97	-16.45
	35	0.04	0.07	0.01	-17.58	0.87	-16.59
	40	0.04	0.06	0.01	-17.59	0.78	-16.70
	50	0.03	0.04	0.02	-17.60	0.64	-16.86
	55	0.04	0.04	0.02	-17.60	0.69	-16.82
	60	0.03	0.02	0.02	-17.61	0.56	-16.97
	65	0.03	0.04	0.02	-17.62	0.51	-17.01
	70	0.03	0.03	0.03	-17.62	0.49	-17.05
75	0.03	0.01	0.03	-17.61	0.46	-17.08	
HEDP	10	0.01	0.43	0.02	-15.67	-10.93	-26.14
	15	0.00	-0.15	0.15	-12.81	-1.70	-14.51
	20	0.00	-0.12	0.14	-13.02	-1.11	-14.11
	25	0.03	0.17	0.01	-14.70	-0.15	-14.64
	30	0.03	0.01	0.17	-13.23	0.21	-12.82
	35	0.03	0.01	0.17	-13.25	0.19	-12.85
	40	0.03	0.02	0.16	-13.27	0.18	-12.88
	50	0.02	0.13	-0.01	-14.96	0.14	-14.68
	55	-0.03	-0.02	0.44	-13.64	-0.03	-12.88
	60	0.02	0.15	-0.02	-15.96	0.71	-15.09

Ligand	ϵ / ϵ_0	Components of the strain energy					ΔE_s /kcal mol ⁻¹
		Bond stretching	Angle bending	Torsion	Non-bonded	Electrostatics	
65	0.02	0.02	0.15	-0.02	-15.96	0.66	-15.15
70	0.02	0.02	0.15	-0.02	-15.96	0.62	-15.19
75	0.02	0.02	0.15	-0.02	-15.97	0.58	-15.24



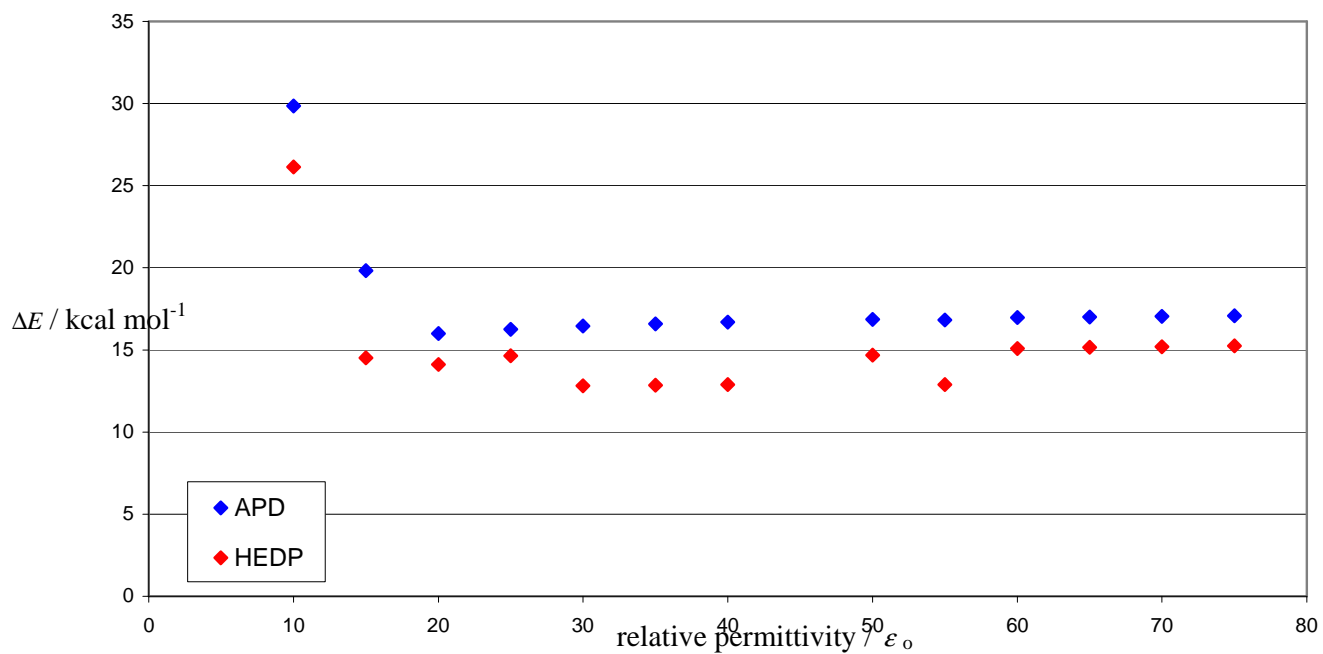


Figure 16: Graphical representation showing the dependence of the total energy of the minimised structure on the relative permittivity

4.3. Interactions of the bisphosphonates with the hydroxyapatite surface

4.3.1. Interactions of the mono-protonated bisphosphonates with the hydroxyapatite surface

The energy of interaction between the bisphosphonate ligands studied and hydroxyapatite is dominated by non-bonded interactions (Table 12, note all energies are the mean of 20 independent minimisations).

4.3.1.1. Interactions with the (001) face of hydroxyapatite

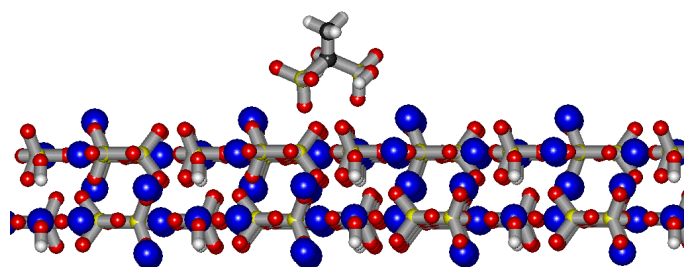
All five bisphosphonate ligands that were studied interacted in a similar fashion with the (001) face. The two phosphonate groups pointed downwards towards the surface (Figure 17A), usually close to one of the surface Ca^{2+} ions (Table 13), and with the bulk of the ligand positioned in a surface trigonal cavity that is lined with phosphate groups (Figure 17B). In addition, in HEDP the OH substituent on the α carbon, and the protonated OH group of the phosphonate form hydrogen bonds with the phosphate groups lining the surface trigonal cavity (Figure 17C). For APD and alendronate the $\text{C}\alpha$ hydroxyl forms an internal hydrogen bond with one of the oxygen atoms of a phosphonate group.

The magnitude of the interaction energy increases with the molecular volume of the ligand, reaching a maximum with alendronate, and then decreasing significantly for neridronate (Table 12 and Figure 18). The side chains of APD and alendronate align with the (001) surface, which increases the non-bonded interactions (Figure 17D). In neridronate, however, the side-chain folds on itself and does not interact significantly with the surface of the mineral thus reducing the non-bonded interactions (Figure 17E).

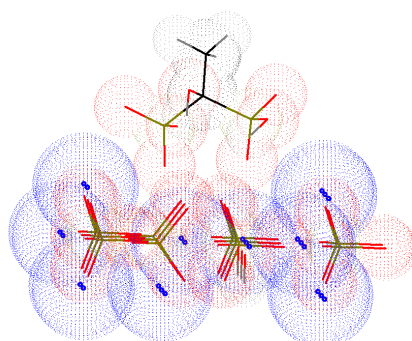
Table 12: Interaction of bisphosphonates with hydroxyapatite: distances between oxygen atoms of phosphonates and the nearest calcium ions on the 001 face of hydroxyapatite

ligand	$\text{O}\cdots\text{Ca}^{2+}$ distances /Å ^a			
	First Ca^{2+} ion		Second Ca^{2+} ion	
	First Phosphonate	Second Phosphonate	Second Phosphonate	Second Phosphonate
MDP	3.09 ± 0.06	3.24 ± 0.10	3.11 ± 0.12	
HEDP	3.71 ± 0.02	2.950 ± 0.003	3.11 ± 0.10	4.34 ± 0.02
APD	3.47 ± 0.01			(5.1 ± 0.2)
Neridronate	3.23 ± 0.01	3.43 ± 0.02	4.45 ± 0.10	4.12 ± 0.10
Alendronate	3.03 ± 0.05		3.04 ± 0.09	

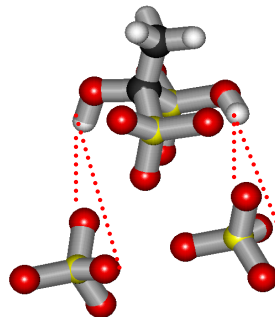
A



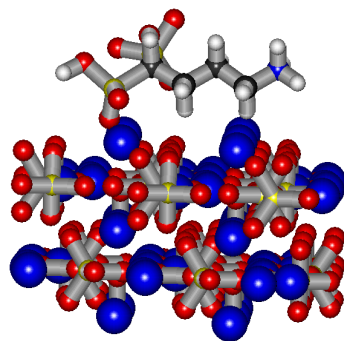
B



C



D



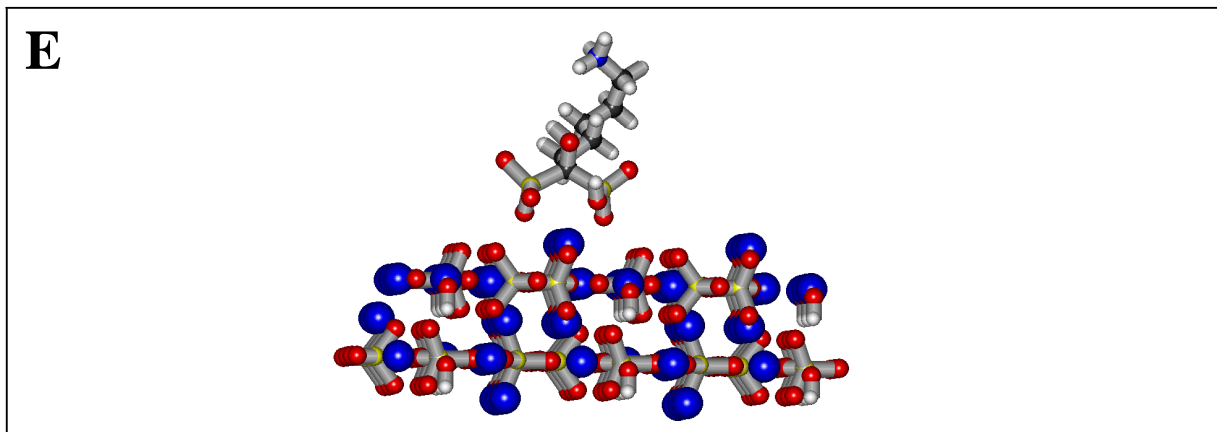


Figure 17: Representations of the interaction of the bisphosphonates with the (001) face of hydroxyapatite (Represented by: A-C HEDP and D-E alendronate)

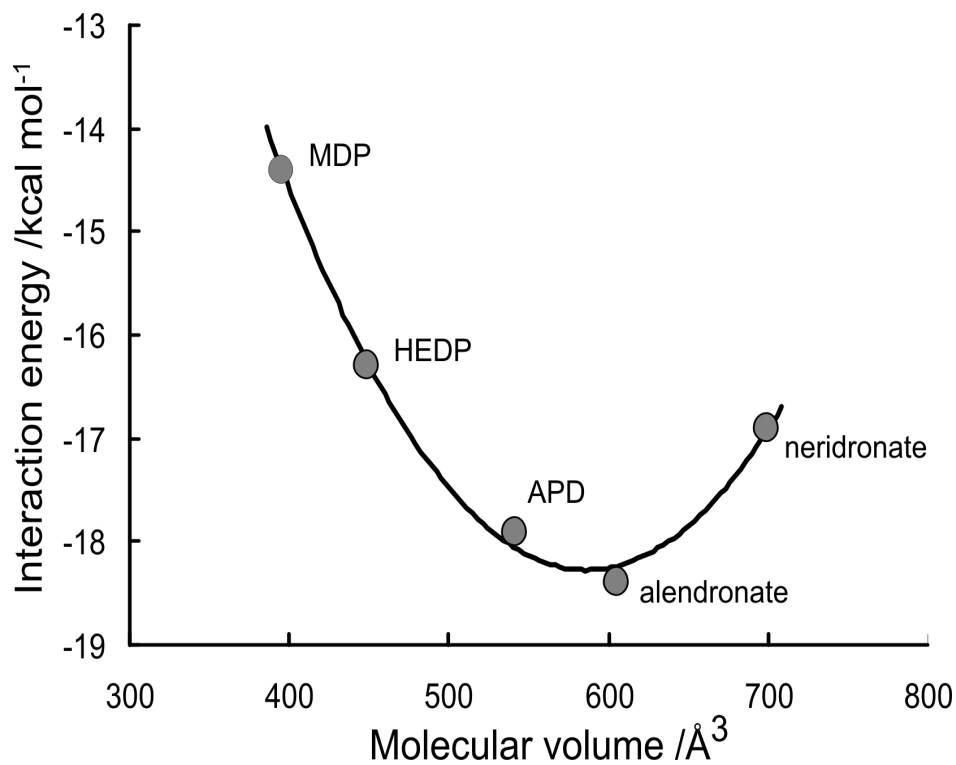
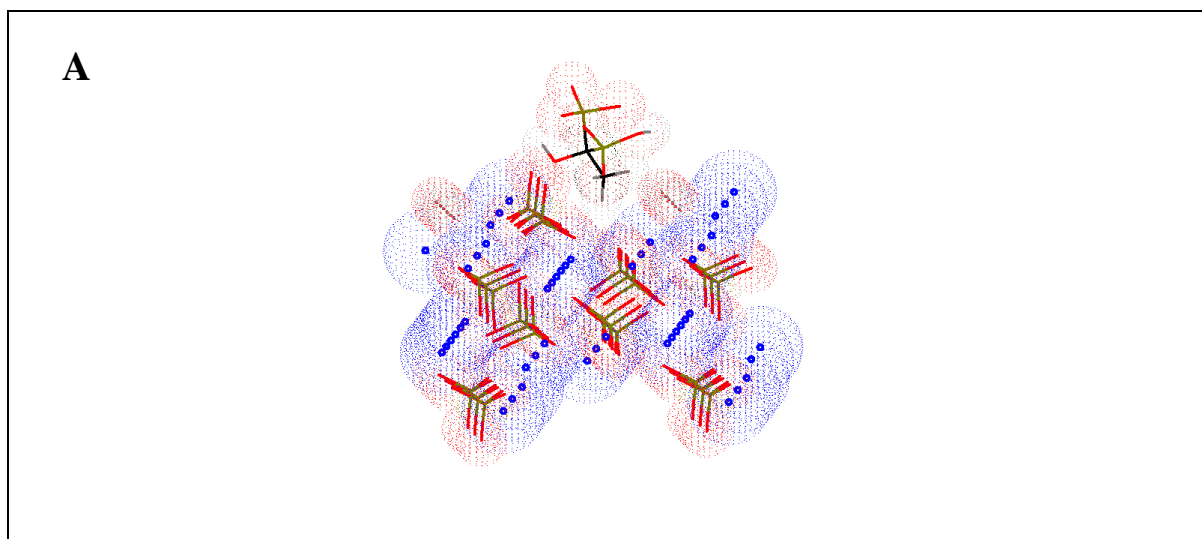


Figure 18: Dependence of the interaction energy of five bisphosphonate ligands and the (001) face of hydroxyapatite on the molecular volume of the ligand

4.3.1.2. Interactions with the (010) face of hydroxyapatite

There were two principal conformations adopted by bisphosphonates on the (010) surface. In both the molecules dock in the cavity that runs alongside the rows of hydroxyl and phosphate groups that define the surface (Figure 19A). In the first conformation (termed conform A in Table 12), found for MDP and about 40% of the structures of alendronate on the (010) face, both phosphonate groups interact with the surface (Figure 19B). One of the phosphonate groups inserts well into the surface such that one of its oxygen atom interacts with three calcium ions in the plane below the surface plane. The second phosphonate group is within van der Waals interaction of two Ca^{2+} from the neighbouring row. In the second conformation (conform B in Table 12), adopted by the majority of ligands, only one of the phosphonate groups interacts with the surface (Figure 19C). All of its oxygen atoms are in van der Waals contact with three surface Ca^{2+} ions and two surface phosphate groups. The $\text{C}\alpha$ side chain is in contact with the surface, while the second phosphonate group points towards the solution.

Since in conform A the $\text{C}\alpha$ side chain has little interaction with hydroxyapatite, the interaction energy is virtually independent of the structure of the bisphosphonate ($-17.5 \pm 1.0 \text{ kcal mol}^{-1}$ for MDP, and $-17.0 \pm 1.0 \text{ kcal mol}^{-1}$ for alendronate). In conform B, the interaction energy increases with the size of the side chain (HEDP -15.9 ± 0.2 ; APD -18.0 ± 1.4 ; and alendronate $-19.2 \pm 0.7 \text{ kcal mol}^{-1}$) but decreases for neridronate ($-17.8 \pm 2.5 \text{ kcal mol}^{-1}$), as was seen on the (001) face. The reason for this is the formation of a hydrogen bond between the amino group and the phosphonate group that is pointed away from the mineral surface, which prevents a complete interaction of the $\text{C}\alpha$ side chain with hydroxyapatite.



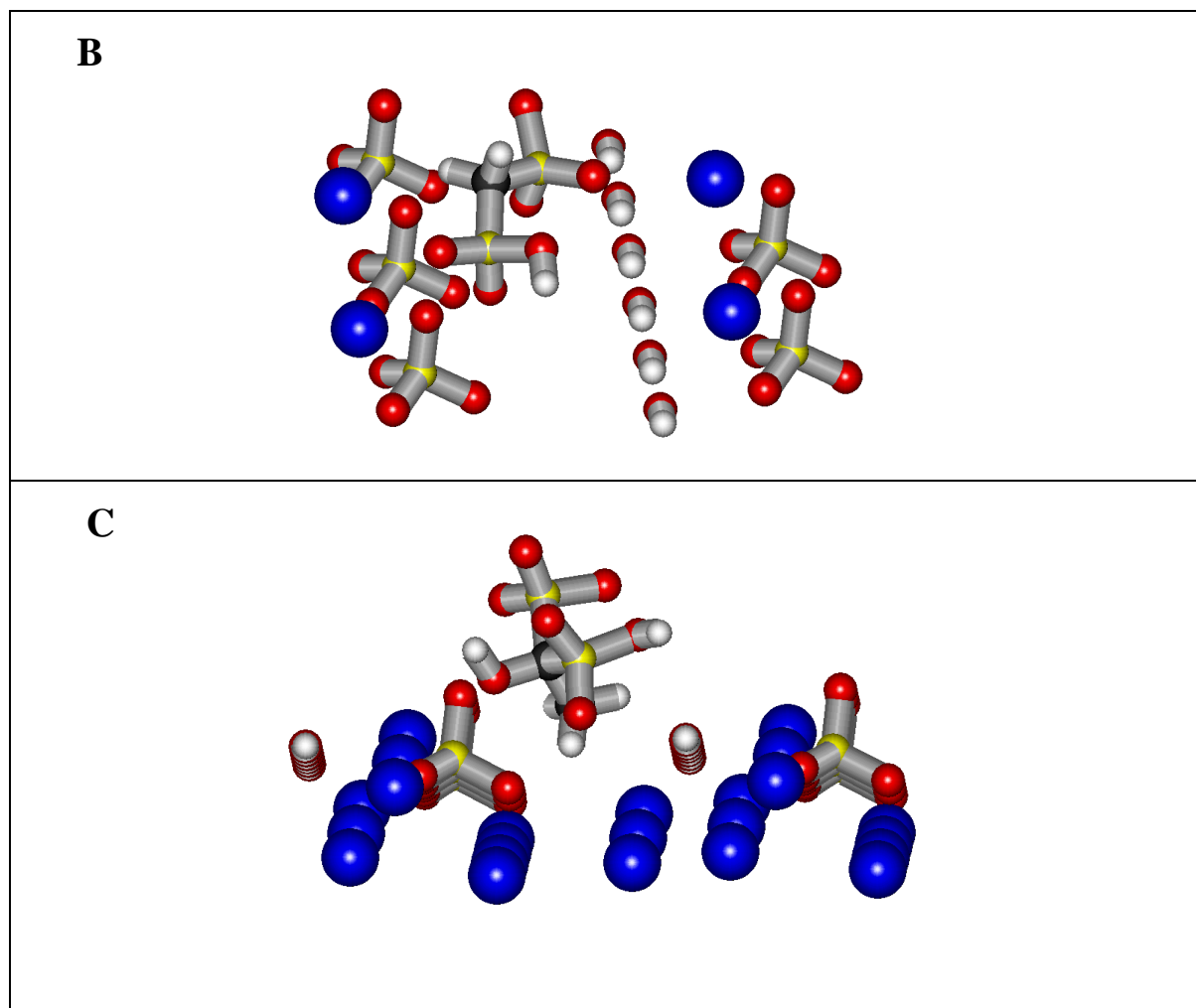


Figure 19: Representations of the interactions of the two conformations A and B adopted by the bisphosphonates when interacting with the (010) surface of hydroxyapatite (represented by HEDP)

4.3.1.3. Interactions with (100) face of hydroxyapatite

As for the interactions with the (010) face of hydroxyapatite, two conformations were seen for the interactions on the (100) face (Figures 20A and B). As the structures of the (010) and (100) crystal were similar in nature, with both containing rows of phosphate groups aligned with hydroxyl and calcium rows, the interactions seen on the two faces are similar. Similarly to the interactions with the (010), the bisphosphonate aligned within the cavity between these rows. The only difference between the two faces is that the cavity in which the bisphosphonate aligns is along the b axis rather than along axis c (Figure 20A).

In the first conformation (termed conform A in Table 12), only one of the phosphonate groups pointed towards the surface and the C α side chain interacted with the surface while in the second conformation (conform B), the C α side chain interacted strongly with the surface and both phosphonate groups pointed away from the surface towards the solution. The former conformation, which is the more common, is also energetically more favourable (Table 12). The magnitude of the interaction is virtually insensitive to the nature of the side chain ($\Delta E_s = -16.3 \pm 0.7 \text{ kcal mol}^{-1}$) and is over 6 kcal mol^{-1} more important than the average interaction energy for the second conformation ($10 \pm 2 \text{ kcal mol}^{-1}$).

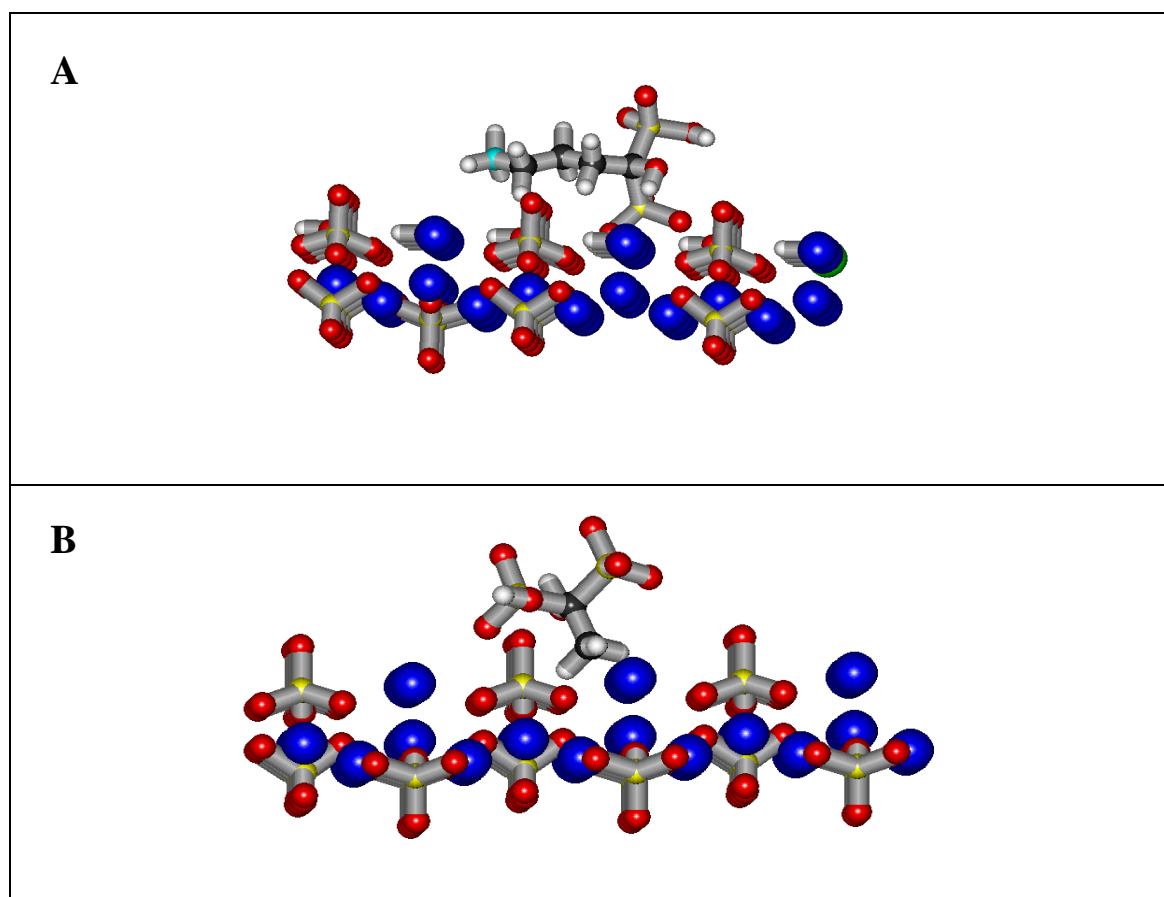


Figure 20: Representations of the interactions of the two conformations A (represented by alendronate) and B (represented by HEDP) adopted by the bisphosphonates when interacting with the (100) surface of hydroxyapatite

4.3.2. Interactions of the di-protonated bisphosphonates with the hydroxyapatite surface

From the available acid dissociation constants (Appendix Table A3) it is clear that nitrogen-containing bisphosphonates exist both as mono- and di-protonated species at pH = 7.6 (Figure 21) with the dominant species being the deprotonated ligand. Thus it was necessary to examine whether addition of another proton to APD, alendronate and neridronate had any significant effect on the structure of their interaction with hydroxyapatite.

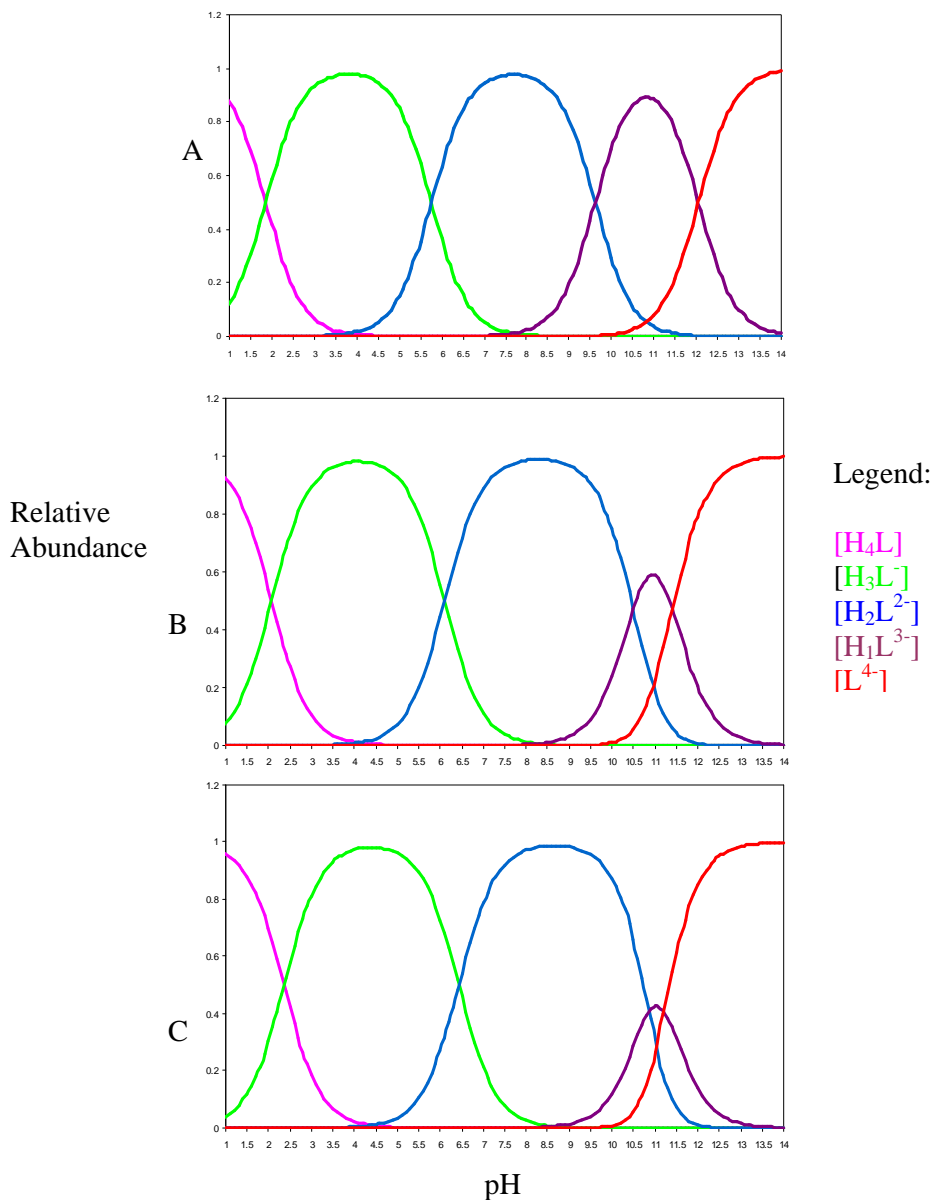


Figure 21: Species distribution for APD (A), alendronate (B) and neridronate (C).

4.3.2.1. Interactions with the (001) face of hydroxyapatite

The interactions on the (001) surface are very similar to those found for mono-protonated APD and alendronate but very different for neridronate (Figure 22). For all three ligands, the ligand was located in the surface trigonal cavity with both phosphonates and the side chain interacting with the surface, thus the magnitude of the stabilization energy increased as the chain size increased with neridronate having the highest (Table 14, Figure 24).

A calcium ion is in close contact with one oxygen atom from each of the phosphonate groups, whilst at least one hydrogen atom from a protonated phosphonate is hydrogen-bonded to a phosphate ion on the hydroxyapatite surface. A hydrogen bond is also present between the proton of the C α hydroxyl group and an oxygen atom from one phosphonate group (Figure 23).

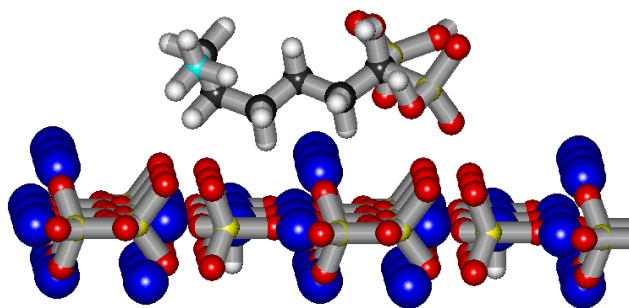


Figure 22: Representation of the interaction between the (001) surface of hydroxyapatite and neridronate, $[H_2L^{2-}]$.

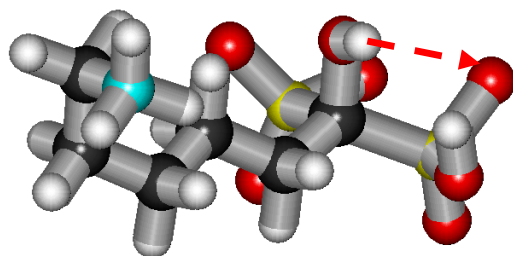


Figure 23: Representation of the hydrogen bond present in the di-protonated bisphosphonates when interacting with the (001) surface (represented by neridronate).

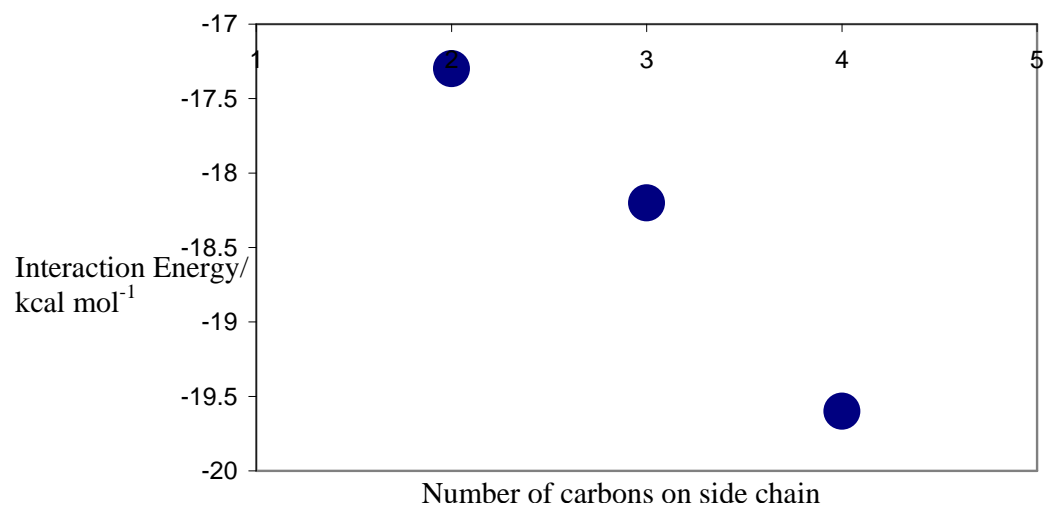


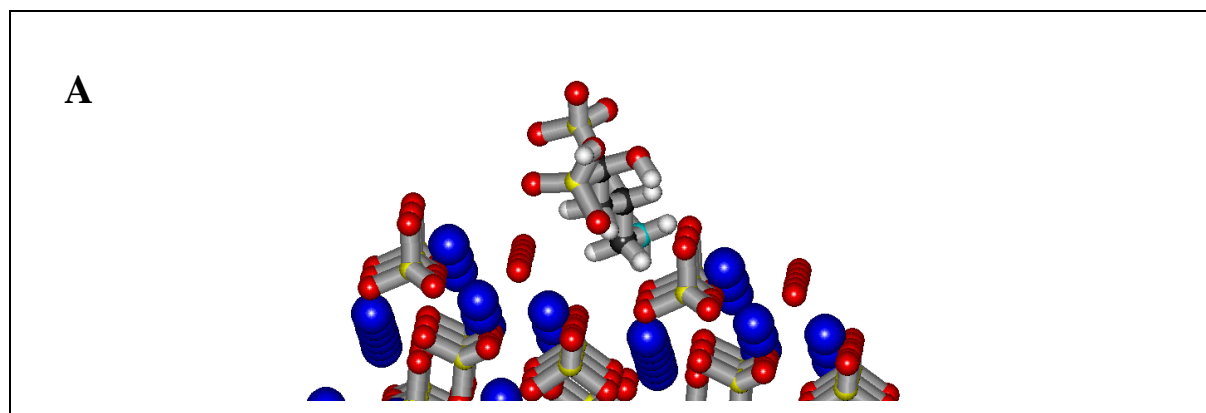
Figure 24: Graphical representation showing that as the length of the $C\alpha$ chain increases so the interaction energy increases

4.3.2.2. Interactions with the (010) face of hydroxyapatite

Two conformations are seen for the interactions with the (010) surface. In conformation A (seen for alendronate and neridronate only) both phosphonate groups point downwards onto the surface, while in conformation B (seen for all three ligands) only one phosphonate interacts with the surface. In both, the $C\alpha$ hydroxyl group points away from the surface while the amine chain interacts with the surface hydroxide ions.

In conformation A, the ligand is aligned within the cavity formed by the chain of hydroxyl groups and the chain of phosphate ions. A calcium ion is in contact with an oxygen atom from each of the phosphonate groups. There are further interactions between the phosphonate groups and the calcium ions in the layer beneath the surface layer.

In conformation B the ligand lies above the chains of hydroxide and calcium ions while the interacting phosphonate lies within the surface cavity. All its oxygen atoms are in close contact with three calcium ions on the surface. Conformation A is energetically more favourable than conformation B (Table 14). For conformation A (Figure 25A) the magnitude of the interaction increases with the size of the side-chain but the converse is true for conformation B (Figure 25B) because, as the chain length increases, the chain becomes too long to preserve an interaction between the amino group and the surface hydroxide ions.



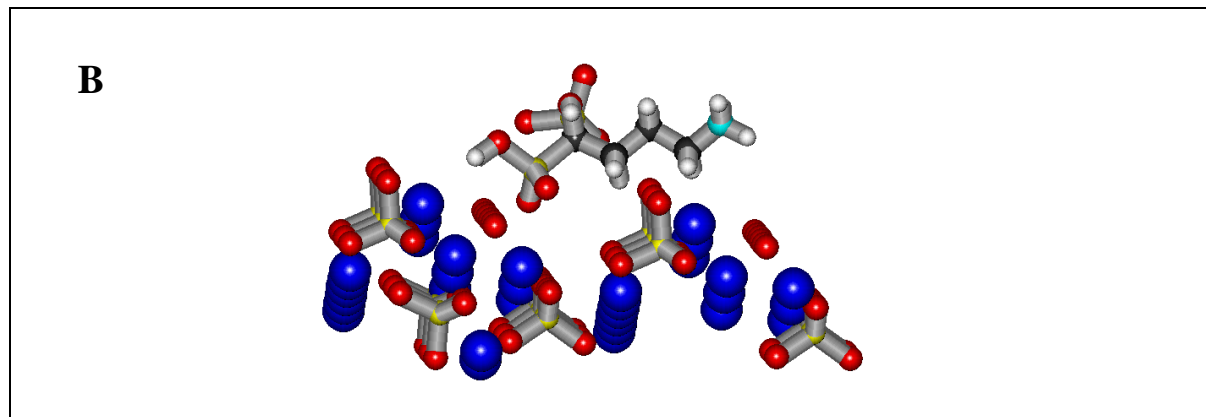
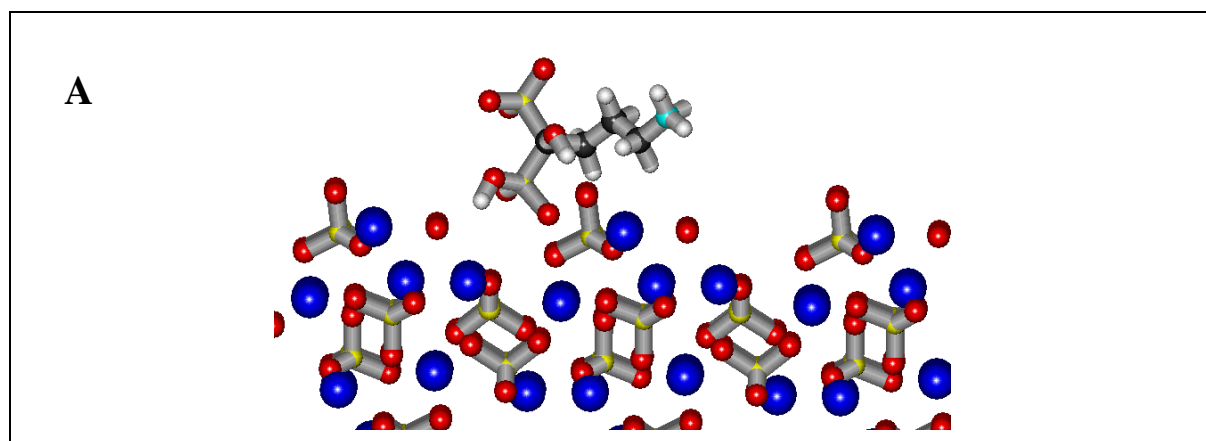


Figure 25: The interaction of the two conformations A and B of alendronate with the (010) surface of hydroxyapatite

4.3.2.3. Interactions with the (100) face of hydroxyapatite

One principal conformation occurs on the (100) surface, although APD does adopt a second conformation (Table 14, Figure 26). In the principal conformation, the ligand aligns in the cavity that runs along the a-axis and only one of the phosphonate groups points towards the surface. An oxygen atom from this phosphonate interacts with a Ca^{2+} ion. The $\text{C}\alpha$ side chain aligns parallel to the surface along the a-axis thus the interaction energy increases monotonically with the length of the side-chain (Table 14).

For conformation B of APD both phosphonate groups interact with the surface but the $\text{C}\alpha$ chain points away from the surface. Since both the phosphonate groups interact with the surface the stabilization energy is greater than for conformation A.



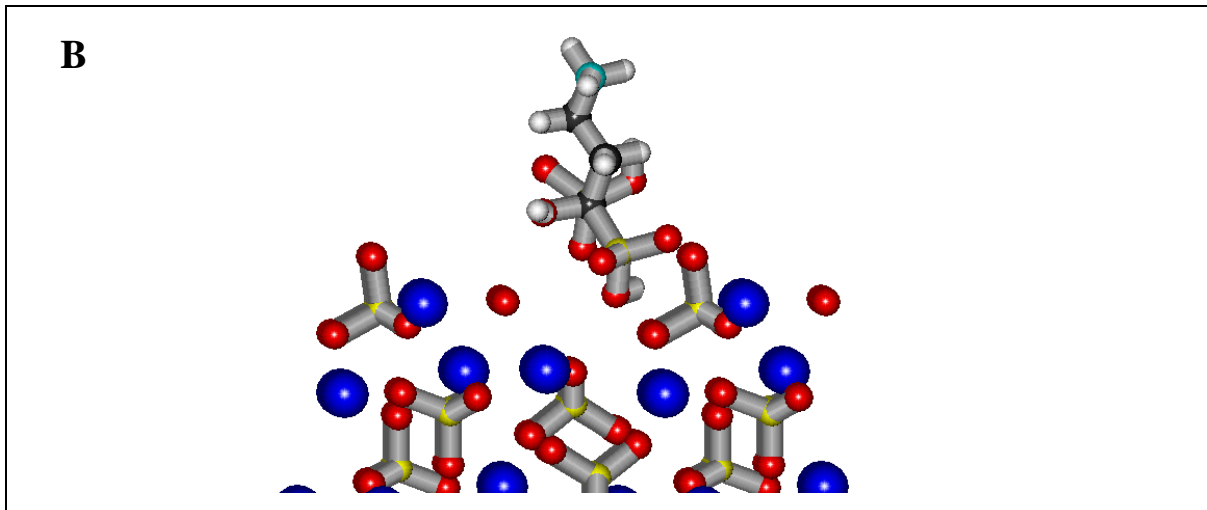


Figure 26: Representation of the interaction of conformation A (represented by alendronate) and B (represented by APD) of the bisphosphonate with the (100) surface of hydroxyapatite.

Chapter 4: Conclusion

It has been shown that our augmentation to the generalised AMBER force field, GAFF, and which we have called WitsGAFF Force Field models interaction well in both a vacuum environment and a synthetic aqueous environment (by using a relative permittivity of $78\epsilon_0$), with experimental and modelled bond lengths and angles within the required specifications [50]. The minimised structures usually adopt the gauche or anti conformation. By using simulated annealing it was determined that these local minimum structures are equivalent to the global minimum structure.

The principal aim of this project was to start determining a mechanism as to how the bisphosphonates treat bone cancer. Molecular modelling has shown the affinity of the crystalline bone apatite (hydroxyapatite) is different when different substituents are present on the central carbon. In addition the affinity and the nature of the interactions are different on different faces of hydroxyapatite with the interactions on the (001) face being the least complex of the interactions. The interactions on all the faces were dominated by electrostatic interactions between the phosphonate groups and amine group on the bisphosphonate with the phosphate and calcium ions in the hydroxyapatite. As we only looked at the interactions with a synthetic bone equivalent there is still much work to be done to determine the exact mechanism, as natural occurring bone is a great deal more complex.

Chapter 5: Future Work

As the field of bone cancer research is extremely large it is impossible to suggest all the possible research opportunities with the bisphosphonates. In my opinion the next important step is to try to synthesize additional bisphosphonates with varying substituents on the central carbon to determine if our force field parameter files WitsGAFF model them correctly.

More research is needed into the interactions of the bisphosphonates on other faces of hydroxyapatite and on bone.

Once our force field has been tested it is necessary to try to add other elements to Wits-GAFF. Initially we should try to add small metal anions as our body contains so many metal ions that it will be important to see how in the presence of a metal the ligand will bind and how this will affect the affinity of the bisphosphonate to hydroxyapatite. The next step will be the inclusion of the radionuclides into the force field.

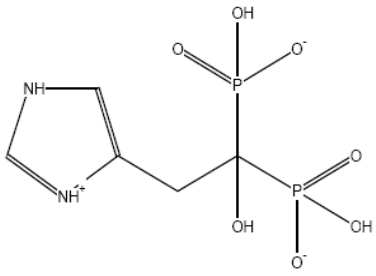
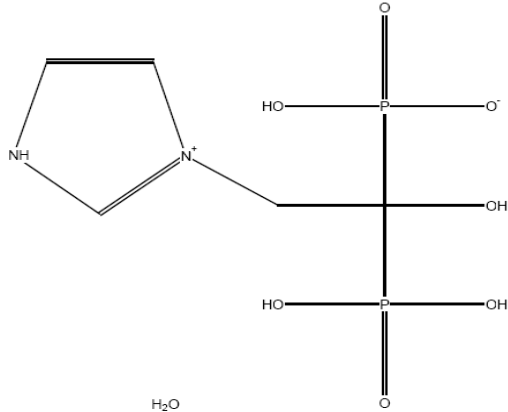
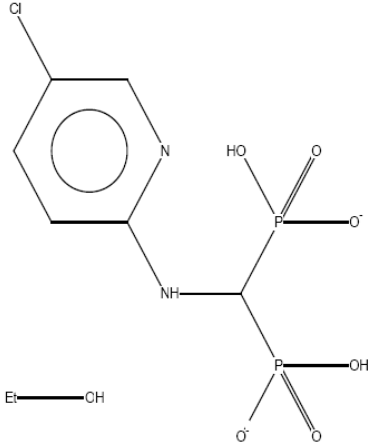
In addition it is necessary that this research be complemented with results from other scientific techniques such as potentiometry, protein NMR and in vivo studies.

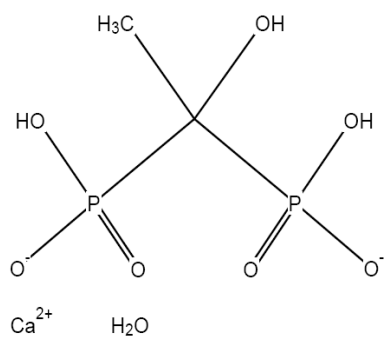
Chapter 6: Appendix

Table of Contents	Page
Section 1: Supplementary tables in the Appendix	69
Table A1: The structures of known bisphosphonates obtained from the CSD, and their CSD reference codes	69
Table A2: The structures and ref codes of structures obtained from the CSD excluded from the modelling	84
Table A3: Comparison of bond lengths and bond angles obtained using the structures obtained from simulated annealing	85
Section 2: Supplementary figures in the Appendix	86
Figure A1: Distribution of torsional angles for the torsion O-P-C-P	86
Figure A2: Distribution of torsional angles for the torsion HO-P-C-P	86
Figure A3: Distribution of torsional angles for the torsion O-P-C-X (where X is any substituent)	86
Figure A4: Distribution of torsional angles for the torsion OH-P-C-X (where X is any substituent)	87
Figure A5: Charge distribution for atom type P5	87
Figure A6: Charge distribution for atom type C3	87
Figure A7: Charge distribution for atom type O	88
Figure A8: Charge distribution for atom type OH	88
Figure A9: Charge distribution for atom type HO	88
Section 3: Supplementary documents in the Appendix	89
A1: Search criteria use to obtain the crystallographic data for the bisphosphonates	89
A2: An example of an .ent file	90
A3: An example of a .hin file	93
A4: An example of an entry in a logfile	95
A5: An example of the optimisation macro used to perform the minimisation	96
A6: An example of the statistics macro used to collect the statistics data	97
Section 4: List of supplementary data on CD	99

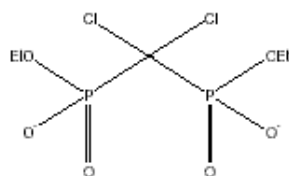
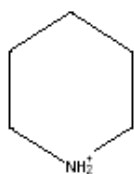
Section 1: Supplementary tables in the Appendix

Table A1: The structures of known bisphosphonates obtained from the CSD, and their CSD reference codes

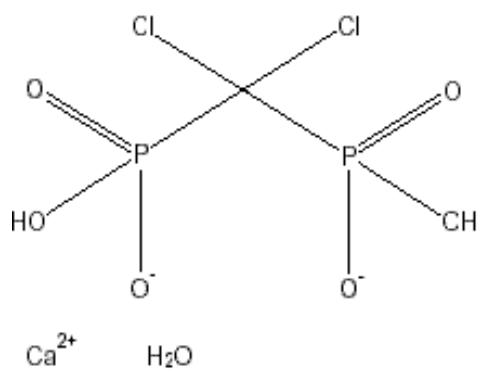
CSD Structure	Ref Code
<p>Na⁺</p>  <p>AHIJUW [65]</p>	
 <p>H₂O</p> <p>BEKBOJ [66]</p>	
<p>Na⁺</p>  <p>Et—CH</p> <p>H₂O</p> <p>BEKBUP [66]</p>	

CSD Structure**Ref Code**

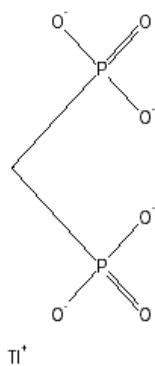
CAEADP [67]



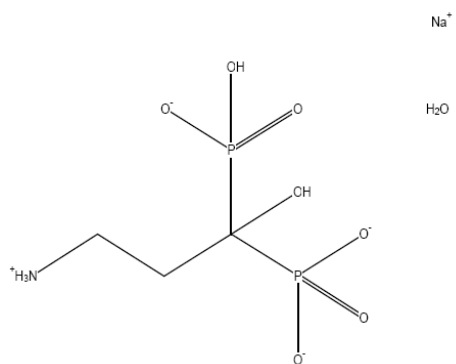
CAKKEF [68]



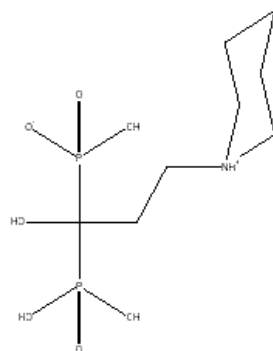
CAVKUF [69]



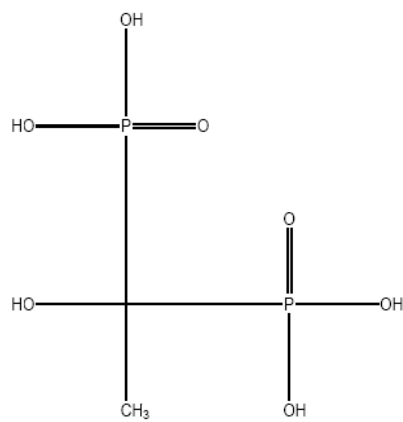
DEZGAQ [70]

CSD Structure**Ref Code**

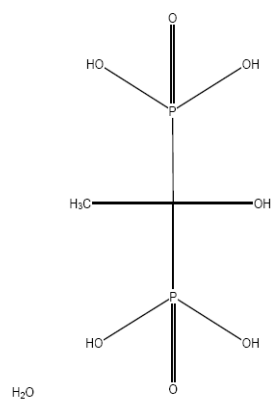
EFAMIH [71]



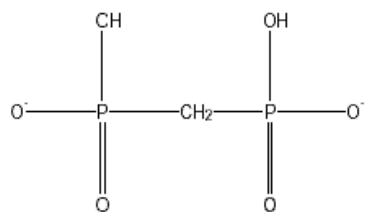
EMIGIQ [72]



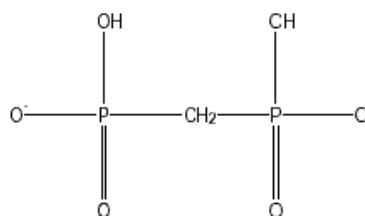
ETHDPH [73]



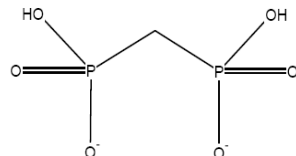
ETHDPH01 [74]

CSD Structure**Ref Code**

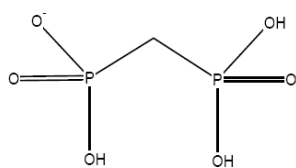
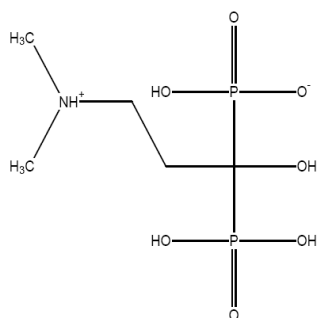
FEZLUR [75]

NH₄⁺

FEZMAY [75]

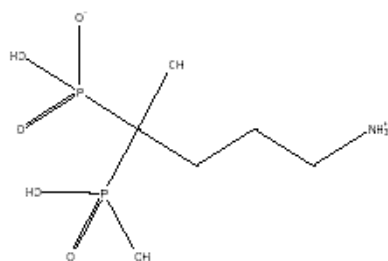
Ti⁺

FIRCAK [75]

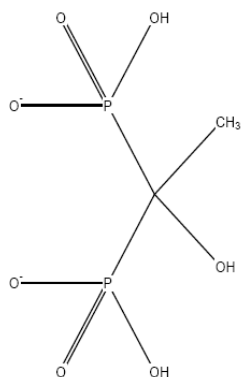
Ti⁺

FURCAW [76]

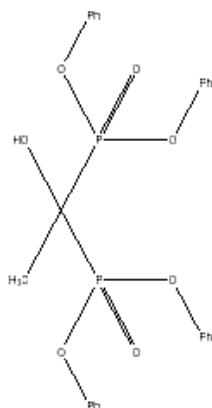
H₂O



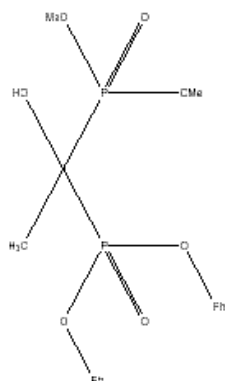
GOWZEX [77]



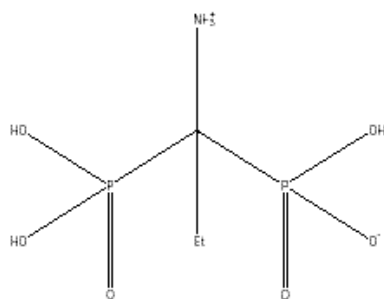
HOWCAX [78]



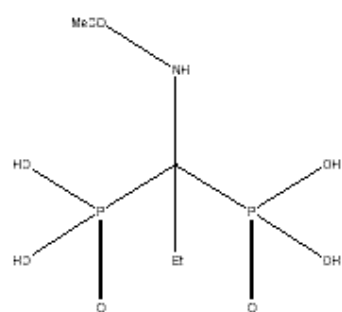
IGUMAY [79]



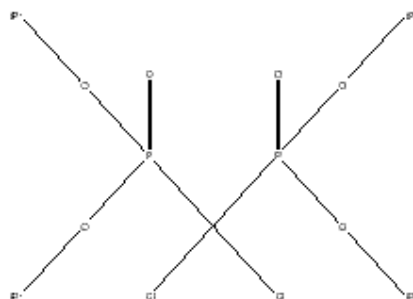
IGUMEC [79]



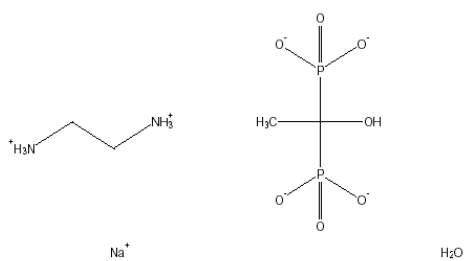
JAGXUL [72]



JAGYAS [72]

H₂O

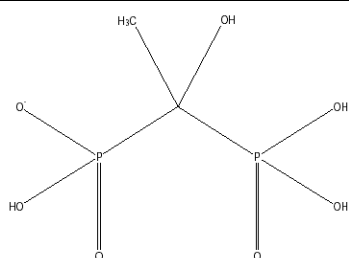
JOTVET [80]



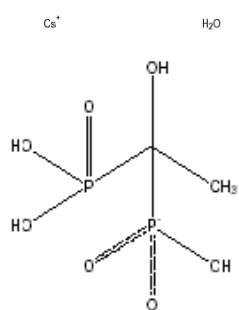
KAGREQ [81]

CSD Structure

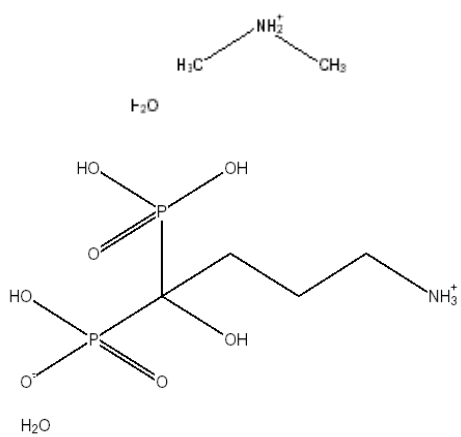
Ref Code



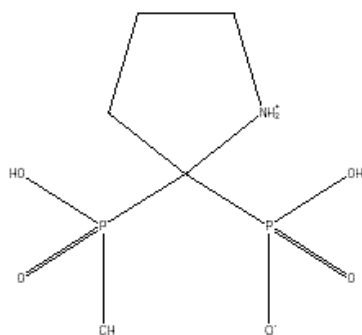
KIBLOW [82]



KOGSAA [83]



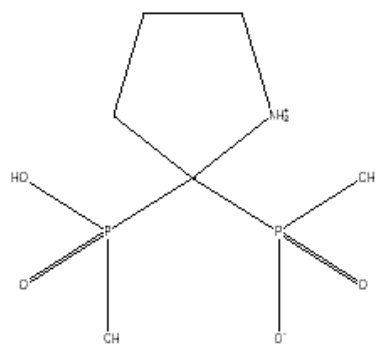
KOJGUL [84]



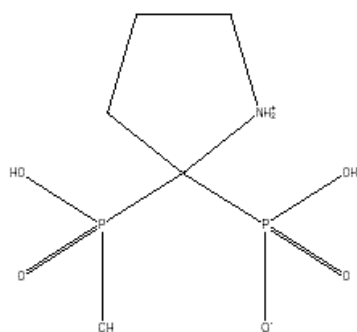
LIYTOC [85]

CSD Structure

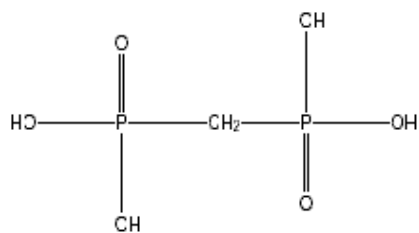
Ref Code



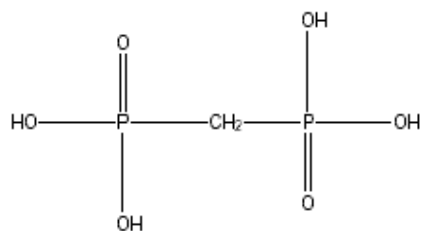
LIYTOC01 [85]



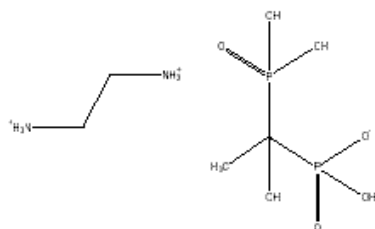
LIYTOC02 [85]



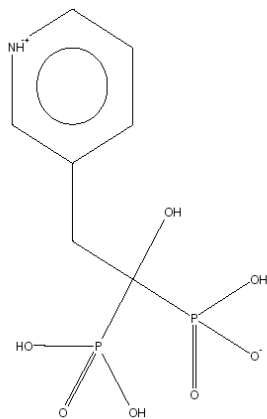
MEYDPA [86]



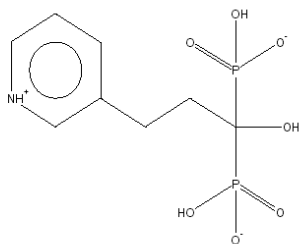
MEYDPA11 [87]



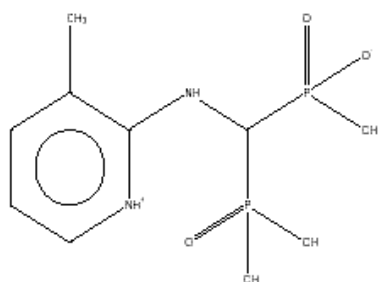
MODGUH [74]



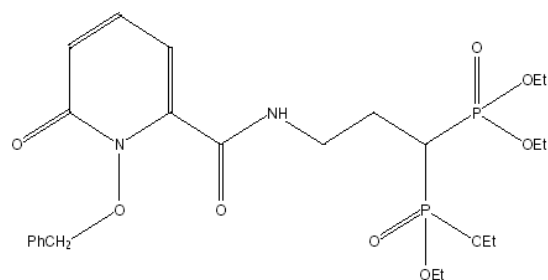
MOFVOS [88]

Na⁺H₂O

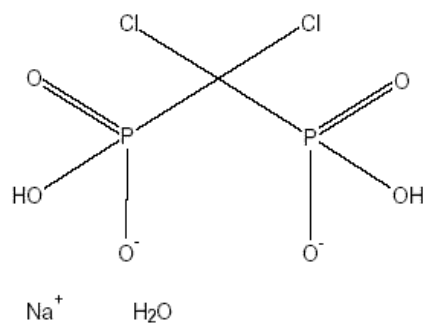
MUPTIA [89]

H₂O

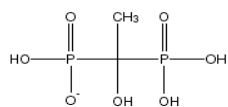
MUQDIL [90]



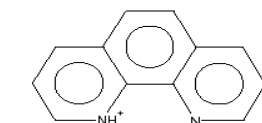
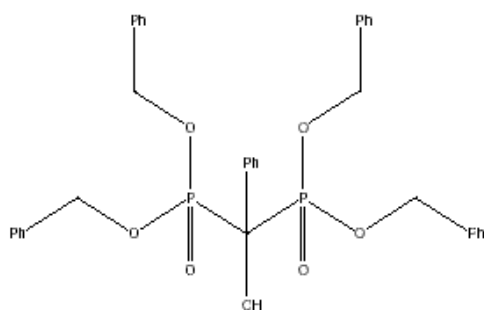
MUSLUH [91]



NAMDPC01 [69]

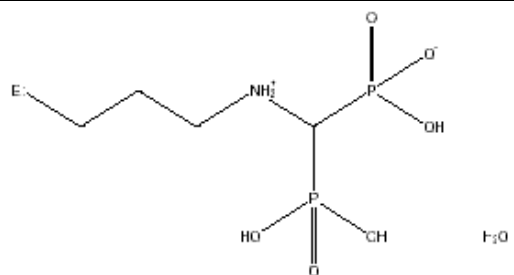


NODSEL [92]

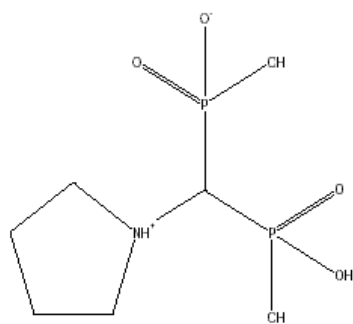
H₂O

PAWTUC [93]

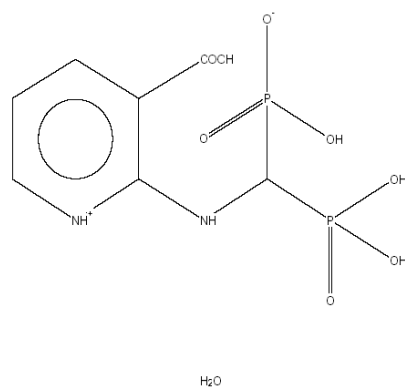
CSD Structure**Ref Code**



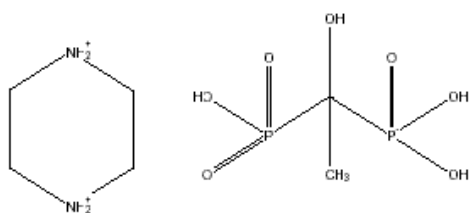
QURXOQ [94]



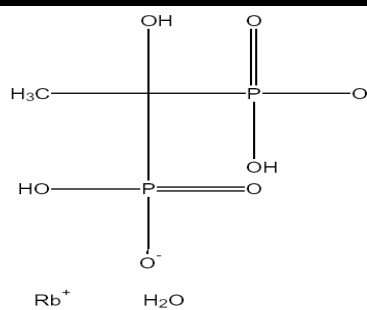
QURXUW [94]



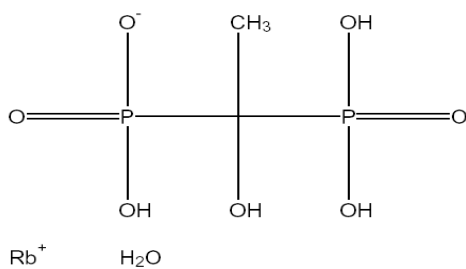
QURYAD [94]



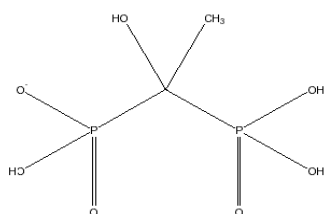
RIMGUP [95]

CSD Structure**Ref Code**

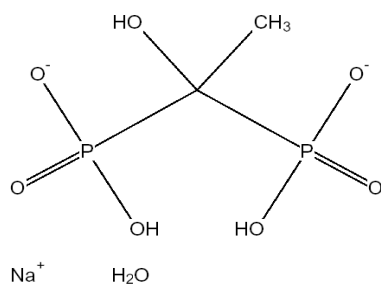
SATHIE [96]



SATHIE01 [97]

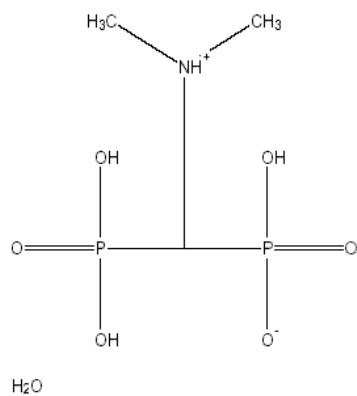


SATHIE02 [98]

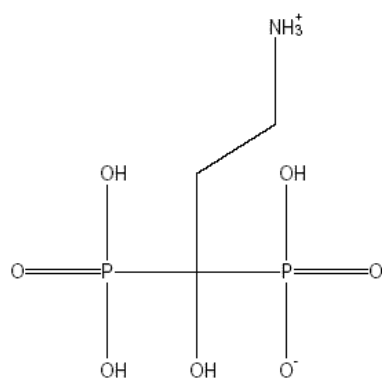
Rb⁺ H₂O

SHEDPH [16]

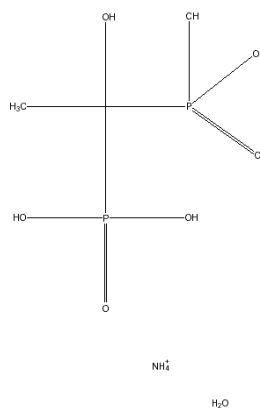
Na⁺ H₂O



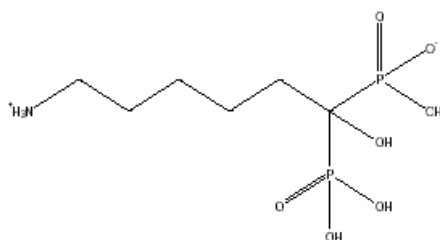
SOP SAR [99]



SOPSEV [99]



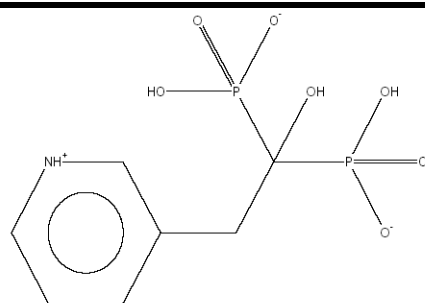
VEYJAK [98]



VUYTUE [100]

CSD Structure

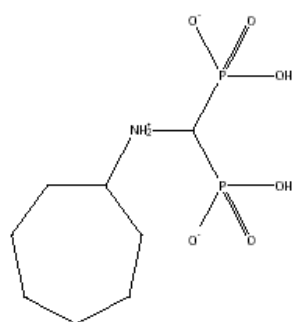
Ref Code



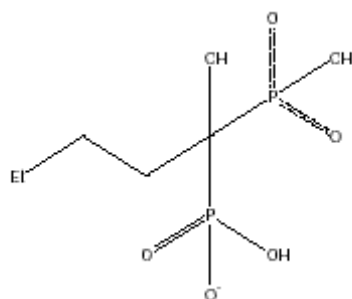
WURPOO [101]

H₂O

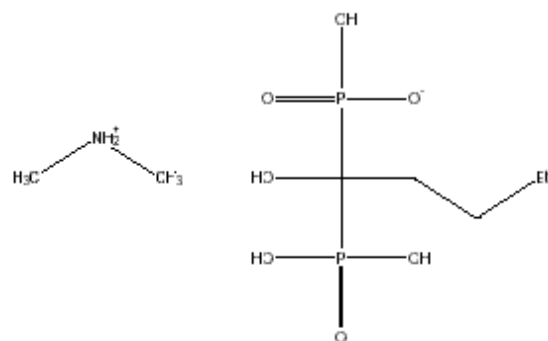
Na⁺



WURXEM [102]



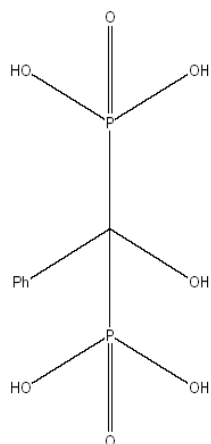
XOBMIK [103]



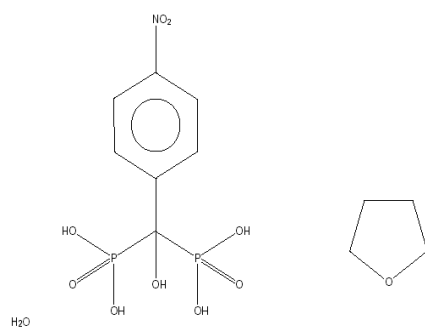
XOBMIK01 [104]

CSD Structure

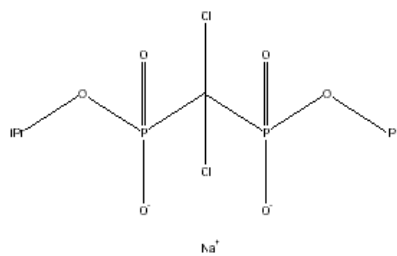
Ref Code



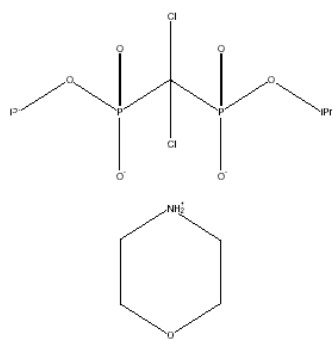
XOSGER [105]



XOSGIV [105]



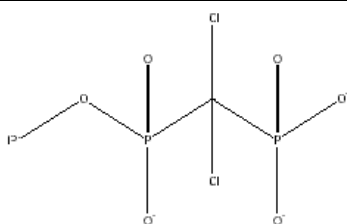
ZARJAD [106]



ZARJEH [106]

CSD Structure

Ref Code



ZARJIL [106]

Na⁺

Table A2: The structures and ref codes of structures obtained from the CSD excluded from the modelling

Structure	Ref Code	Reason for Exclusion
	JOTVIX [80]	Hyperchem[42] has insufficient parameters for bromine

Table A3: Comparison of bond lengths and bond angles obtained using the structures
obtained from simulated annealing

Parameter	Number of protons						Average	Standard deviation
	0	1	2	3	4	5		
<i>Bond lengths/ Å</i>								
P5-C3	1.835	1.836	1.837	1.836	1.837	1.839	1.837	0.001
P5-O	1.554	1.554	1.540	1.518	1.481	1.482	1.521	0.034
P5-OH	n/a	n/a	1.627	1.628	1.628	1.591	1.618	0.018
OH-HO	0.974	0.975	0.974	0.976	0.974	0.979	0.975	0.002
C3-OH	1.436	1.437	1.435	1.436	1.438	1.436	1.436	0.001
C3-C3	1.551	1.551	1.551	1.550	1.550	1.551	1.551	0.000
C3-H	1.093	1.092	1.092	1.092	1.093	1.093	1.092	0.000
C3-NH	1.507	1.508	1.508	1.507	1.508	1.508	1.508	0.001
NH-HN	1.033	1.033	1.033	1.033	1.033	1.033	1.033	0.000
<i>Bond angles/ degrees</i>								
P5-C3-P5	113.9	114.4	114.2	113.6	114.1	115.3	114.3	0.6
O-P5-C3	107.6	107.6	108.5	109.3	110.8	111.7	109.3	1.7
OH-P5-C3	n/a	n/a	104.1	104.6	104.5	105.6	104.7	0.7
O-P5-O	111.1	111.1	111.5	112.7	111.2	n/a	111.5	0.7
O-P5-OH	n/a	n/a	110.0	110.2	112.5	112.6	111.3	1.4
OH-P5-OH	n/a	n/a	n/a	n/a	105.2	108.0	106.6	2.0
HO-OH-P5	n/a	n/a	110.5	107.7	110.3	104.9	108.3	2.6
OH-C3-P5	104.0	104.7	103.9	104.0	105.1	104.3	104.3	0.5
HO-OH-C3	110.0	110.3	109.8	109.9	110.3	110.2	110.1	0.2
C3-C3-P5	112.7	112.3	112.7	113.0	111.9	112.1	112.5	0.4
C3-C3-OH	108.5	107.6	108.6	108.3	108.1	107.8	108.1	0.4
C3-C3-C3	113.6	113.6	113.6	113.8	113.6	113.6	113.6	0.1
H-C3-C3	109.3	109.3	109.3	109.3	109.3	109.3	109.3	0.0
H-C3-H	107.8	107.8	107.8	107.8	107.8	107.9	107.8	0.0
C3-C3-NH	110.5	110.7	110.7	109.9	110.7	110.7	110.5	0.3
H-C3-NH	108.0	108.0	108.0	108.0	108.0	108.0	108.0	0.0
C3-NH-HN	110.0	110.4	110.4	110.4	110.4	110.5	110.4	0.2
HN-NH-HN	108.1	108.5	108.5	108.5	108.5	108.5	108.4	0.2

All values are an average of ten measurements

Section 2: Supplementary figures in the Appendix

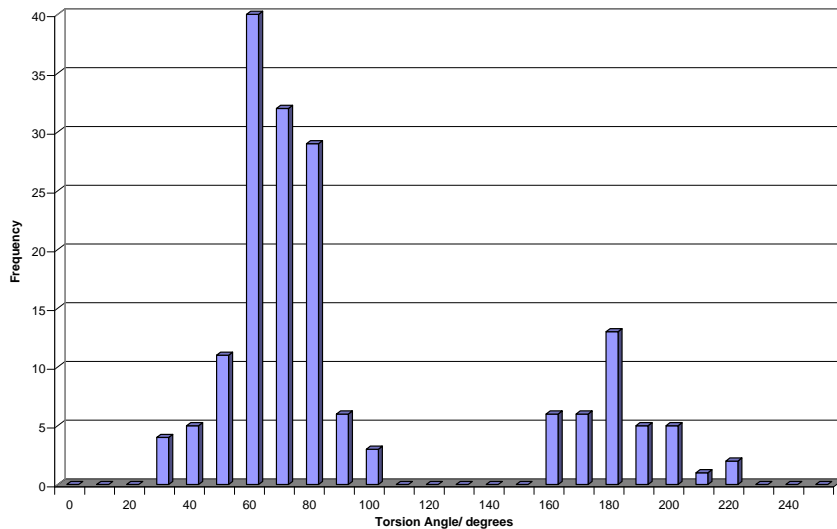


Figure A1: Distribution of torsional angles for the torsion $\bar{\text{O}}\text{-P- C-P}$

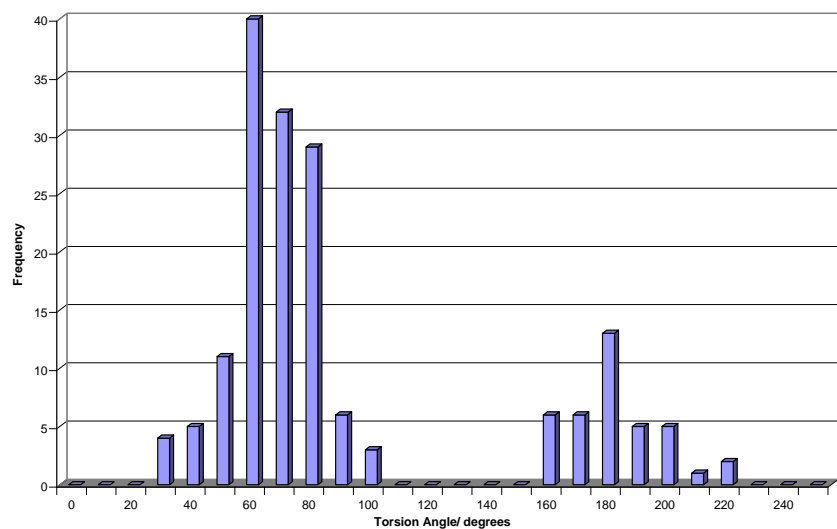


Figure A2: Distribution of torsional angles for the torsion HO-P-C-P

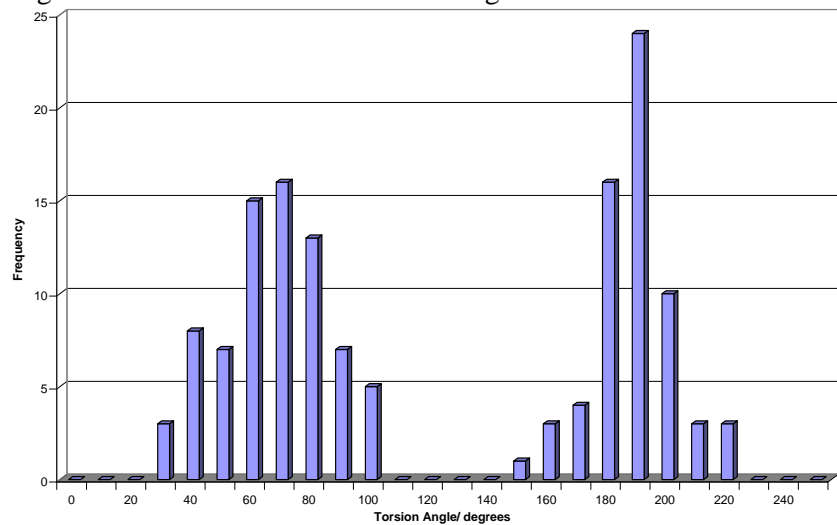


Figure A3: Distribution of torsional angles for the torsion $\bar{\text{O}}\text{-P-C-X}$ (where X is any substituent)

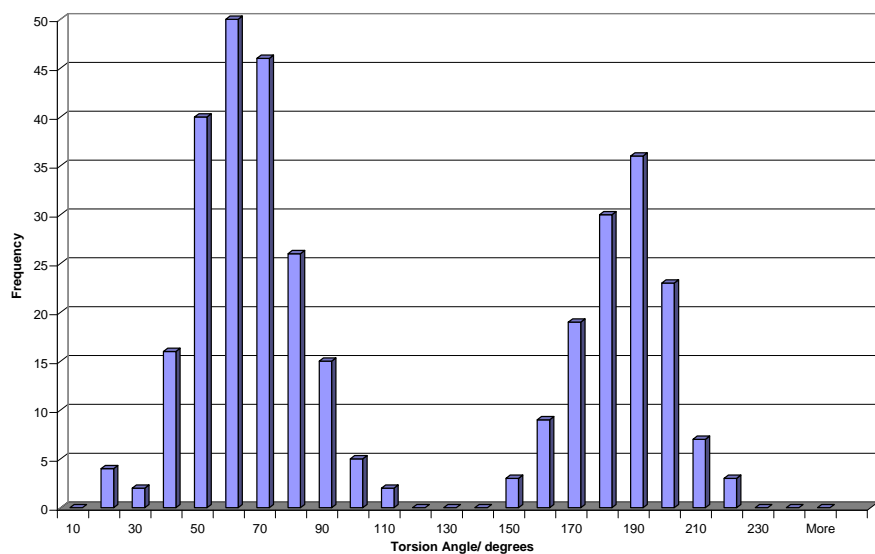


Figure A4: Distribution of torsional angles for the torsion OH-P-C-X (where X is any substituent)

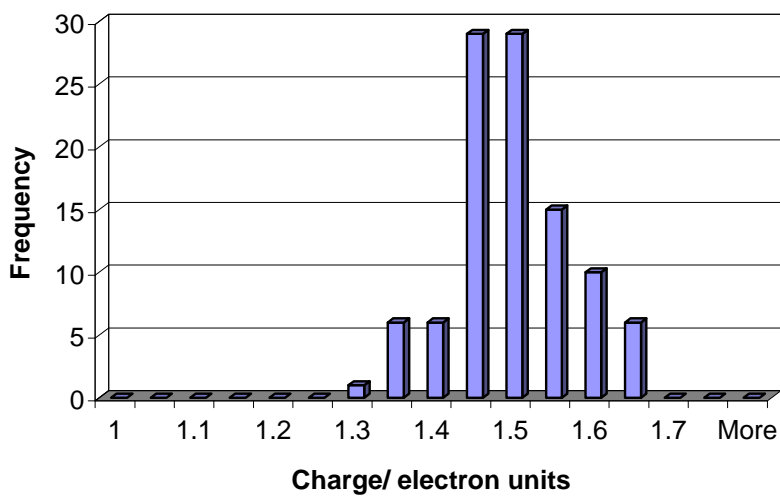


Figure A5: Charge distribution for atom type P5

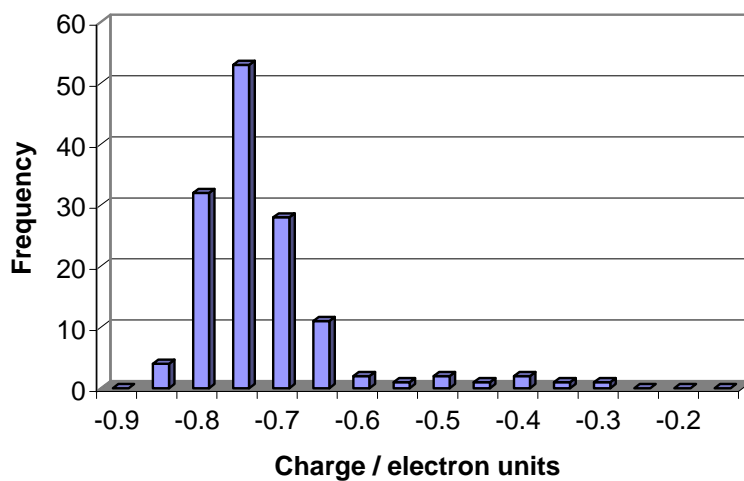


Figure A6: Charge distribution for atom type C3

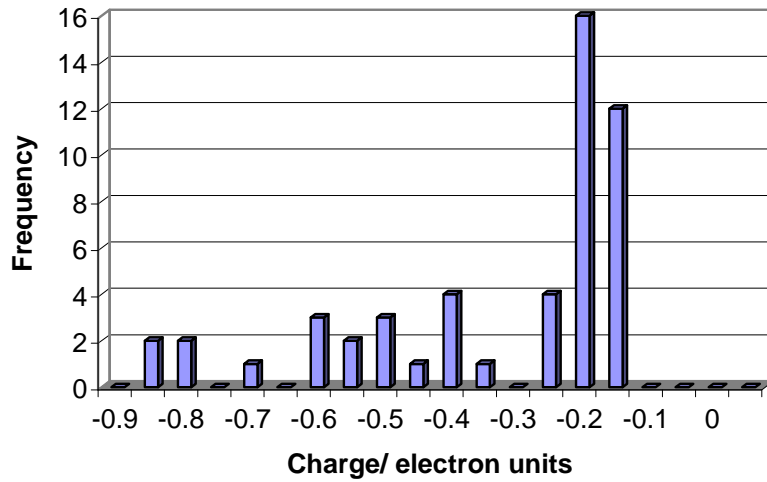


Figure A7: Charge distribution for atom type O

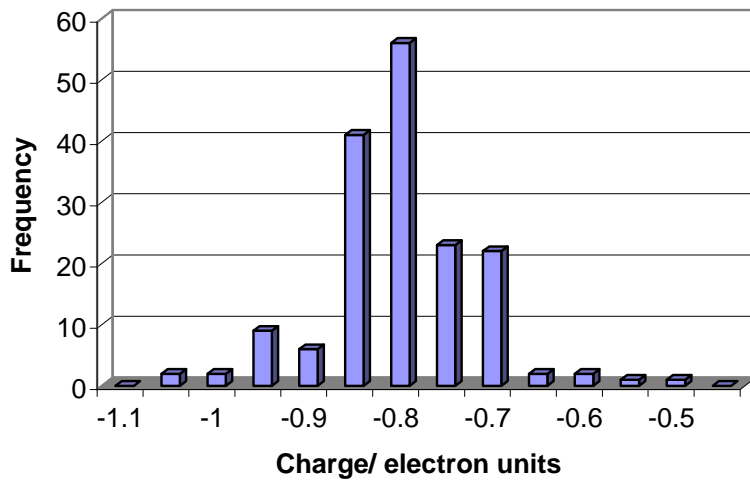


Figure A8: Charge distribution for atom type OH

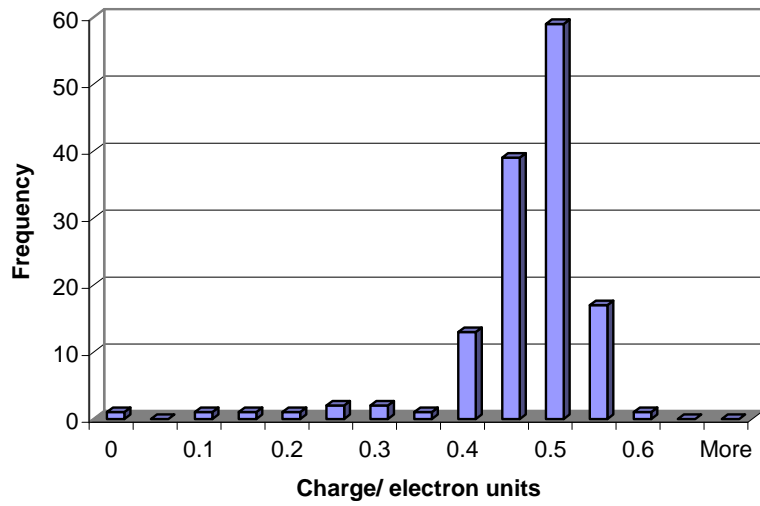


Figure A9: Charge distribution for atom type HO

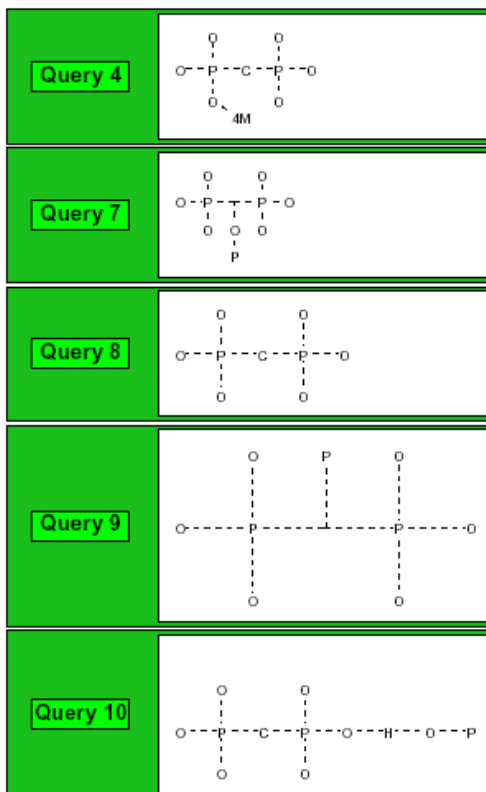
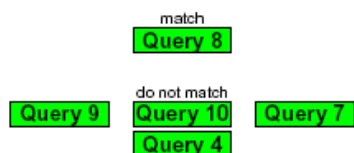
Section 3: Supplementary documents in the Appendix

A1: Search criteria use to obtain the crystallographic data for the bisphosphonates

Search Overview

Search: search28
Date/Time done: Mon Feb 14 14:42:27 2005
Database(s): CSD version 5.26 (November 2004)
Restriction Info: No refoode restrictions applied
Filters: 3D coordinates determined R factor < 0.075
Not disordered No errors
Not polymeric No powder structures
Percentage Completed: 100%
Number of Hits: 64

Summary of queries used. Search found structures that:



A2. An example of an .ent file

HEADER CSD ENTRY AHIJUW

COMPND UNNAMED

AUTHOR GENERATED BY CONQUEST

CRYST1 6.666 6.676 15.571 84.08 82.80 85.78 P-1 2

ATOM	1	N1	UNK	0	1	7.949	1.985	1.638	1.00	0.00
ATOM	2	H1	UNK	0	1	8.400	2.130	2.362	1.00	0.00
ATOM	3	C1	UNK	0	1	8.433	1.596	0.465	1.00	0.00
ATOM	4	H2	UNK	0	1	9.355	1.490	0.266	1.00	0.00
ATOM	5	N2	UNK	0	1	7.429	1.458	-0.374	1.00	0.00
ATOM	6	H3	UNK	0	1	7.478	1.179	-1.183	1.00	0.00
ATOM	7	C2	UNK	0	1	6.260	1.760	0.274	1.00	0.00
ATOM	8	H4	UNK	0	1	5.420	1.745	-0.132	1.00	0.00
ATOM	9	C3	UNK	0	1	6.572	2.078	1.551	1.00	0.00
ATOM	10	C4	UNK	0	1	5.678	2.429	2.693	1.00	0.00
ATOM	11	H5	UNK	0	1	6.176	2.883	3.419	1.00	0.00
ATOM	12	H6	UNK	0	1	5.014	3.036	2.305	1.00	0.00
ATOM	13	C5	UNK	0	1	4.922	1.201	3.287	1.00	0.00
ATOM	14	Na1	UNK	0	1	6.547	2.065	6.798	1.00	0.00
ATOM	15	O1	UNK	0	1	4.200	0.615	2.203	1.00	0.00
ATOM	16	H7	UNK	0	1	3.713	-0.031	2.468	1.00	0.00
ATOM	17	O2	UNK	0	1	7.096	0.782	4.842	1.00	0.00
ATOM	18	O3	UNK	0	1	6.779	-0.724	2.795	1.00	0.00
ATOM	19	O4	UNK	0	1	5.318	-1.011	4.829	1.00	0.00
ATOM	20	H8	UNK	0	1	5.788	-1.697	4.897	1.00	0.00
ATOM	21	O5	UNK	0	1	2.790	2.787	3.796	1.00	0.00
ATOM	22	O6	UNK	0	1	4.425	2.391	5.727	1.00	0.00
ATOM	23	O7	UNK	0	1	2.908	0.545	4.925	1.00	0.00
ATOM	24	H9	UNK	0	1	2.086	0.634	4.895	1.00	0.00
ATOM	25	O8	UNK	0	1	9.059	1.646	7.747	1.00	0.00
ATOM	26	H10	UNK	0	1	9.379	1.947	8.474	1.00	0.00
ATOM	27	H11	UNK	0	1	9.658	1.907	7.216	1.00	0.00
ATOM	28	O9	UNK	0	1	5.776	3.190	8.767	1.00	0.00
ATOM	29	H12	UNK	0	1	5.549	2.626	9.312	1.00	0.00
ATOM	30	H13	UNK	0	1	5.395	3.898	8.964	1.00	0.00

ATOM 31 O10 UNK 0 1 7.618 3.832 5.591 1.00 0.00
ATOM 32 H14 UNK 0 1 8.196 4.213 6.050 1.00 0.00
ATOM 33 H15 UNK 0 1 8.043 3.475 4.949 1.00 0.00
ATOM 34 O11 UNK 0 1 9.308 -1.548 2.285 1.00 0.00
ATOM 35 H16 UNK 0 1 8.514 -1.274 2.353 1.00 0.00
ATOM 36 H17 UNK 0 1 9.338 -2.210 2.794 1.00 0.00
ATOM 37 P1 UNK 0 1 6.162 0.009 3.947 1.00 0.00
ATOM 38 P2 UNK 0 1 3.718 1.828 4.531 1.00 0.00
CONNECT 1 2 3 9
CONNECT 2 1
CONNECT 3 1 4 5
CONNECT 4 3
CONNECT 5 3 6 7
CONNECT 6 5
CONNECT 7 5 8 9
CONNECT 8 7
CONNECT 9 1 7 10
CONNECT 10 9 11 12 13
CONNECT 11 10
CONNECT 12 10
CONNECT 13 10 15 37 38
CONNECT 14 0
CONNECT 15 13 16
CONNECT 16 15
CONNECT 17 37
CONNECT 18 37
CONNECT 19 20 37
CONNECT 20 19
CONNECT 21 38
CONNECT 22 38
CONNECT 23 24 38
CONNECT 24 23
CONNECT 25 26 27
CONNECT 26 25
CONNECT 27 25

CONNECT 28 29 30
CONNECT 29 28
CONNECT 30 28
CONNECT 31 32 33
CONNECT 32 31
CONNECT 33 31
CONNECT 34 35 36
CONNECT 35 34
CONNECT 36 34
CONNECT 37 13 17 18 19
CONNECT 38 13 21 22 23
MASTER 0 0 0 0 0 0 0 0 0 38 0 38 0
END

A3. An example of a .hin file

```
forcefield mm+
sys 0 0 1
view 40 0.18557 55.75 15.75 1 0 0 0 1 0 0 0 1 -5.872 -1.0015 -59.814
seed -1111
mol 1
res 1 UNK 1 - 0
atom 1 N1 N OW - 0 7.949 1.985 1.638 3 2 s 3 s 9 s
atom 2 H1 H HO - 0 8.4 2.13 2.362 1 1 s
atom 3 C1 C B3 - 0 8.433 1.596 0.465 3 1 s 4 s 5 s
atom 4 H2 H H - 0 9.355 1.49 0.266 1 3 s
atom 5 N2 N OW - 0 7.429 1.458 -0.374 3 3 s 6 s 7 s
atom 6 H3 H HO - 0 7.478 1.179 -1.183 1 5 s
atom 7 C2 C B3 - 0 6.26 1.76 0.274 3 5 s 8 s 9 s
atom 8 H4 H H - 0 5.42 1.745 -0.132 1 7 s
atom 9 C3 C B3 - 0 6.572 2.078 1.551 3 1 s 7 s 10 s
atom 10 C4 C C4 - 0 5.678 2.429 2.693 4 9 s 11 s 12 s 13 s
atom 11 H5 H H - 0 6.176 2.883 3.419 1 10 s
atom 12 H6 H H - 0 5.014 3.036 2.305 1 10 s
atom 13 C5 C C4 - 0 4.922 1.201 3.287 4 10 s 14 s 24 s 25 s
atom 14 O1 O O2 - 0 4.2 0.615 2.203 2 13 s 15 s
atom 15 H7 H SI - 0 3.713 -0.031 2.468 1 14 s
atom 16 O2 O ** - 0 7.096 0.782 4.842 1 24 s
atom 17 O3 O ** - 0 6.779 -0.724 2.795 1 24 s
atom 18 O4 O O2 - 0 5.318 -1.011 4.829 2 19 s 24 s
atom 19 H8 H SI - 0 5.788 -1.697 4.897 1 18 s
atom 20 O5 O ** - 0 2.79 2.787 3.796 1 25 s
atom 21 O6 O ** - 0 4.425 2.391 5.727 1 25 s
atom 22 O7 O O2 - 0 2.908 0.545 4.925 2 23 s 25 s
atom 23 H9 H SI - 0 2.086 0.634 4.895 1 22 s
atom 24 P1 P CP - 0 6.162 0.009 3.947 4 13 s 16 s 17 s 18 s
atom 25 P2 P CP - 0 3.718 1.828 4.531 4 13 s 20 s 21 s 22 s
endres 1
endmol 1
mol 2
```

atom 1 NA1 Na ** - 0 6.547 2.065 6.798 0

endmol 2

mol 3

atom 1 O8 O O2 - 0 9.059 1.646 7.747 2 2 s 3 s

atom 2 H10 H SI - 0 9.379 1.947 8.474 1 1 s

atom 3 H11 H SI - 0 9.658 1.907 7.216 1 1 s

endmol 3

mol 4

atom 1 O9 O O2 - 0 5.776 3.19 8.767 2 2 s 3 s

atom 2 H12 H SI - 0 5.549 2.626 9.312 1 1 s

atom 3 H13 H SI - 0 5.395 3.898 8.964 1 1 s

endmol 4

mol 5

atom 1 O10 O O2 - 0 7.618 3.832 5.591 2 2 s 3 s

atom 2 H14 H SI - 0 8.196 4.213 6.05 1 1 s

atom 3 H15 H SI - 0 8.043 3.475 4.949 1 1 s

endmol 5

mol 6

atom 1 O11 O O2 - 0 9.308 -1.548 2.285 2 2 s 3 s

atom 2 H16 H SI - 0 8.514 -1.274 2.353 1 1 s

atom 3 H17 H SI - 0 9.338 -2.21 2.794 1 1 s

endmol 6

A4: An example of an entry in a logfile

HyperChem log start -- Wed Dec 27 13:44:56 2006.

Geometry optimization, MolecularMechanics, molecule = C:\Documents and Settings\Di\My Documents\simplebps\3OH\BEKBOJ_x1.hin.

mmplus

PolakRibiere optimizer

Invalid atom type for atom 4.

Invalid atom type for atom 18.

Invalid atom type for atom 19.

Unknown torsion constant for

atom(1 2 3 5)

type(**-C4-CP-**).

Unknown torsion constant for

atom(1 2 3 5)

type(**-**-**-**).

Default parameters being used for torsions...

Using default torsion constants

V1 = 0.000000

V2 = 0.000000

A5: An example of the optimisation macro used to perform the minimisation

Control-R	Compute.Results
Channel	<pre>=OpenFile() =IF(ISERROR(Channel)) = RETURN() =END.IF() =EXECUTE(Channel,"[query-response-has-tag(no)]") =EXECUTE(Channel,"[file-format(hin)]") =WHILE(NOT(ISBLANK(SELECTION())))</pre>
Command	<pre>=EXECUTE(Channel,"[open-file(E:\HEDP_dynamics\"&SELECTION()&".hin)]") =EXECUTE(Channel,"[optim-algorithm steepestdescents]") =EXECUTE(Channel,"[optim-max-cycles=1000]") =EXECUTE(Channel,"[do-optimization]") =EXECUTE(Channel,"[optim-algorithm polakribiere]") =EXECUTE(Channel,"[optim-max-cycles=1000]") =EXECUTE(Channel,"[do-optimization]") =SELECT("r[1]c") =EXECUTE(Channel,"[write-file(E:\HEDP_dynamics\"&SELECTION()&".hin)]") =SELECT("r[1]c") =NEXT() =TERMINATE(Channel) =RETURN()</pre>
NewChan	<pre>OpenFile =INITIATE("HyperChem", "System") =IF(ISERROR(NewChan))</pre>
	<pre>= IF(ISERROR(EXEC("d:\Program Files\Hypercube\HyperChem5\PROGRAM\chem.exe",1))) = RETURN(NewChan) = END.IF() = RETURN(INITIATE("HyperChem", "System")) =END.IF() =RETURN(NewChan)</pre>

A6: An example of the statistics macro used to collect the statistics data

Control-R	Compute.Results
Channel	<pre>=OpenFile() =IF(ISERROR(Channel)) = RETURN() =END.IF()</pre>

	<pre> =EXECUTE(Channel,"[query-response-has-tag(no)]") =EXECUTE(Channel,"[file-format(hin)]") =WHILE(NOT(ISBLANK(SELECTION())))</pre>
Command	<pre> =EXECUTE(Channel,"[open-file(C:\Hyper7\Data\simplebps\noOH\"&SELECTION()&".hin)]") =EXECUTE(Channel,"[select-atom 1,1]") =EXECUTE(Channel,"[select-atom 2,1]") =FORMULA.ARRAY(REQUEST(Channel,"selection-value"),"r[1]c") =EXECUTE(Channel,"[select-none]") =SELECT("r[1]c") =EXECUTE(Channel,"[select-atom 1,1]") =EXECUTE(Channel,"[select-atom 2,1]")</pre>
	<pre> =EXECUTE(Channel,"[select-atom 3,1]") =FORMULA.ARRAY(REQUEST(Channel,"selection-value"),"r[1]c") =EXECUTE(Channel,"[select-none]") =SELECT("r[1]c") =EXECUTE(Channel,"[select-atom 1,1]") =EXECUTE(Channel,"[select-atom 2,1]") =EXECUTE(Channel,"[select-atom 3,1]") =EXECUTE(Channel,"[select-atom 11,1]") =FORMULA.ARRAY(REQUEST(Channel,"selection-value"),"r[1]c") =EXECUTE(Channel,"[select-none]") =SELECT("r[1]c") =EXECUTE(Channel,"[select-atom 4,1]") =TERMINATE(Channel) =RETURN()</pre>
NewChan	<p>OpenFile</p> <pre> =INITIATE("HyperChem","System") =IF(ISERROR(NewChan) = IF(ISERROR(EXEC("d:\Program Files\Hypercube\HyperChem5\PROGRAM\chem.exe",1))) = RETURN(NewChan) = END.IF() = RETURN(INITIATE("HyperChem","System")) =END.IF() =RETURN(NewChan)</pre>

Chapter 7: References

- (1) www.medicinenet.com. Accessed 22 January 2005
- (2) van Poznak, C.H. *Canc. Cont.* **2002**, *19*, 480.
- (3) Fleish, H. *Breast Canc. Res.* **2002**, *4*, 30.
- (4) Serafini, A.N. *J. Nucl. Med.* **2001**, *42*, 895.
- (5) Hoskin, P.J. *Clin. Onocol.* **2004**, *16*, 112.
- (6) Fernandez, D.; Wenck, M.A.; Craig, S.P.; Delfino, J.M. *Bioinorg. Med. Chem. Lett.* **2004**, *14*, 4501.
- (7) Heymann, D.; Ory, B.; Gouin, F. Green, J.R.; Redini F. *Trends Mol. Med.* **2004**, *10*, 337.
- (8) Kotsikorou, E.; Oldfield, E. *J. Med.Chem.* **2003**, *46*, 2932.
- (9) Zeevaart, J.R.; Jarvis, N.V.; Louw, W.K.A.; Jackson, G.E.; Cukrowski, I.; Mouton, C.J. *J. Inorg. Biochem.* **1999**, *73*, 265.
- (10) Zeevaart, J.R.; Jarvis, N.V.; Louw, W.K.A.; Jackson, G.E. *J. Inorg. Biochem.* **2001**, *83*, 57.
- (11) Neves, M.; Gano, L.; Pereira, N.; Costa, M.C.; Chandia, M.; Rosado, M.; Fausto R. *Nuc. Med. Bio.* **2002**, *29*, 329.
- (12) Lin, J.H. *Bone* **1996**, *18*, 75.
- (13) van der Plutjm, G.; Vloedgraven, H.; van der Beek, E. *J. Clin. Invest.* **1996**, *98*, 698.
- (14) Jagdev, S.P.; Coleman, R.E.; Shipman, C.M. *Brit. J. Canc.* **2001**, *84*, 1126.
- (15) Neves, M.; Gano, L.; Pereira, N.; Costa, M. C.; Costa, M. R.; Chandia, M.; Rosado, M.; Fausto, R. *Nucl. Med. Biol.* **2002**, *29*, 329.
- (16) Barnett, B. L.; Strickland, L. C. *Acta Cryst. Sec. B* **1979**, *35*, 1212.
- (17) Fleischer, H. *Endocrine Rev.* **1998**, *80*.
- (18) van Beek, E.; Pieterman, E.; Cohen, L.; Lowik, C.; Papapoulos, S. *Biochem. Biophys. Res. Commun.* **1999**, *255*, 491.
- (19) Cromartie, T. H.; Fisher, K. J.; Grossman, J. N. *Pest. Biochem. Physiol.* **1999**, *63*, 114.
- (20) Oberhauser, V.; Gaudin, J.; Fonne-Pfister, R.; Schar, H. P. *Pest. Biochem. Physiol.* **1998**, *60*, 111.
- (21) Martin, M. B.; Arnold, W.; Heath, H. T.; Urbina, J. A.; Oldfield, E. *Biochem. Biophys. Res. Comm.*, **1999**, *263*, 754.
- (22) Moreno, B.; Bailey, B. N.; Luo, S.; Martin, M.; Kuhlenschmidt, M.; Moreno, S. N. J.; Docampo, R.; Oldfield, E. *Biochem. Biophys. Res. Comm.*, **2001**, *284*, 632.
- (23) Moreno, B.; Urbina, J. A.; Oldfield, E.; Bailey, B. N.; Rodrigues, C. O.; Docampo, R. *J. Biol. Chem.* **2000**, *275*, 28356.

- (24) Rodrigues, C. O.; Scott, D. A.; Bailey, B. N.; de Sousa, W.; Benchimol, M.; Moreno, B.; Urbina, J. A.; Oldfield, E.; Moreno, S. N. *J. Biochem. J.* **2000**, *349*, 737.
- (25) Urbina, J. A.; Moreno, B.; Vierkotter, S.; Oldfield, E.; Payares, G.; Sanoja, C.; Bailey, B. N.; Yan, W.; Scott, W.; Moreno, S.; Docampo, R. *J. Biol. Chem.* **1999**, *274*, 33609.
- (26) Gordon-Weeks, R.; Parmar, S.; Davies, T. G.; Leigh, R. A. *Biochem. J.* **1999**, *337*, 373.
- (27) Szabo, C. M.; Oldfield, E. *Biochem. Biophys. Res. Commun.* **2001**, *287*, 468.
- (28) Rappe, A. L.; Colwell, K. S.; Casewit, C. J. *Inorg. Chem.* **1993**, *32*, 3438.
- (29) Ullman, B.; Carter, D. *Int. J. Parasitol.* **1997**, *27*, 203.
- (30) Wang, C. C. *Parasitology* **1997**, *114*.
- (31) Fernandez, D.; Wenck, M. A.; Craig, S. P.; Delfino, J. M. *Bioinorg. Med. Chem. Lett.* **2004**, *14*, 4501.
- (32) Levine I. N. *Quantum Chemistry*; 4 ed.; Prentice-Hall, Inc: New Jersey, 1991.
- (33) Leach A.R. *Molecular Modelling- Principles and Applications*; 2 ed.; Pearson Education Ltd.: Edinburgh, 2001.
- (34) Atkins P.W. *Molecular Quantum Mechanics*; 2 ed.; Oxford University Press: Great Britain, 1988.
- (35) Hall G.G. *Proceedings of the Royal Society (London)* **1951**, 541.
- (36) Roothaan C.C.J. *Rev. Mod. Phys.* **1951**, *23*, 69.
- (37) Weiner S.J.; Kollman P.A.; Nguyen D.T.; Case D.A. *J. Comput. Chem.* **1986**, *7*, 230.
- (38) Cornell W.D.; Cieplak P.; Bayly C.I.; Gould I.R.; Merz Jr K.M.; Ferguson D.M.; Spellmeyer D.C.; Fox T.; Caldwell J.W.; Kollman P.A. *J. Amer. Chem. Soc.* **1995**, *117*, 5179.
- (39) Wang J.; Cieplak P.; Kollman P.A. *J. Comput. Chem.* **2000**, *21*, 1049.
- (40) Weiner S.J.; Kollman P.A.; Case D.A.; Singh U.C.; Ghio C.; Alagona G.; Profeta Jr S.; Weiner P. *J. Amer. Chem. Soc.* **1984**, *106*, 765.
- (41) Allinger N.L. *J. Amer. Chem. Soc.* **1977**, *99*, 8127.
- (42) Hypercube Inc: Gainesville, Florida, 2002.
- (43) Lii J.-H.; Allinger N.L. *J. Comput. Chem.* **1991**, *21*, 186.
- (44) Brooks B.R.; Bruccoleri R.E.; Olafson B.D.; States D.J.; Swaminathan S.; Karplus M. *J. Comput. Chem.* **1983**, *4*, 187.
- (45) Jorgensen W.L.; Tirado-Rives J. *J. Amer. Chem. Soc.* **1988**, *110*, 1657.
- (46) Pranata J.; Wierschke S.G.; Jorgensen W.L. *J. Amer. Chem. Soc.* **1991**, *113*, 2810.
- (47) Wang J.; Wolf R.M.; Caldwell J.W.; Kollman P.A.; Case D.A. *J. Comput. Chem.* **2004**, *25*, 1157.
- (48) Wang J.; Kollman P.A. *J. Comput. Chem.* **2001**, *22*, 1219.

- (49) Allen F.H. *Acta Cryst. Sect. B* **2002**, 58, 380.
- (50) Stewart J.J.P. *J. Comput. Chem.* **1989**, 10, 209.
- (51) Allinger N.L. *J. Comput. Chem.* **1996**, 17, 642.
- (52) Marques H.M.; Brown K.L. *Coord. Chem. Rev.* **1999**, 127, 190-12.
- (53) Kay M.I.; Young R.A.; Posner A.S. *Nature* **1964**, 204, 1050.
- (54) Fluck, E. *J. Res. Natl. Inst. Stand. Technol.* **1996**, 101, 217.
- (55) Sheldrick, G. M.; University of Gottingen, Germany.: 1997.
- (56) Farrugia, L. J. *J. Appl. Crystallogr.* **1999**, 32, 837.
- (57) Bruno, I. J.; Cole, J. C.; Edgington, P. R.; Kessler, M. K.; Macrae, C. F.; McCabe, P.; Pearson, J. *Acta Crystallogr. Sec. B* **2002**, 58, 389.
- (58) Martell A.E.; Smith R.M. *Critical Stability Constants*; Plenum: New York, 1982.
- (59) Turhanen P.A.; Ahlgren M.J.; Jarvinen T.; Vepsalainen J.J. *Phosphorus, Sulfur, Silicon, Relat. Elem.* **2001**, 170, 115.
- (60) Vepsalainen J.J.; Nupponen H.; Pohjala E.; Ahlgren M.J.; Vainiotalo P.J. *J. Chem. Soc. Perkin Trans.* **1992**, 2, 835.
- (61) Bailly T.; Burgada R.; Prange T.; Lecouvey M. *Tetrahedron Lett.* **2003**, 44, 189.
- (62) Benech J.M.; Coindet-Benramdane M.; Leroux Y.Z. *Kristallogr.-New Cryst. Struct.* **1997**, 212, 499.
- (63) Kontturi M.; Vuokila-Laines E.; Peranierni S.; Pakkanen T.T.; Vepsalainen J.J.; Ahlgren M.J. *J. Chem. Soc. Dalton Trans.* **2002**, 1969.
- (64) Vepsalainen J.J.; Kivikoski J.; Ahlgren M.J.; Nupponen H.; Pohjala E. *Tetrahed.* **1995**, 51, 6805.
- (65) Gossman, W. L.; Wilson, S. R.; Oldfield, E. *Acta Crystallogr. Sec. C* **2002**, 58, m599.
- (66) Saunders, J. M.; Gomez, A. O.; Mao, J.; Meints, G. A.; van Brussel, E. M.; Burzynska, A.; Kafarski, P.; Gonzalez-Pacanoska, D.; Oldfield, E. *J. Med. Chem.* **2003**, 46, 5171.
- (67) Uchtman, V. A. *J. Phys. Chem.* **1972**, 76, 1304.
- (68) Kontturi, M.; Vuokila-Laines, E.; Peranierni, S.; Pakkanen, T. T.; Vepsalainen, J. J.; Ahlgren, M. *J. Chem. Soc. Dalton Trans.* **2002**, 1969.
- (69) Nardelli, M.; Pelizzi, G.; Staibano, G.; Zucchi, E. *Inorg. Chim. Acta* **1983**, 80, 259.
- (70) Hmimid, N.; Besse, J. P.; Chevalier, R. *Mater. Chem. Phys.* **1985**, 12, 491.
- (71) Vega, D.; Fernandez, D.; Ellena, J. A. *Acta Crystallogr. Sec. C* **2002**, 58, m77.
- (72) Fernandez, D.; Vega, D.; Ellena, J. A. *Acta Crystallogr. Sec. C* **2003**, 59, o289.
- (73) Uchtman, V. A.; Gloss, R. A. *J. Phys. Chem.* **1972**, 76, 1298.
- (74) Silvestre, J. P.; Dao, N. Q.; Salvini, P. *Phosphorus, Sulfur, Silicon, Relat. Elem.* **2002**, 177, 771.

- (75) Hmimid, N.; Besse, J. P.; Chevalier, R. *Acta Crystallogr. Sec. C* **1987**, *43*, 782.
- (76) Shkol'nikova, L. M.; Shcherbakov, B. K.; Dyatlova, N. M.; Medved, T. Y.; Kabachnik, M. I. *Izv. Akad. Nauk SSSR, Ser. Khim.* **1987**, 1511.
- (77) Ohanessian, J.; Avenal, D.; El Manouni, D.; Benramdane, M. *Phosphorus, Sulfur, Silicon, Relat. Elem.* **1997**, *129*, 99.
- (78) Sergienko, V. S.; Aleksandrov, G. G.; Afonin, E. G. *Koord. Khim. (Russ.)(Coord. Chem.)* **1999**, *25*, 323.
- (79) Turhanen, P. A.; Ahlgren, M. J.; Jarvinen, T.; Vepsalainen, J. J. *Phosphorus, Sulfur, Silicon, Relat. Elem.* **2001**, *170*, 115.
- (80) Vepsalainen, J. J.; Nupponen, H.; Pohjala, E.; Ahlgren, M. J.; Vainiotalo, P. *J. Chem. Soc. Perkin Trans. 2* **1992**, 835.
- (81) Wu, Z.; Liu, Z.; Tian, P.; Xu, L.; He, Y.; Sang, S.; Yang, Y.; Liu, X.; Liu, X.; Bao, X. *Acta Crystallogr. Sec. E* **2003**, *59*, m521.
- (82) Shkol'nikova, L. M.; Masyuk, A. A.; Polyanchuk, G. V.; Krinitskaya, L. V.; Afonin, E. G.; Pechurova, N. I.; Dyatlova, N. M. *Koord. Khim. (Russ.)(Coord. Chem.)* **1989**, *15*, 486.
- (83) Shkol'nikova, L. M.; Afonin, E. G.; Kalugina, E. V.; Sotman, S. S. *Kristallografiya (Russ.)(Crystallogr. Rep.)* **1991**, *36*, 77.
- (84) Leroux, Y.; El Manouni, D.; Safsaf, A.; Neuman, A.; Gillier, H. *Phosphorus, Sulfur, Silicon, Relat. Elem.* **1991**, *63*, 181.
- (85) Olive, G.; Ellis, D. D.; Siri, D.; Le Moigne, F.; Lutz, M.; Spek, A. L.; Tordo, P.; Reboul, J. P. *Acta Crystallogr. Sec. C* **2000**, *56*, 720.
- (86) De La Matter, D.; McCullough, J. J.; Calvo, C. *J. Phys. Chem.* **1973**, *77*, 1146.
- (87) Peterson, S. W.; Gebert, E.; Reis, A. H.; Druyan, M. E.; Mason, G. W.; Pepperd, D. F. *J. Phys. Chem.* **1977**, *81*, 466.
- (88) Barbey, C.; Lecouvey, M. Z. *Kristallogr.- New Cryst. Struct.* **2002**, *217*, 137.
- (89) Martin, M. B.; Sanders, J. M.; Kendrick, H.; de Luca-Fradley, K.; Lewis, J. C.; Grimley, J. S.; van Brussel, E. M.; Olsen, J. R.; Meints, G. A.; Burzynska, A.; Kafarski, P.; Croft, S. L.; Oldfield, E. *J. Med. Chem.* **2002**, *45*, 2904.
- (90) Szabo, C. M.; Martin, M. B.; Oldfield, E. *J. Med. Chem.* **2002**, *45*, 2894.
- (91) Bailly, T.; Burgada, R.; Prange, T.; Lecouvey, M. *Tetrahedron Lett.* **2003**, *44*, 189.
- (92) Sergienko, V. S.; Aleksandrov, G. G.; Afonin, E. G. *Kristallografiya (Russ.)(Crystallogr. Rep.)* **1997**, *42*, 1049.
- (93) Benech, J. M.; Coindet-Benramdane, M.; Leroux, Y. Z. *Kristallogr.- New Cryst. Struct.* **1997**, *212*, 499.

- (94) Matczak-Jon, E.; Sawka-Dobrowolska, W.; Kafarski, P.; Videnova-Adrabinska, V. *New J. Chem. (Nouv. J. Chim.)* **2001**, 25, 1447.
- (95) Aleksandrov, G. G.; Sergienko, V. S.; Afonin, E. G. *Kristallografiya (Russ.)(Crystallogr. Rep.)* **1997**, 42, 438.
- (96) Charpin, P.; Lance, M.; Nierlich, M.; Vigner, D.; Lee, M. R.; Silvestre, J. P.; Dao, N. Q. *Acta Crystallogr. Sec. C* **1988**, 44, 990.
- (97) Silvestre, J. P.; Bkouche-Waksman, I.; Heger, G.; Dao, N. Q. *New J. Chem. (Nouv. J. Chim.)* **1990**, 14, 29.
- (98) Shkol'nikova, L. M.; Masyuk, A. A.; Afonin, E. G.; Dyatlova, N. M. *Koord. Khim. (Russ.)(Coord. Chem.)* **1989**, 15, 747.
- (99) Shkol'nikova, L. M.; Sotman, S. S.; Afonin, E. G. *Kristallografiya (Russ.)(Crystallogr. Rep.)* **1990**, 35, 1442.
- (100) Coiro, V. M.; Lamba, D. *Acta Crystallogr. Sec. C* **1989**, 45, 446.
- (101) Gossman, W. L.; Wilson, D. L.; Oldfield, E. *Acta Crystallogr. Sec. C* **2003**, 59, m33.
- (102) van Brussel, E. M.; Gossman, W. L.; Wilson, S. R.; Oldfield, E. *Acta Crystallogr. Sec. C* **2003**, 59, o93.
- (103) Neuman, A.; Coindet-Benramdane, M.; Gillier, H.; Leroux, Y.; El Manouni, D.; Prange, T. Z. *Kristallogr.- New Cryst. Struct.* **2002**, 217, 154.
- (104) Navaza, A.; Chevrier, G.; Kiat, J. M.; Barbey, C. *J. Solid State Chem.* **2002**, 167, 441.
- (105) Lecouvey, M.; Barbey, C.; Navaza, A.; Neuman, A.; Prange, T. *Acta Crystallogr. Sec. C* **2002**, 58, o521.
- (106) Vepsalainen, J. J.; Kivikoski, J.; Ahlgren, M. J.; Nupponen, H. E.; Pohjala, E. K. *Tetrahed.* **1995**, 51, 6805.

